Master's thesis

NTNU
Norwegian University of Science and Technology
Faculty of Natural Sciences
Department of Materials Science and Engineering

Aurora Cathrin Pedersen

Freeze-drying of NMC cathodes for Li-ion batteries

Master's thesis in Chemical Engineering and Biotechnology
Supervisor: Ann Mari Svensson
Co-supervisor: Magnus Rotan and Fride Vullum-Bruer
January 2023

NTNU
Norwegian University of
Science and Technology

Aurora Cathrin Pedersen

Freeze-drying of NMC cathodes for Li-ion batteries

Master's thesis in Chemical Engineering and Biotechnology
Supervisor: Ann Mari Svensson
Co-supervisor: Magnus Rotan and Fride Vullum-Bruer
January 2023

Norwegian University of Science and Technology
Faculty of Natural Sciences
Department of Materials Science and Engineering

NTNU
Norwegian University of
Science and Technology

Preface

This master thesis was produced as part of the course "TMT4900 - Materials Chemistry and Energy Technology, Master's Thesis" at NTNU Trondheim. The project evaluates freeze-drying as a possible drying method for cathodes used in lithium-ion batteries.

The materials used were provided by the Department of Material Science and Engineering at NTNU Trondheim and SINTEF Energy Research. The experiments were conducted at the Department of Material Science and Engineering and the Department of Energy and Process Engineering at NTNU Trondheim.

I would like to express gratitude to my supervisor, Ann Mari Svensson, who was always readily available with valuable guidance and helpful input. I would also like to thank my co-supervisors Magnus Rotan, for training in the manufacturing of the electrodes in addition to always being available for counsel, and Fride Vullum-Bruer, for guidance and valuable discussion. Additionally, thanks to Philipp Schweigart for guidance in electrolyte preparation and SINTEF ...s Per-Erik Vellum who created the cross-sections of cathodes using a PFIB, and his guidance in SEM imaging. Further, I would also like to thank Pei Na Kui for her help in everything related to HMS and the use of the glove box.

A special thanks to family and friends who has supported and motivated me through the years. Know that while Trondheim might be rainy, you have always brought sunshine.

Trondheim, 23rd January 2023

Aurora Pedersen

Abstract

In this thesis, freeze-drying was evaluated as a possible drying method for NMC_{622} cathodes. Cathodes produced by freeze-drying and vacuum-drying were characterized using different methods, and the results were compared. Galvanostatic cycling with potential limits gave varying results for the freeze-dried electrodes. It displayed a lower average capacity compared to the vacuum-dried used as reference, but an efficiency that was comparable to the reference and lower irreversible losses at 6.28-9.04 % compared to the reference of 7.24-9.08 % depending on the C-rate. The freeze-dried electrodes had a considerable higher uncertainty, due to the variation in performance by the parallels, than the vacuum-dried electrodes, deviating on average 28.24 mAh g^{-1}compared to 4.42 mAh $g^{-1}$the reference electrode at 1C.

Symmetrical cells using the NMC cathodes as both working- and counter-electrode, and an inert electrolyte at two different concentrations were used in electrochemical impedance measurements. The electrolytes consisted of 0.01M and 0.005M TBATFSI in 1:1 wt% EC:DMC. The results from the measurements were fitted to a Randles circuit to determine the resistance in the electrodes. Only the values from the 0.005M electrolyte were usable, and it was determined that the tortuosity of the freeze-dried electrode was much higher than the reference electrode.

The reduced performance of the freeze-dried electrodes was attributed to be due to residue solvent in the electrode and insufficient conductivity throughout the electrode due to the binder not being completely coated in the conductive material. The latter claim was supported by SEM imaging showing the bare binder on the electrode surface. Except for the lack of binder coated in conducting material, no other major difference could be observed on the surface or cross-section of the electrodes with SEM imaging. The FTIR spectrum displayed an occurrence around 1670 cm^{-1} in the freeze-dried sample which could not be observed in the reference. This peak occurs at a wavelength where a double binding between carbon and oxygen gives a signal. This indicates traces of solvent left in the material as the solvent is the only component evaluated where this bond occurs, supporting the claim that residue solvent was present in the electrodes.

Sammendrag

I denne masteroppgaven ble frysetørking evaluert som en potensiell tørkemetode i produksjon av NMC_{622} katoder. Det ble produsert testkatoder via frysetørking og referanseelektroder via vakuum-ovn tørking. Katodene ble deretter karakterisert med forskjellige metoder, før resultatene ble sammenlignet. Galvanostatisk sykling med potensialgrenser ga varierende resultater for de frysetørkede elektrodene. De hadde en lavere gjennomsnittlig kapasitet enn de vakuum-tørkede referanseelektrodene, men utfordret på effektivitet og irreversible kapasitetstap med et gjennomsnittlig tap på 6.28-9.04 % per syklus mot of 7.24-9.08 % per syklus for referanseelektrodene avhengig av C-raten. De frysetørkede elektrodene hadde større usikkerhet grunnet store variasjoner i prestasjonene mellom parallellene, enn de vakuum-tøkede elektrodene med et gjennomsnittlig standardavvik på 28.24 mAh g^{-1}per syklus mot 4.42 mAh g^{-1}per syklus for referanseelektrodene.

Symmetriske celler med NMC-elektroder som både arbeids- og mot-elektroder og en inert elektrolytt ved to forskjellige konsentrasjoner, ble benyttet i elektrokjemisk impedans-målinger. Elektrolyttene besto av 0.01M og 0.005M TBATFSI i 1:1 vt% EC:DMC. Resultatene fra målingene ble tilpasset en Randles krest for å bestemme resistansen i electrodene. Kun verdiene fra 0.005M electrolytten var brukbare, og det ble bestemt at tortuositeten i de frysetørkede elektrodene var mye høyere enn turtousiteten i referanse elektrodene.

Den reduserte prestasjonen av de frysetørkede elektrodene ble tilskrevet å være grunnet ufullstendig tørking av elektrodene og utilstrekkelig konduktivitet gjennom elektroden da bindemiddlet ikke var fullstendig dekket av det ledende materialet. Sistnevnte ble observert i SEM-bilder da udekket bindemiddel kunne observeres på elektrodeoverflaten til den frysetørkede elektroden. Utenom dette var det ingen annen signifikant forskjell observert på verken overflate eller kryssseksjon mellom de to elektrodene via SEM. En blanding av bindemiddlet og løsemiddlet brukt i elekktrodene, ble påført på alimiumsfolie, tørket i frysetørker og vakuum-ovn, så karaterisert i FTIR. Spektrumet av den frysetørkede blanding ga et signal rundt 1670 $cm-1$ som ikke ble observert blandingen tøket i vakuum-ovn. Dette signalet inntreffer på en bølgelengde hvor en dobbelbinding mellom karbon og oksygen oppstår. Dette indikerer spor av rester av løsemiddelet i materialet da løsemiddelet er den eneste komponenten tilstede hvor denne bindingen finnes.

Contents

List of Tables

List of Figures

1 Introduction

1.1 Background and motivation

As the demand and supply for electricity-driven technology are increasing, so does the demand for efficient energy storage[1]. The fastest-growing sector of developing energy storage is the transport sector where the EU expects the annual production of lithium-ion batteries (LIB) for electric vehicles (EV) to reach 550 GWh by 2030[2]. The EU's climate goal is to reduce greenhouse gas (GHG) emissions by 55 % by 2030 compared to 1990 and be carbon neutral by 2050[3]. As of 2022, transport accounts for approximately 25% of GHG emissions. To reach the goal, a reduction of 90 % is needed by 2050. The development of new energy storage technology is essential[2]. The EV technology has come very far, and in 2021, 64.5 % of all new cars sold were electric[4]

One major drawback of lithium-ion batteries is the cost, 51 % comes from the price of materials, and 24 % of the cost comes from manufacturing, much of this from energy use[5]. The cost of energy is increasing all over the world which impacts the manufacturing cost of battery packs.[6]. To reduce the cost of production, a reduction of energy consumption is necessary. The energy consumption in manufacturing the electrodes in batteries for electric vehicles is very high compared to the other steps.[7] It is estimated that ca. 38-48% of the energy used in producing a battery pack for electric vehicles goes to coating, drying the electrodes, recovering the solvent, and operating the dry room. These steps constitute more than 23 % of the total cost of the battery pack, where ca. 15 % of this is from the coating and drying. This is due to the difficulty of removing the solvent from the porous structure in electrodes, the toxic nature of some solvents requiring strict procedures and regulations, and the electrodes' sensitivity to moisture.[7;8;9] N-methyl-2-pyrrolidine (NMP), which is a common solvent, is both toxic and combustible, requiring NMP to be collected at low concentrations and condensed to be stored. The lower explosive limit (LEL) of NMP in the air is 1.3 vol%, and the upper explosive limit is 9.5 vol%.[8]

The research conducted on drying electrodes is limited, and the research in different drying technologies is even more so[10]. Freeze-drying has been suggested as a potential substitute for current drying methods such as vacuum ovens or convective air drying as it is widely used in food and medicine preservation[6;11]. This is due to freeze-drying producing highly porous

materials with a long shelf-life[12]. Freeze-drying of electrodes for lithium-ion batteries has been researched on anodes and cathodes with water as solvents[13;14;15;16;17]. This research also proved that freeze-drying could provide low tortuosity electrodes with great electrochemical performance due to the porosity of the structure. It is still unknown how solvents such as NMP acts in freeze-drying.

1.2 Aim of this work

The aim of this work is to investigate the possibility of using freeze-drying technology to dry NMC_{622} cathodes for lithium-ion batteries (LIBs). As the drying process of electrode production is highly energy-consuming, investigating possible alternative drying methods could provide a more sustainable battery production. Freeze-drying technology is known to give the dried material a high porosity compared to other conventional drying methods, which is crucial in electrodes for high ion mobility and fast charging ability. The goal is to determine whether freeze-drying will remove a sufficient amount of solvent from the material and leave a porous structure without damaging the material and its electrochemical performance. Freeze-dried electrodes will be tested electrochemically with galvanostatic cycling with potential limits (GCPL) and electrochemical impedance spectroscopy (EIS) and compared to reference electrodes. This will allow for determining the differences in cyclability and resistance within the electrodes. Unused electrodes will also be characterized with a scanning electron microscope (SEM) and Fourier transform infrared spectroscopy (FTIR) to find out how freeze-drying compares and potentially deviates from the reference.

2 Theory

2.1 The fundamentals of the Li-ion battery

The Lithium-ion battery (LIB) was first patented by Sony in 1991[18]. Lithium had been researched as a potential component in electrochemical cells, due to its lightness, stability in non-aqueous solutions, and electronic configuration, which eventually led to the commercialization of LIBs. The LIBs have high cycle life, high gravimetric capacity, and high volumetric capacity, which are all desired qualities in a battery[18].

2.1.1 The working principle

The LIB is an electrochemical cell that stores and converts electrochemical energy into electric energy. The battery consists of a cathode and an anode on current collectors separated by an electrolyte. Due to the nature of the electrolyte, which has high ionic conductivity, but low electronic conductivity, the ions travel through the electrolyte from one electrode to the other. At the same time, the electrons generated by the chemical reactions are forced through an external circuit connected to the current collectors[18]. They are then used to extract electrical energy. A separator is placed between the anode and cathode, soaked in the electrolyte, which allows the Li^+-ions to migrate across while preventing the electrodes from physical contact with each other[18]. A general schematic of the LIB is presented in Figure 2.1.

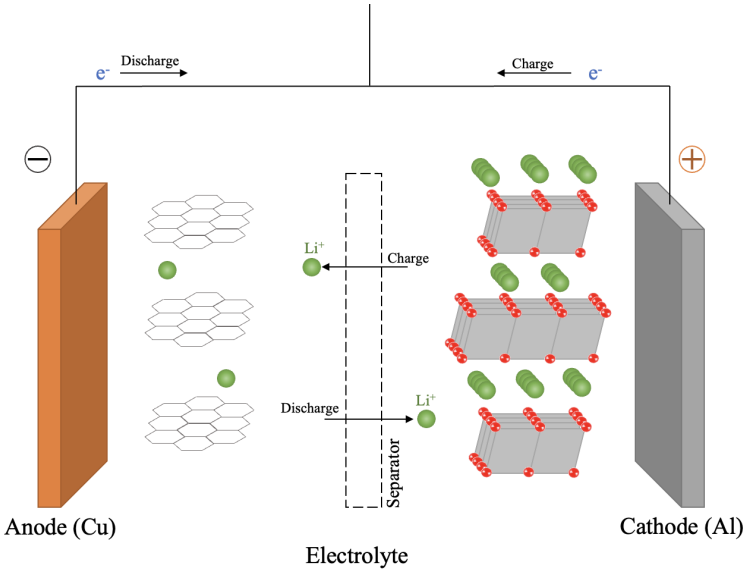

Figure 2.1: Schematic of the rechargeable LIB with a graphite anode and a $LiCoO_2$ cathode[18].

As the LIB is a rechargeable battery, both electrodes must be suitable for storing and releasing lithium quickly. To do this, the LIB does not contain Li-metal, but Li-ions that can be stored in both electrodes[18]. The battery goes through reduction-oxidation (RedOx) reactions to release and capture the lithium from one electrode to the other. During charging the cathode is oxidized, generating Li^+-ions into the electrolyte, and the anode is reduced, capturing the freed Li^+-ions into the structure. During discharge, this process is reversed[18].

2.1.2 Important terms and parameters

Here are the explanations of terms and parameters that are important when discussing batteries.

Capacity [Ah]: The total amount of charge possible to store in a battery. The capacity, Q, can be defined as the current, I, passed over time, Δt, according to Equation 2.1[18],

$$Q = \int_0^{\Delta t} I dt \tag{2.1}$$

Coulombic efficiency [%]: Describes the capacity fade in one charge/discharge cycle. It is defined by how much charge can be extracted during discharge, Q_{dis}, compared to how much energy is needed to charge a battery fully, Q_{ch}, as displayed in Equation 2.2[18],

$$\mathrm{CE} = 100\% \cdot \frac{Q_{dis}}{Q_{ch}} \tag{2.2}$$

C-rates : The current it takes to charge/discharge the cell completely within a set time. A C-rate of nC is the current needed to fully charge/discharge the battery in $1/n$ hours[18].

Cycle life : It is the number of charge/discharge cycles a battery can undergo before the capacity reaches 80 % of its initial, reversible value[19].

Intercalation of lithium : The reversible process of lithium migration into a layered host structure[19].

Irreversible capacity losses (ICL) [%]: The capacity losses after one charge/discharge cycle. It is defined as the deviation from CE = 100 %[20]. ICL is defined by:

$$\mathrm{ICL} = 100\% - \mathrm{CE}, \tag{2.3}$$

Open-circuit voltage [V]: This is the potential difference between a cathode and anode of a battery when no current is being drawn. This is defined by the electrochemical potential difference of the anode, μ_A^i, and cathode, μ_C^i, divided by the number f moles of electrons transferred, n and Faraday's constant, F as displayed in Equation 2.4[18],

$$V_{\mathrm{OC}} = -\frac{1}{nF}(\mu_A^i - \mu_C^i) \tag{2.4}$$

Shelf life [years]: The amount of time a battery can be stored before it is unusable[18].

Specific capacity [Ahkg$^-$1]/[mAhg^{-1}]: The theoretical maximum charge that can be stored for a specific material, which is calculated by Faraday's law in Equation 2.5 bellow[18]. For NMC this is 160 mAh g^{-1} [21].

$$Q_{\mathrm{th}} = \frac{1000 \cdot nF}{3600 \cdot M_{\mathrm{W}}} = \frac{26.8}{M_{\mathrm{W}}} \cdot n \tag{2.5}$$

Specific energy [Whg^{-1}]/[Whm^{-3}]: The amount of energy a battery can provide. This can be expressed as either the gravimetric specific energy [Wh g^{-1}] or volumetric specific energy [Wh m^{-3}][21].

2.2 Electrode materials

Lithium was first researched as an anode in lithium metal batteries due to its low reduction potential and lightness. However, lithium batteries are not suitable for rechargeable batteries due to the formation of lithium dendrites after extended cycling, which impacts cell performance[22]. This is the reason lithium-ion batteries (LIBs) were created, and the research on suitable electrode materials for rechargeable batteries began. Both electrodes in a LIB must be able to intercalate Li^+, one during charge and one during discharge[18]. The more Li^+ an electrode is able to lithiate and subsequently delithiate determine the power density of the battery. A high power density means less material used and lighter batteries[18]. Some electrode materials are displayed in Figure 2.2

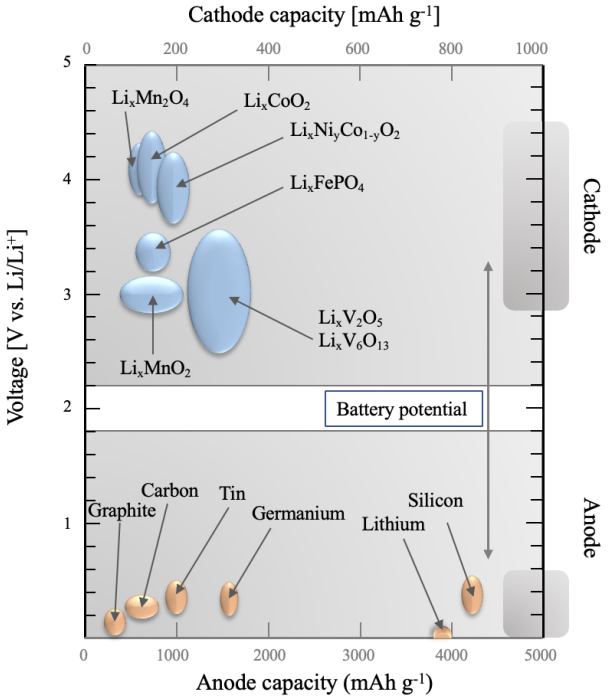

Figure 2.2: Potential- and capacity range of different cathode and anode materials used in lithium-ion batteries[23].

2.2.1 Anode materials

The anode in a LIB is the electrode that is lithiated upon charging. Julien et al.[18] determined several properties an ideal anode should have for optimal performance. These are as follows:

1. Have a small weight and accommodate as much Li^+ as possible for high gravimetric

capacity.

2. Have a small potential with respect to Li^0/Li^+ to increase the total potential of the cell as the anode potential is subtracted from the cathode potential.

3. Possess good electronic and ionic mobility so that electrons and ions can easier travel through the electrode.

4. Not be soluble in the electrolyte solvent and not react with the electrolyte salt.

5. It should allow the lithium to be inserted and extracted from the material without compromising the electrode structure

6. Be cheap, safe to use, and environmentally friendly.

The first commercial LIB used graphite as an anode taking advantage of the layered structure of the material[24]. The most common anode material in today's LIBs is still graphite which cycles between C and LiC_6, reaching a theoretical specific capacity of 372 mAh $g^{-1}$for reversible intercalation of Li-ions into graphite[18]. This is not a very high capacity, or high amount of Li^+ compared to C, leaving the first requirement lacking. It full-fills requirements two and three well, as it has a potential of only 0.005-0.2 V vs Li^0/Li^+, an electronic conductivity of 10^{-3} S cm^{-1}, and ionic mobility of $10^{-8} - 10^{-10}$ cm s^{-1}[18]. In addition to the lower-than-desired capacity of graphite, the fourth requirement poses a challenge as it also reduces the electrolyte on the surface of the electrode and forms a solid electrolyte interphace (SEI) layer[18]. This is due to the intercalation of Li^+ into graphite happening at a lower potential than the stability potential of the electrolyte. By using EC in the electrolyte, the SEI layer becomes stable enough to keep its shape and form a passifying layer, hindering more electrolytes from reducing[18]. The migration of ions through the SEI to the anode is suggested as the limiting reaction in the charge/discharge cycle and therefore the battery performance overall depends on the SEI having high ionic mobility[25]. This is considered a necessary evil when using graphite anodes. While the Coloumbic efficiency is reduced during the first couple of cycles, it will stabilize for the rest of the lifetime.

Another suggestion for anode material is silicon. This material has two highly desired properties; it is cheap and has a capacity of 4200 mAh g^{-1} as it is cycled between Si and $Li_{4.4}Si$. It has a potential of 0.3-0.4 V vs. Li^0/Li^+, which would fulfill the second requirement for a good

anode[18;26]. The main challenge with Si is the change in volume between Si and $Li_{4.4}Si$. As the volume increases 400% during intercalation of Li, the electrode can experience cracking and pulverization of Si particles causing a disconnect from the current collector and other conductive material[27;26]. During cycling, this is observed as high irreversible capacity losses and a decrease in efficiency[26].

2.2.2 Cathode materials

The cathode is the electrode that is lithiated upon discharge. Compared to anode materials, there is a large selection of potential cathode materials, as seen in Figure 2.2. A list of parameters for an ideal cathode is given as follows[18]:

1. Have a high oxidation potential in regards to Li^0/Li^+ to increase the total potential of the cell.
2. Have a high number of available lithium sites to accommodate as much lithium into the structure as possible.
3. It should have a reverse reaction with lithium, allowing the lithium to be inserted and extracted from the material without compromising the electrode structure.
4. Possess good electronic and ionic mobility so that electrons and ions can easier travel through the electrode.
5. Not be soluble in the electrolyte solvent and not react with the lithium salt in the electrolyte.
6. Be cheap, safe to use, and environmentally friendly.

It has proven a challenge to find a cathode that fulfills all the requirements to a satisfactory degree. Many different materials have been researched after the invention of the first LIB, which used lithium cobalt oxide, $LiCoO_2$ with a capacity of 130 mAh g^{-1}as it is only able to intercalate 0.5 Li/Co reversibly[28].

Most cathodes have a theoretical specific capacity between 140-200 mAh g^{-1}, which is quite low compared to the anode capacity as seen in section 2.2.1. According to Julien et. al., this low capacity has more of a limiting effect on the cell capacity than the anode capacity[18]. In Figure 2.3 it can be seen that after the capacity of the anode reaches ca. 500 mAh g^{-1}, the total

cell capacity does not increase much further until the cathode capacity is increased[18]. This gives incentive for developing cathodes with higher capacity which is why there are many more options for cathode materials than for anode materials.

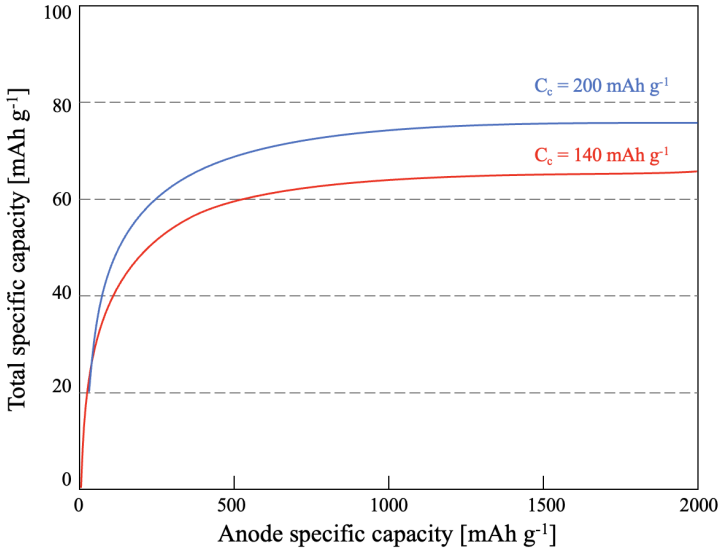

Figure 2.3: The total cell capacity of an 18,650 Li-ion cell as a function of anode capacity for two different cathode capacities; 140 mAh $g^{-1}$and 200 mAh g^{-1} [18].

Layered $LiMO_2$ compounds such as $LiCoO_2$, $LiNi_xCo_yO_2$, and $LiNi_xMn_yO_2$ has all been evaluated as potential cathode materials in rechargable batteries[29]. They have the same structure, α-$NaFeO_2$ which means that the MO_2 forms stacking layers with edge-sharing MO_6 octahedral with Li in between the layers. However, all these materials have their short-comings, such as low specific capacity, low thermal stability, toxicity, low conductivity, or a combination of these[28].

2.2.3 NMC cathodes

After the $LiNi_xMn_yO_2$ and $LiNi_xCo_yO_2$ had been evaluated for use in batteries, a hypothesis was presented that combining these two materials into one could make up for the shortcomings[28]. NMC, which is short for Lithium Nickel Manganese Cobalt oxide $LiNi_xCo_yMn_zO_2$, is often written as NMC_{xyz} where x, y, and z are the ratios of the nickel-, cobalt-, and manganese-ions. NMC has a similar layered structure as the $LiCoO_2$ in Figure 2.1[30]. The Ni-, Co-, and Mn-ions are surrounded by six oxygen atoms each in an octahedral structure in layers. Li-ions are seated in between the layers of these structures[31]. NMC was first synthesized and char-

acterized in 1999 by Liu et. al[32]. They tested different configurations of NMC and found that NMC_{721} performed better than NMC_{622} and NMC_{523} in terms of cycle life and capacity retention during the first 10 cycles[32]. Further studies were done on different configurations by Lee et. al[33]. which concluded that while NMC materials with high nickel content, such as NMC_{811} have a high specific capacity, the capacity retention decreases a lot quicker than materials with more cobalt and manganese such as NMC_{433}.

NMC provides a higher capacity than $LiCoO_2$ with a lower amount of cobalt. It is also able to intercalate more lithium-ions without the volume expansion experienced by $LiCoO_2$[28]. NMC has a specific capacity of 140-200 mAh g^{-1}depending on the nickel content[34]. Common configurations are NMC_{111}, NMC_{442}, NMC_{622}, and NMC_{811}. The capacity of the cathode will increase with the nickel content, however, this will also affect the capacity retention[35]. As cobalt is toxic it is desired to keep the content of cobalt low, but removing it completely has been problematic as this slows the charging rate[28]. Cobalt has also been shown to be suppressing the migration of nickel to the lithium sites within the material[28]. The manganese content helps keep the production cost down and is also helping to keep the structural integrity of the material[32]. It is also found that excessive manganese doping will affect the quality of the cycle life[32].

NMC_{622} has a theoretical capacity of 160 mAh $g^{-1}$and can reach a reversible cell potential of 4.3 V. When going above this to 4.4 V the cathode will start releasing oxygen and corrode[36]. It has lower thermal stability than NMC_{442} and NMC_{532}[37].

2.3 Fabrication of cathodes

Electrodes are typically prepared from powders and solvents. In addition to the active material, a conductive material, such as carbon black, and a binder are combined with a solvent[6]. For cathodes, the typical binder is polyvinylidene fluoride (PVDF) and the solvent is NMP[18]. However, PVDF provides environmental and toxicity issues. As it is a fluorinated material, and soluble in organic solvents, it provides dangers for humans and animals. Also, NMP provides an environmental issue as it is very corrosive when in contact with water, even at small concentrations of 2 % NMP[18]. NMP does also reduce fertility and affects the nervous system. This means that NMP can not be released into the atmosphere, but must be collected and handled appropriately by the factories. Currently, as the electrode dries, the NMP that evaporates must

be collected by an extractor.

After combining the components into a homogeneous mixture called a slurry, it must be deposited onto the current collector. This can be done in three ways; casting, coating, or printing, illustrated in Figure 2.4.

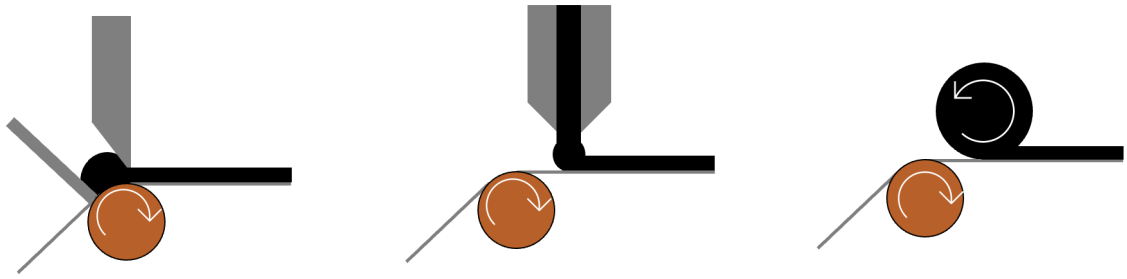

(a) (b) (c)

Figure 2.4: Illustrations of the different ways to deposit the slurry onto the current collector: a) Casting by doctor blade, b) Coating by slot die, and c) Printing by a roller[38]

Casting the electrode mixture onto a current collector is done utilizing a "doctor blade", a tool with a gap of a certain height used to smear the mixture at a constant thickness onto the current collector. It can be used to produce films as thin as 5 µm[18]. After casting the electrode is moved to dry. In the second process, the coating from a reservoir is squeezed through a slot-die onto the current collector. The slot is perpendicular to the current collector, and to achieve a uniform cast, the coating bead that fills the gap between the slot-die and current collector must be stable[18]. Lastly, printing is generally done by deposition rollers with the slurry mixture and rolling it onto the current collector. Here precision is also important to make a uniform cast, as well as optimizing the adhesion strength between the substrate and film to avoid delamination[18].

2.4 Drying of electrodes

After the slurry has been deposited onto the current collector, the electrode is dried until all the solvent has evaporated. Depending on the solvent, the energy required for the electrode to dry completely is different. The energy used to dry a graphite anode using water as a solvent is much lower than for cathodes using NMP as a solvent[6].

The drying process can be explained in different ways, this report will use the two-period ex-

planation. The first period is when the solvent at the surface of the substrate is evaporated. This is when ca. 90 % of the solvent is removed. The second period is when the solvent within the pores is removed. The solvent has to travel through the substrate to the surface where it can evaporate, either through diffusion or capillary forces[11]. The second drying period is very energy intensive as there is a need for an extra force to drive the solvent to the surface for evaporation. After the slurry is applied to the current collector the solvent will start to evaporate and a semirigid skeleton will be established by the particles. Some pores will empty out due to evaporation and the remaining pores will deliver more solvent to the emptying ones due to capillary forces. As this process continues with constant evaporation, the smaller particles are forced toward the surface along with the solvent. The result is a non-homogenous electrode with an accumulation of smaller particles towards the surface[39]. An illustration of the drying process can be seen in Figure 2.5.

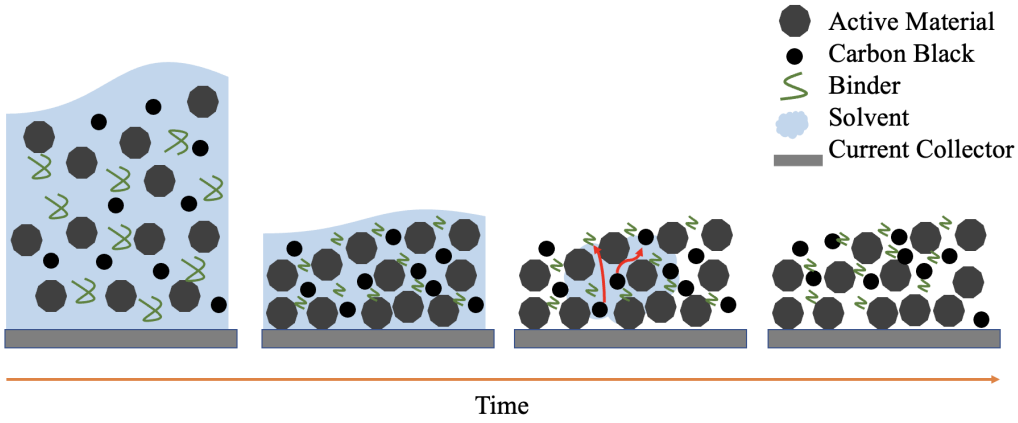

Figure 2.5: An illustration of drying mechanism of an electrode over time[39;6].

Currently, the most common drying technique in commercialized production is drying at 60-120 °C in a low-pressure environment with the option of an inert gas supply, where capillary forces are responsible for solvent migration[9;6]. An illustration of this drying process is displayed in Figure 2.6

Some research has been done on Near-Infrared (NIR) drying of graphite anodes and spinel cathodes which displayed a longer lifetime[41;42]. The graphite anodes show a good particle distribution post-drying while an increased drying speed[41]. The spinel cathodes showed an improved electrochemical performance, especially in thin film cathodes, at a moderate heat flux[42]. NIR drying also shows a higher drying efficiency than convective drying[43].

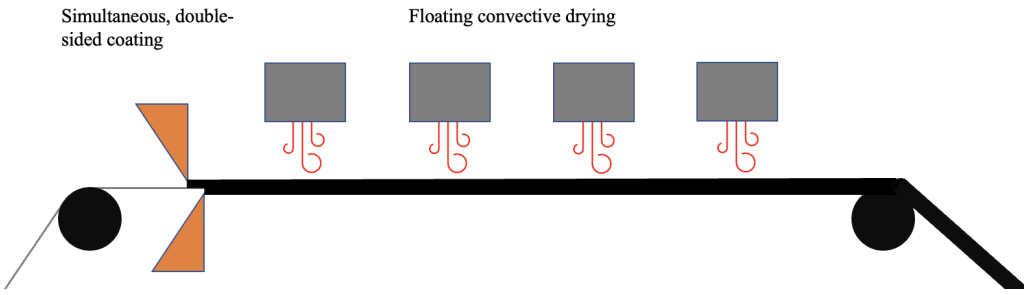

Figure 2.6: Schematics of a possible drying process used in commercial production of electrodes[40;6]

The drying process can have a big impact on the properties of the electrode cast, such as active layer adhesion to the current collector (CC), homogeneity, and electric conductivity[10]. This is related to the binder migration that happens at high drying rates, which results in the accumulation of the binder, and subsequently, other small particles such as the conductive material carbon black, at the surface of the electrode[44;45;41]. This migration can cause lowered adhesive effects of the active material (AM) to the CC as well as the electron transport at the AM-CC interface. This will then affect the electrochemical reaction on the AM-surface and raise the cell overpotential[39]. It is hypothesized that the capillary forces responsible for pushing the solvent to the surface are responsible for this migration of smaller particles, and while this is probable it has not been satisfactorily proven[46;10]. As the binder accumulated towards the surface a concentration gradient is created which triggers back diffusion of binder into the substrate. The amount of back diffusion is determined by the drying time; longer drying time at low heat gives ample opportunity for the binder to migrate back into the substrate and reach a balance in the concentration gradient. The molecule size of the binder is also a determining factor as larger molecules will not as easily diffuse back into the material.[46] Additionally to binder migration, high drying rates over a long period of time can damage the binder and subsequently the electrode structure[47]. Having lower temperatures, around 80 °C, can increase the binder distribution in the substrate[39].

2.4.1 Freeze Drying

Freeze drying, or lyophilization, is the process where the medium of suspension is crystallized at a low temperature before the solvent is sublimated and removed as a vapor[11]. These three main stages are illustrated as a phase diagram in Figure 2.7.

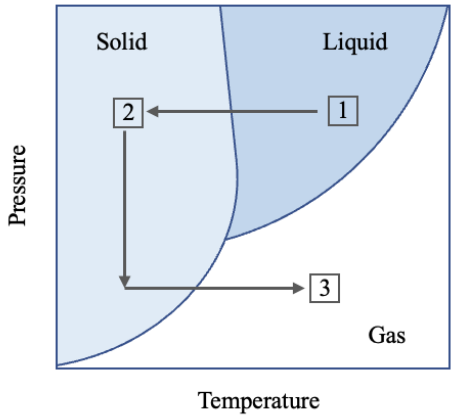

Figure 2.7: A phase diagram of a solvent with the process of freeze drying: a) The solvent is keeping all the particles in suspension, b) The solvent is frozen, and c) The solvent sublimates and is carried away in vapor phase[48].

The drying in itself only occurs during sublimation from solid to vapor and diffusion is the force responsible for the removal of the solvent within the substrate as opposed to capillary forces in vacuum drying[49]. Similarly to the vacuum oven drying process, there is a primary- and secondary drying stage. In the primary drying stage, the solvent on the surface will be removed first, creating a sublimation interface. This interface moves from the surface into the material as more of the solvent sublimates and diffuses towards the surface[49]. As the solvent is removed, it leaves behind pores created by the crystals of solvent during freezing[50]. During the secondary drying stage, the bound solvent is removed from the substrate by desorption. This is usually around 10-35% of the total solvent[49]. At this point, the substrate has become a eutectic mixture, which is a homogeneous mixture with a lower melting point than its components, where the mixture is unwilling to release the solvent as it has reached a stable state. Without being supplied with more energy the mixture will not leave this stage. Here, the temperature can be increased to give the solvent enough energy to be released from the substrate[50]. However, materials with low diffusion within the material, such as glassy products, need to be carefully kept below the collapse temperature to avoid deformation[49]. The collapse temperature is the temperature at which the porous structure will start to melt and deform[12]. This stage is recognized as the rate-determining step in freeze drying, as the time it takes to remove the bound solvent can be as long or longer than the removal of the free solvent[49]. Freeze-drying processes at the industrial scale is a relatively slow process due to the very slow mass and heat transfer rates that can be achieved under vacuum by providing the heat for sublimation without exceeding the

triple point[51;52]. Freeze-drying has been prominent in the food and pharmaceutical industries as a means of preservation[11]. This is due to freeze-dried materials keeping high porosity and color of the material without sacrificing taste and texture[53].

As porosity is crucial for the wetting ability of an electrolyte in a battery, studies have been conducted on applying the freeze-drying method to battery technology to achieve better porosity and tortuosity properties, the importance of which will be discussed in section 2.6. Freeze-drying was first tested in the synthesis of different cathode materials. The powders produced using this drying method have shown a more uniform pore distribution, improved electrochemical properties, and lower tortuosity than their respective normal synthesis routes[54;55;56;50]. Many of these materials are normally prepared in aqueous mediums, which have poor stability, and freeze-drying has been considered as a way to improve the long-term stability of colloidal particles[57].

In 2017, Ghadkolai et. al. used freeze-tape-casting in the production of $Li_4Ti_5O_{12}$ (LTO) anodes for LIBs, which has the mechanism of freeze-drying, except that the tape-cast plate has a very low temperature. These cathodes showed high porosity and low porosity. They also performed better electrochemically than the normal ones with the same loading, despite being almost twice as thick[16]. It has long been known that the properties of the final dried material, depend on the temperature during freeze-drying[53]. Ghadkolai et. al. experienced this as well as they tested different temperatures raging from -140 to -160 °C during the freeze-tape-casting, and the electrodes manufactured at -150 °C performed the best[16]. After this, there have been several success stories of freeze-drying being used in electrode production. In 2018 Delattre et. al. produced $LiNi_{0.8}Co_{0.15}Al_{0.05}O_2$ (NCA) cathodes also through freeze-tape-casting and experienced similar results as Ghadkolai[13]. The cathodes had low tortuosity and better electrochemical performance than the normal cathodes[13]. In 2019 Hwa et. al. produces sulfur electrodes for lithium-sulfur batteries, which experiences as little as 4 % decay in a capacity of 200 cycles[14]. Dang et. al. produced graphite electrodes that had over 8% higher capacity retention after 90 cycles at C/5, and better rate capability at 60% higher capacity at 1C, than the electrodes prepared by the normal tape-casting method[58]. Lastly, Liu et. al. produced freeze-dried $LiFePO_4$ electrodes which showed better capacity retention than the electrodes produced in the conventional way[17].

All the electrodes produced by freeze-tape-casting and freeze-drying used water as a solvent,

except for the latter which used a mixture of 1,4 dioxane and water. $LiFePO_4$ usually uses NMP as a solvent in manufacturing, however, NMP has a very low melting point of -24 °C while 1,4 dioxane has a melting point of 11.8 °C[17]. As water, with a melting point of 0 °C, needed to reach -150 °C in freeze-tape-casting to produce the best results, it is theorized that NMP would need to reach even lower temperatures[16;17]. Some of the different properties of different solvents are given in Table 2.1.

Table 2.1: Physical properties of different solvents used in electrode production.

Solvent	Melting point [°C]	Boiling point [°C]	Density (liquid) [g cm^{-3}]	Density (solid) [g cm^{-3}]
Water[59]	0	100	1	0.917
NMP[60]	-25	202	1.027	-
1,4-dioxane[61]	11.8	101.2	1.033	-

2.5 Electrolytes

The electrolyte in a LIB is supposed to be a conductor of the ions migrating between the electrodes during charge and discharge. The mobility of the ions in the electrolyte determines the charging rate of the battery[62]. There are different kinds of electrolytes such as aqueous, non-aqueous, semi-solid, and solid[63]. As with electrode materials, there are some general properties that are wanted in an ideal electrolyte. Firstly, the electrolyte should have a large window of phase stability and a large window of electrochemical stability. It should also be non-corrosive and resistant to various abuses. It should have the good wetting ability and low viscosity. Lastly, it is preferable for it to be non-flammable, non-toxic, and abundant[18].

The window of phase stability is the band gap, E_g, which is illustrated in Figure 2.8. It is important for the open-circuit voltage, eV_{OC}, to fall within this window to avoid the degradation of the electrolyte. For the electrolyte to remain stable the μ_A must be below LUMO of the electrolyte and μ_C be above the electrolyte HOMO[20]. Should μ_A or μ_C fall outside the electrolyte window, the electrolyte can be degraded through reduction at the anode electrode-electrolyte interphace leading to the formation of a solid electrolyte interface (SEI) or oxidation at the cathode electrode-electrolyte leading to the formation of cathode electrode interface (CEI)[20;63]. For materials such as graphite anodes, the formation of an SEI is desired to protect

the electrolyte as a passivating layer, as long as the SEI is stable[18].

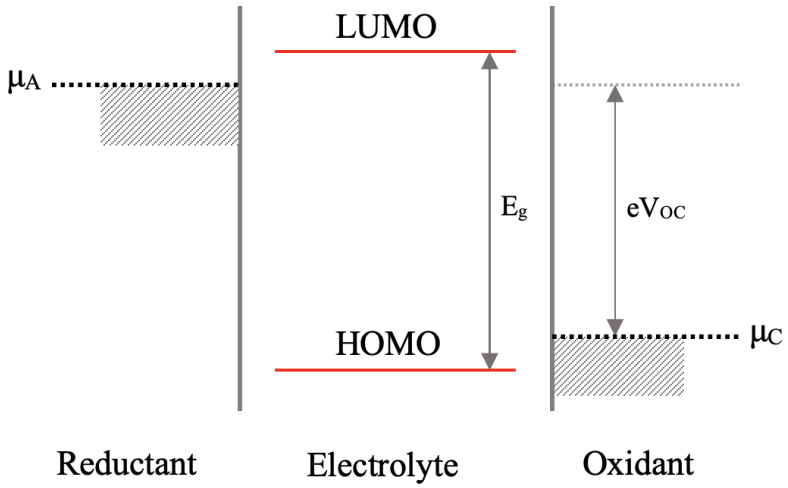

Figure 2.8: Illustration of the stability window of a liquid electrolyte. The band gap, E_g, of the electrolyte exceeds the difference in electrochemical potential between the anode and cathode, eV_{OC}, to remain stable[20].

Like with electrode materials, it is difficult to find an electrolyte that fulfills all these requirements. The electrolyte used in current commercial lithium-ion batteries consists of a salt dissolved in a non-aqueous solvent and additives. They have a large window of stability, but have a high vapor pressure which can provoke fires or explosions in certain cases[18].

2.5.1 Solvents

Electrolytes used in LIBs often employ a mixture of two or more solvents. This is due to different solvents having different contradictory properties, such as fluidity vs. high dielectric constant, which when used together achieve various aims simultaneously[18]. For example, adding ethylene carbonate (EC) to propylene carbonate (PC), dimethyl carbonate (DMC) or other similar solvents will improve the stability of the SEI layer on the anode[64;65]. The EC/PC electrolyte was used in the first commercial rechargeable battery[62], and in 1994 the EC/DMC electrolyte emerged. It had a better performance in both cycle life and self-discharge, as well as better electrochemical stability against oxidation[66]. This quickly became the state-of-art electrolyte used in lithium-ion batteries[62].

2.5.2 Salt

While there are many different solvents that can be used in rechargeable LIBs, there are significantly fewer salts that are suitable[62]. In LIBs the salt must contain lithium. It should be able to dissolve completely in the solvent, and the ions should be able to move with high mobility. The anion should be stable against oxidative decomposition at the cathode, inert to the solvents in the electrolyte, non-toxic, and remain stable against thermally induces reactions with electrolyte solvents and the cell components. The salt should also remain inert toward the other cell components[62].

It is found that salts with complex anions, such as in lithium hexafluorophosphate ($LiPF_6$) have the desired solubility. This is due to the anion F^- complexed by the Lewis' acid PF_5. The negative charge is being shared among the ligands in the Lewis' acid, lowering the melting point and increasing the solubility[18]. $LiPF_6$ is the most used salt on the marked, which has a conductivity of 10.7 mS cm^{-1}, second only to $LiAs_6$[67]. However, $LiPF_6$ is very sensitive to even small amounts of water, creating HF acids upon contact which corrodes the current collector[62]. Research is done on other salts which are less sensitive to water as an alternative to $LiPF_6$[18].

2.6 Electrode Morphology

2.6.1 Effect of porosity

The porosity, ε, of a material is defined as the amounts of pores within a material, and can be determined through equation 2.6[68]. The theoretical density is the density of the material if it has no pores, while the geometrical density is the measured density. Porosity is mostly discussed in connection to the anode performance in a battery cell, however as porosity is a parameter that must be considered in tortuosity determination, it is included here[68].

$$\varepsilon = 1 - \frac{\text{theoretical density}}{\text{geometrical density}} \tag{2.6}$$

The porosity of an electrode has an influence on how fast lithium ions from the electrolyte can diffuse into the electrode material during charge and discharge. This is due to porous electrodes having a smaller diffusion length than non-porous electrodes[68]. The diffusion length is the length of the pathway the lithium ions must take to reach an intercalation site and is related to

the diffusion time by equation 2.7.

$$t \frac{l^2}{D}, \tag{2.7}$$

where t is time, l is the diffusion length and D is the diffusion coefficient. A short diffusion time is wanted. There are two ways this can be achieved, either by reducing the diffusion length or increasing the diffusion coefficient. To do the latter, the material composition must change, so the former is the parameter relevant here. Using porous structured electrodes the diffusion length can be reduced. This is due to the pathways to intercalation sites being reduced, as the pores open up more paths. The pores allow the electrolyte to penetrate deeper into the material, and for more of the active material to be used. They also increase stability as the volume expansion happening as Li-ions intercalate into the material, has a smaller chance of damaging the structure[68].

2.6.2 Effect of tortuosity

Tortuosity is a parameter used to describe the length a lithium-ion must travel through the electrode material. As this parameter gives information about the pathway an ion will take, it will also indicate how the electrolyte will diffuse into the electrode pores, which again influences the charge and discharge rate of an electrode[69]. Tortuosity is defined as the elongation of transport path ion travels due to a porous structure, L_c, with respect to a straight line, L, as described by equation 2.8[69].

$$\tau = \frac{L_c}{L} \tag{2.8}$$

Should the ion travel in a straight line, the tortuosity will be 1, and if the value is larger than one, the pathway will be longer than the straight line. Low tortuosity electrodes will experience better cycling ability and faster charging as the ions more easily can travel through the material[69].

The microstructure of an electrode decides how the electrode will behave in bulk. The MacMullin number expressed in equation 2.9[30] is a common parameter used to describe how the porosity in an electrode or separator influences macroscopic conservation laws[69].

$$N_M = \frac{\tau}{\varepsilon} = \frac{\sigma}{\sigma_{ion}} \tag{2.9}$$

Here τ is the tortuosity, ε is the porosity, σ is the conductivity of the electrolyte, and σ_{ion} is the ionic conductivity of an electrode or a separator. Ohms law in equation 2.10, where the resistance is R, the conductivity is σ, the area of the electrode is A, and the thickness of the electrode is d, can be combined with equation 2.9 to create equation 2.11 [30]. Using values obtained from electrochemical impedance spectroscopy (EIS) measurements, equation 2.11 can be used to calculate the tortuosity of an electrode. The factor of 1/2 is added to the equation due to the EIS measurement using a symmetrical cell.

$$R = \frac{d}{\sigma_{ion} \cdot A} \tag{2.10}$$

$$\tau = \frac{R_{ion} A \sigma_{ion} \varepsilon}{2d} \tag{2.11}$$

2.7 Electrochemical measurements

2.7.1 Galvanostatic cyclic

Galvanostatic cycling with potential limitations is a method of determining battery performance. It is widely used when characterizing batteries as a wide range of parameters can be measured such as Coloumbic efficiency, discharge capacity, and charge capacity at different times or potentials. When cycling, a constant current is applied, with a charge and discharge rate determined by the c-rate of the active material, until a set potential limit is reached [70].

2.7.2 Electrochemical impedance spectroscopy

Electrochemical impedance spectroscopy measurements is used as a means to measure the opposition to electric currents in materials [71]. For DC systems the opposition to electric current is same as resistance. For AC systems the opposition or resistance to electric currents are expressed in terms of an impedance. The impedance is normally represented by complex numbers accounting for phase shifts of the AC current. Thus, in impedance determination both the potential and current are frequency dependent parameters [71].

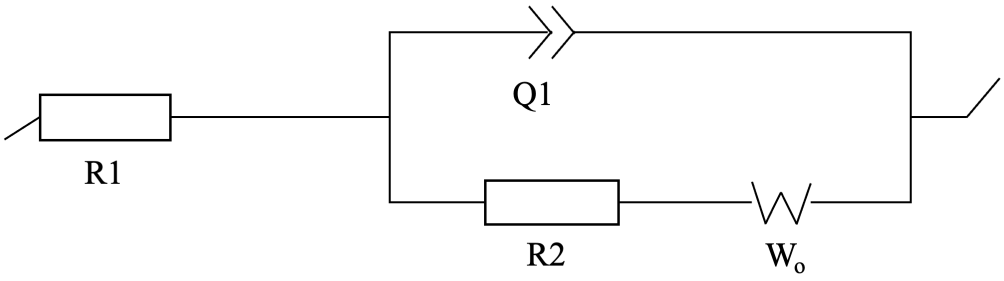

Figure 2.9: The Randles circuit which is an equivalent circuit for a battery. R1 is the resistance of the electrolyte, R2 is the resistance in the pores of the structure, W_o is the Warburg finite open coefficient, and Q1 is the constant phase element[].

Impedance measurements can be done by applying either AC potentials (PEIS) or currents (GEIS) at different frequencies while measuring the corresponding current or potential. In PEIS the current signal is the sum of sinusoidal currents which represents electrochemical processes. At high frequencies these processes are high rate electrochemical processes such as charge transfer. At low frequencies these processes are low rate electrochemical processes such as diffusion.[71]

By fitting the EIS experimental data to an ideal equivalent circuit, the resistance and capacitance of a battery can be determined. One of the simplest circuits that can be applied to a battery is the Randles circuit in Figure 2.9 which represents the ideal electrode/electrolyte interface.[69]

The Warburg coefficient represents the semi-infinite diffusion of a charged particle. Nyquist plots are used to illustrate the EIS data. The Nyquist plot of a Randles circuit is represented in Figure 2.10.

As mentioned in section 2.6.2, Electrochemical impedance spectroscopy (EIS) measurements can be used in tortuosity determination. This is done using a symmetrical cell, a cell with both working- and counter electrode of same material, weight and volume, and a blocking electrolyte[69]. The blocking electrolyte needs to be inert towards the electrode so it does not intercalate into the material. In this way the pore resistance will be related only to the transport of ions in the pores. Equation 2.12 shows how the impedance in the pores are related to the values attained from fitting the EIS data to the equivalent circuit in Figure 2.9.

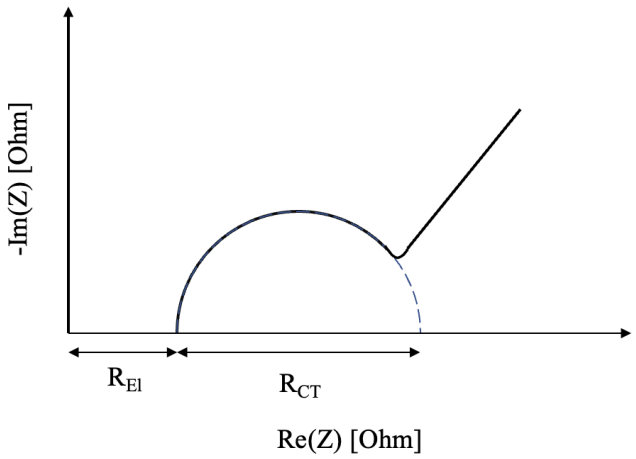

Figure 2.10: A simple Nyquist plot. R_{El} is the resistance in the electrolyte, R_{CT} is the charge transfer resistance[30].

$$Z_{pore} = R\frac{\coth(i\tau\omega)^{\alpha}}{(i\tau\omega)^{\alpha}} \text{ [72]} \tag{2.12}$$

2.8 Characterization

2.8.1 Scanning Electron Microscopy Imaging

Scanning electron microscopy (SEM) creates images using an electron gun as a probe. The material is bombarded with electrons that interact with the atoms and generates different signals such as Auger electrons (AE), secondary electrons (SE), backscatter electrons (BE), and X-rays. Different detectors are used to analyze the different signals[73]. The interaction volume is the depth and geometry of penetration by the electrons into the material, how large the interaction volume is, is determined by the accelerating voltage and the atomic number of elements within the samples. It is approximately pear-shaped and the depth of penetration from the electron beam determines which electrons are detectable as seen in Figure 2.11. The main kinds of signals the SEM can pick up are secondary electrons (SE), backscatter electrons (BE), and X-rays. Secondary electrons are the electrons knocked loose by the primary electrons emitted from the probe. The secondary electron signal does not penetrate deep into the material, but is sensitive to surface incline, making it suitable for analyzing topography[73]. Backscattered electrons are incidence electrons that escape the sample. They are used to give a better contrast between the individual elements in the material due to elements of higher atomic number releas-

ing more electrons creating visual contrast between elements. However, it cannot distinguish between exact elements, just if it is of a higher or lower atomic number[73]. X-rays can be used to identify exact elements in a material as every element generates unique energies. The X-rays can be detected by using Energy-dispersive X-ray spectroscopy (EDS) and the exact element can be determined[73].

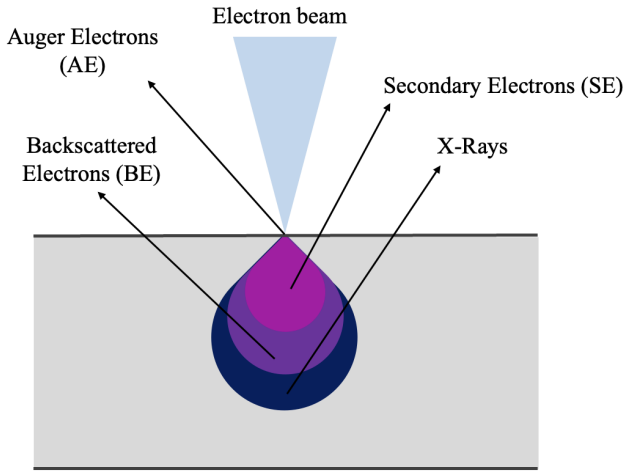

Figure 2.11: Interaction volume of a material from an electron beam[73]

The resolution of the SEM image can be affected by changing some parameters, mainly accelerating voltage and working distance. The accelerating voltage is the voltage that controls the electron beams depth into the sample. Higher voltage gives a larger interaction volume but causes decreased resolution due to the surface electrons dissipating. The working distance determines the depth of field compared to the resolution of the sample. A shorter working distance gives better resolution at the cost of the depth of field.

2.8.2 Focused Ion Beam

A focused ion beam (FIB) utilized a focused ion beam to sputter away material at the micro- or nanoscale allowing for accurate cuts into the sample[74]. The most common FIB uses Gallium ions to cut the samples, however, other FIBs exist such as Plasma-FIB (PFIB). The PFIB is a lot faster than the conventionally used Gallium-FIB, due to it being capable of handling higher voltages and having lower contamination of the sample. However, the PFIB is not as accurate as the Gallium-FIB. A SEM is included in the FIB allowing for easy characterization of the indent.

2.8.3 Fourier Transform Infrared Spectroscopy

Fourier transform Infrared Spectroscopy (FTIR) is used to detect chemical bonds present in a sample[75]. The chemical bonds undergo vibrations in the form of stretching or bending when exposed to energy. As molecular vibrations absorb infrared (IR) radiation, FTIR utilized that each chemical bond vibration has a different frequency[75]. The IR radiation in the sample produces a spectrum by measuring an interferogram of the sample surface. As IR radiation is applied to the sample, vibrations of the chemical bonds occur which absorb light at certain wavelengths. The interferogram experiences a reduction in amplitude which is then Fourier transformed into an IR spectrum[76]. IR radiation covers electromagnetic radiation over large frequencies, however, the mid-infrared with frequencies of 4 000 to 400 cm^{-1} are used to create the characteristic electromagnetic spectrum referred to as FTIR spectrum[76]. There are also vibrational nodes that cannot be detected by FTIR as they are IR inactive[75]. Detectable molecules that are of importance for this thesis are given in Table 2.2 with their respective frequencies.

Table 2.2: FTIR vibrational frequencies of different components

Bond	Vibration [cm^{-1}]
CF_2	1299[77] 1146[77] 830[78]
CH_2	1453[79] 870[78]
CH_3	3000-2800[77]
CH	1400[80] 1000-700[80]
C=O	1745[80]
CN	1660-1615[80] 1200[80] 1100[80] 1000[80]
C=C	1615[80]

3 Experimental

This section will explain the preparation and execution of the experiments conducted. It will explain the fabrication of cathodes, the drying processes, and the characterization methods used to evaluate said drying processes. As only $LiNi_{0.6}Co_{0.2}Mn_{0.2}O_2$, also called NMC_{622}, was used, this will be referred to as just NMC. There were made reference cathodes and freeze-dried cathodes which were characterized with the same instruments under the same conditions. This same slurry was used both for the reference cathodes and the freeze-dried cathodes. However, due to differences in available appliances in the different laboratories, they were not cast or dried in the same place.

3.1 Slurry production and tape casting

The NMC electrodes were made from a slurry mixture cast onto an aluminum foil current collector. The slurry mixture consisted of 90 wt% NMC (Targay), 5 wt% carbon black (Targay), and 5 wt% PVDF (polyvinylidene difluoride). Table B.2 displays the calculated amounts for the slurry mixture. The PVDF was dissolved in NMP (N-methyl-2-pyrrolidone) as a 5 wt% solution before adding it to the slurry mixture. It was created by weighing out 0.5 g PVDF and 9.5 g NMP and dissolving the PVDF in NMP overnight using a magnetic stirrer at 40 °C. Two batches were made to produce enough cathodes for the experiments.

Using a Thinky Are-250 mixer the components were mixed at 1500 rpm for 5 minutes before being mixed at 2000 rpm for 25 minutes. After mixing the slurry was inspected for the right flow properties. More NMP was added as needed and the slurry was mixed at 2000 rpm for 10 more minutes.

Using a RK K Control Coater 101 tape caster, the slurry was cast onto an aluminum foil current collector. The aluminum foil had a thickness of 15-20 μm. Both sides of the foil and the tape caster were cleaned with ethanol before use. The foil was held onto the tape caster by either vacuum or a clip and using a doctor blade with a 50 μm gap, the slurry was cast onto the current collector at a speed of 10. The casts were then either dried in a freeze drier at -61 °C and less than 5 mbar for at least four hours or left in an oven at 80 °C with a fan for one hour before drying in a vacuum oven overnight at 120 °C. The latter being the reference electrodes. The dry casts were cut into 16 mm diameter circles to be used as cathodes.

3.2 Electrolyte mixing

Two electrolytes were used in the experiments. The electrolyte used in the galvanostatic cycling of batteries was $LiPF_6$, which was pre-mixed and delivered by Sigma-Aldrich. The electrolyte used in electrochemical impedance spectroscopy was 0.01M, 0.01M, and 0.005 Tetramethylammonium bis(trifluoromethanesulfonyl)imide (TABTFSI, Sigma-Alrich) dissolved a in 1:1 weight ratio solution of ethylene carbonate (Sigma-Alrich) and dimethyl carbonate (Sigma-Aldrich). All the calculations used and exact measurements are given in Appendix B

First the 1:1 EC:DMC solution was made. EC was heated until liquid. EC was weighed out into an aluminum bottle. Afterward DMC was added to the aluminum bottle until a 1:1 weight ratio was reached. To a new bottle, enough TBATFSI was weighed out to give 10 mL of 0.1 mol/L solution, then 10 mL of the EC:DMC solution was added and the final solution was mixed overnight using a magnet stirrer. This was repeated twice for the 0.01 M and 0.005 M solutions of TBATFSI in EC:DMC with different amounts of TBATFSI.

3.3 Cell Assembly

Two types of cells were used in the experiments; coin cells and PAT cells. For galvanostatic cycling, coin cells were used. PAT cells were used for electrochemical impedance spectroscopy (EIS) measurements for both the freeze-dried and reference electrodes.

3.3.1 Coin cells

In this project, half cells were constructed as coin cells using Hohsen 2016 parts. The NMC electrode was used as the working electrode and a lithium disk as the counter electrode in the half cells. The NMC electrodes were cut into 16 mm diameter disks. The lithium was cut into 14 mm diameter disks. Microporous polypropylene Celgard 2400 disks of 18 mm diameter and 25 μm thick were used as separators and the spacers were 0.5 mm Hohsen spacers. The reference NMC cathodes were dried in the vacuum oven at 120 °C for 12 hours before being introduced to the glove box for cell assembly. The freeze-dried NMC cathodes were transported through the vacuum chamber without heating before being introduced to the glove box.

The half cells with both the reference electrodes and the freeze-dried electrodes were assembled according to Figure 3.1. 20 μL of 1M $LiPF_6$ in a 1:1 ratio of EC:DMC electrolyte was added on top of the electrode and another 20 μL on top of the separator before the lithium disk giving

a total of 40 μL electrolyte. Using an automatic coin cell crimper the cells were closed. The cells were left overnight to let the electrolyte wet the electrode and separator completely before cycling. 6 freeze-dried and 5 reference electrodes were made, the properties of which are presented in Table 3.1.

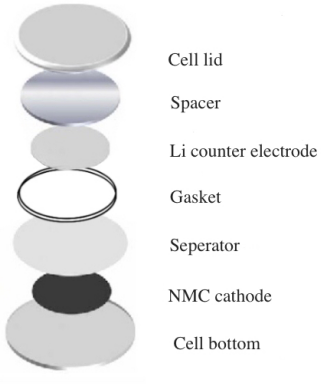

Figure 3.1: The construction of a coin cell with all components

3.3.2 PAT cells

The PAT cells were assembled according to Figure 3.2. All the electrodes used were 16 mm in diameter and the separators were microporous polypropylene Celgard 2400 disks with a diameter of 21 mm and thickness of 25 μm.

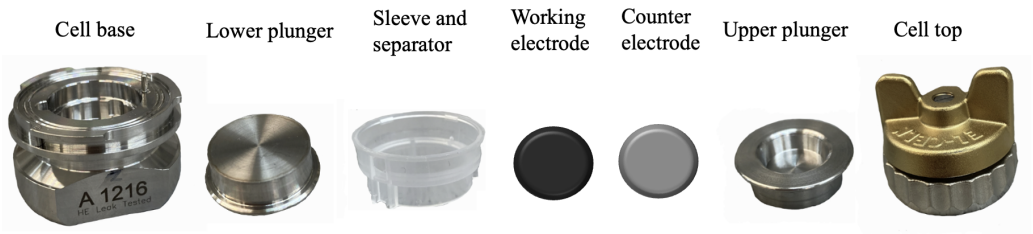

Figure 3.2: Construction of a PAT cell with all components[]

Both the lower and upper electrodes were NMC cathodes of equal weight and thickness from the same drying process. One of the two cathodes was placed in the middle of the lower plunger. A 100 ... lower plunger was used here as well. The separator in the gasket was placed on top of the bottom electrode and 100 μL of the electrolyte was applied on top of the separator. The electrolytes used were 0.01M and 0.005 M of TBATFSI in a 1:1 ratio of EC:DMC solvent. The

Table 3.1: Loading and theoretical capacity for the freeze-dried and reference cathodes used in coin cells.

Cathode		Loading [mg cm^{-2}]	Theoretical capacity [mAh]
Freeze-dried	1	3.03	0.97344
	2	3.09	0.99216
	3	3.31	1.06416
	4	2.65	0.85104
	5	3.90	1.2528
	6	3.34	1.07424
Reference	1	3.06	0.98352
	2	2.62	0.84384
	3	2.51	0.8064
	4	3.08	0.99072
	5	2.57	0.82512
	6	2.82	0.90576

second cathode was placed, facing down, onto the separator. The upper plunger was placed on the upper cathode and the PAT cell was closed and left for the electrolyte to wet the electrodes overnight. Four PAT cells were assembled. One of each concentration for the freeze-dried cathodes, and one of each concentration for the reference cathodes. The properties for the PAT cells are given in Table 3.2. The calculations of the densities are given in Appendix B.

3.4 Galvanostatic cycling with potential limits

The coin cells with the freeze-dried and reference cathodes were cycled using a Lahne battery cycler. Two different cycling programs were used. The cycling programs are specified in Table 3.3.

1 C is the current density required to discharge the battery completely in one hour, C/2 is the current density required to discharge the battery in two hours, C/10 is the current density required to discharge the battery in ten hours. This value is calculated from the theoretical value for the active material, NMC, which is 160 mAh g^{-1}. In total 3 freeze-dried and 3 reference

Table 3.2: Molarity of electrolyte and loading, theoretical capacity, geometric density, and thickness for the freeze-dried and reference cathodes used in PAT cells.

Electrode	Molarity [mol L^{-1}]	Loading [mg cm^{-1}]	Theoretical capacity [mAh g^{-1}]	Thickness [μm]	Porosity -
Freeze-dried	0.01	3.16 ± 0.00	1.0152 ± 0.0000	29.0 ± 2.0	0.527 ± 0.016
	0.005	3.01 ± 0.01	0.9655 ± 0.0007	29.5 ± 0.5	0.558 ± 0.008
Reference	0.01	2.63 ± 0.000	0.847 ± 0.0000	31.5 ± 0.50	0.637 ± 0.0058
	0.005	29.82 ± 0.004	0.959 ± 0.00144	32.0 ± 0.00	0.596 ± 0.0006

Table 3.3: The cycling program used during electrochemical testing of the coin cells

Program	Step	Current	Voltage	Cycles
1	1	C/10	4.3-3 V	2
	2	C/1	4.3-3V	50
2	1	C/10	4.3-3V	2
	2	C/2	4.3-3V	50

electrodes were cycled at each program, testing in total 6 freeze-dried and 6 reference cells.

3.5 Determination of tortousity

Electrochemical impedance spectroscopy (EIS) measurements were used to determine the tortuosity of the freeze-dried and reference cathodes. The experiments were performed in symmetrical PAT cells constructed according to section 3.3.2 with the electrolytes from section 3.2. The electrode surface area (A), electrode porosity (ε), and thickness (d) were known. The ionic resistance (R_{ion}) and ionic conductivity (σ_{ion}) were found by EIS measurements. The EIS measurements were performed between a frequency of 10 mHz and 150 kHz at an amplitude of 1 mV and 20 measuring points per decade. This was repeated for all four cells.

The results were fitted to the circuit seen in Figure 2.9 from Section 2.7.2.

3.6 Characterization

3.6.1 Electrode morphology

The surface morphology was analyzed using SEM on unused electrodes. Three freeze-dried and three reference cathodes were placed in a Plasma-FIB with SEM (Thermo Scientific) and evaluated at different magnifications using the SEM function. After the surface had been evaluated, the Plasma-FIB cut two cross-sections which were 150 μm long and 40 μm wide, through the electrode. The SEM function was used to evaluate the morphology of the cross-section. All SEM pictures were taken with secondary electrons at an accelerating voltage of 3kV with an emission current of 0.10 nA and a working distance of 4 mm.

3.6.2 FTIR

Analysis was also performed using Bruker Vertex 80V ATR-FTIR with a diamond crystal to determine if there was any possible NMP left in the freeze-dried cathodes. A scanner velocity of 10 kHz with an aperture of 6mm was used with the detector at room temperature. A scan range of 550-4000^{-1} was used with a resolution of 4 cm^{-1}. A total of 100 scans were performed.

To avoid too much signal from other components than NMP, the 5 % PVDF-NMP solution used in slurry production was used in place of the NMC cathodes. The solution was cast onto aluminum foil using the same tape caster for the slurry application. The casts were then dried in either the freeze-dryer for four hours or vacuum oven overnight like the NMC casts. A sample of each cast was cut out and analyzed in the FTIR. Pure PVDF powder was also analyzed and the spectrum was compared to the spectrum of the freeze-dried cast and the reference cast. A pure Al-foil sample was used as a background for the dried casts while a vacuum was used as a background for the PVDF powder.

4 Results

This section provides the results obtained for the freeze-dried and reference electrodes. Firstly the electrochemical testing results are presented. This includes the results from galvanostatic cycling and the electrochemical impedance spectroscopy measurements. Then the SEM imagine of the electrode surfaces and cross-sections are displayed before the FTIR spectra for the freeze-dried and vacuum dried 5% PVDF solution are presented.

4.1 Cell performance during galvanostatic measurements

This section presents the results obtained through the galvanostatic cycling of the half cells constructed with the freeze-dried and reference electrodes.

4.1.1 Capacities and Coloumbic efficiencies

Figure 4.1 and 4.2 show the charge and discharge capacities in mAh $g^{-1}$for each cycle during galvanostatic cycling of the freeze-dried and reference electrodes. Six cells of both freeze-dried and reference electrodes were tested, three of each with a C-rate of 1C and three of each with C/2. For all the cells the recorded charge capacity was at 4.3 V while the recorded discharge capacity was at 3.0 V for each cycle.

In Figure 4.1 the cells were cycled at a C-rate of 1C except for the two first cycles, which were formation cycles at a C-rate of C/10. The reference electrodes show a generally better performance in both charge and discharge capacity than the freeze-dried electrodes. All reported numbers in this section are the means of the three parallels of freeze-dried and reference electrodes for each cycle. The reference cells had an initial charge capacity of 215.7 mAh $g^{-1}$and a discharge capacity of 168.3 mAh g^{-1}. For the freeze-dried electrode, the initial charge capacity was 227.5 mAh $g^{-1}$and the discharge capacity was 163.7 mAh g^{-1}, which is slightly lower than the reference electrode. The reference electrode had an irreversible loss of 47.4 mAh $g^{-1}$for the first cycle while for the freeze-dried electrode, this was 63.9 mAh g^{-1}. For the next cycle the reference electrode experienced a further drop in charge capacity to 191.4 mAh g^{-1}, and a slight increase in discharge capacity to 174.6 mAh g^{-1}. The freeze-dried electrodes also experienced a decrease in charge capacity and decrease in discharge capacity to 177.3 and 166.0 mAh g^{-1}, respectively. As the C-rate changes from C/10 to 1C there is a sharp decrease in both charge and discharge capacity in the first cycle for both the reference and freeze-dried electrode. The refer-

ence electrodes went from 191.4 to 175.9 mAh g^{-1}in charge capacity and from 174.6 to 148.0 mAh g^{-1}in discharge capacity. The freeze-dried electrodes experience a decrease from 177.3 to 159.2 mAh g^{-1}in the charge capacity and 166.0 to 130.1 mAh g^{-1}in discharge capacity in this cycle. For the rest of the cycling, both electrodes experience a steady loss of capacity. On average, the reference electrodes have an irreversible loss of 9.4 mAh g^{-1}per cycle, while the freeze-dried electrodes experienced 7.1 mAh g^{-1}lost per cycle. It can also be observed that the standard deviation for the freeze-dried electrode is much larger than for the reference electrode throughout the cycling. While all the reference electrodes performed similarly with a C-rate of 1C and had standard deviations ranging from 0.2 to 7.6 mAh g^{-1}per cycle, with a mean standard deviation of ca. 4.4 mAh g^{-1}per cycle, the freeze-dried electrodes were more inconsistent with standard deviations ranging 16.5 to 75.8 mAh g^{-1}per cycle, with a mean standard deviation of ca. 28.7 mAh g^{-1}per cycle.

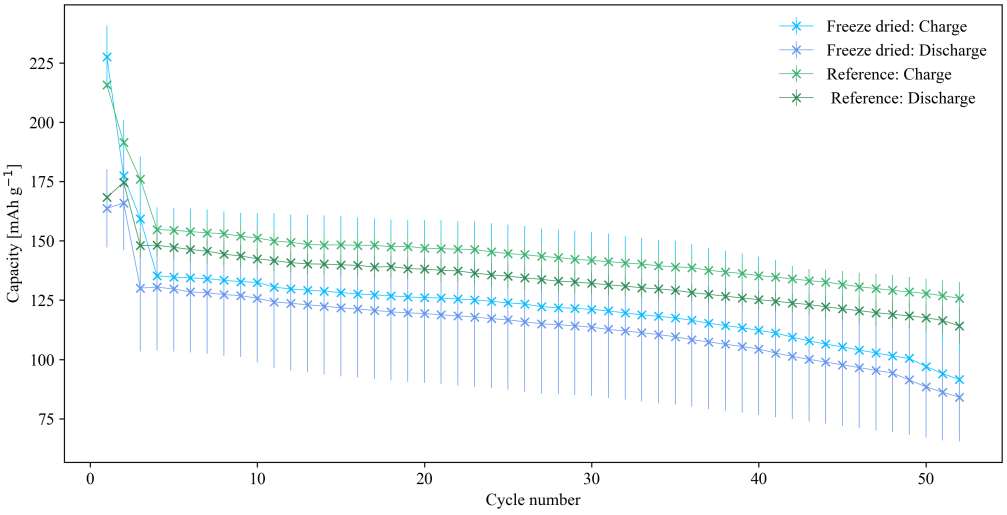

Figure 4.1: Charge and discharge capacities for freeze-dried and reference electrodes cycled at a C-rate of 1C with corresponding standard deviations.

Figure 4.2 represents the cells that were cycled at a C-rate of C/2 except for the first two cycles which, like the previous cells, were cycled at a C-rate of C/10 for the formation cycles. The freeze-dried and reference electrodes display a lower difference in performance for this cycling program than the previous one. Both have a high charge capacity for the first three cycles compared to the discharge capacity. The charge capacity was 218.4 and 206.7 mAh $g^{-1}$the discharge capacity was 171.3 and 158.7 mAh $g^{-1}$for the freeze-dried and reference electrodes,

respectively. The first cycle had a capacity loss of 47.1 mAh $g^{-1}$for the freeze-dried electrode which is slightly higher than the reference electrode which had a capacity loss of 47.9 mAh g^{-1}. The second cycle gave a large decrease in charge capacity for the freeze-dried electrodes from 218.4 to 184.2 mAh g^{-1}, while there was barely any change in the discharge capacity from 171.3 to 173.6 mAh g^{-1}. The reference electrodes also experienced a dip in charge capacity from 206.7 to 183.0 mAh g^{-1}, but had a more noticeable increase in discharge capacity than the freeze-dried from 158.7 to 166.3 mAh g^{-1}. From cycle 3 the C-rate changed to C/2. The freeze-dried and reference electrodes had a very similar performance from cycle 4 to cycle 20. The charge capacities were 157 and 157.8 mAh g^{-1}, the discharge capacities were 146.7 and 146.8 mAh g^{-1}, and the capacity losses were 10.8 and 10.8 mAh g^{-1}per cycle from cycle 4 to 20 for the freeze-dried and reference electrode, respectively. After cycle 20 the freeze-dried electrode deteriorated quickly, and after cycle 31 the charge capacity of the freeze-dried was lower than the discharge capacity of the reference electrode. The reference electrode kept the charge and discharge capacities until cycle 38 when the capacities dropped. However, the capacities remained higher than the freeze-dried ones until the end of the cycling.

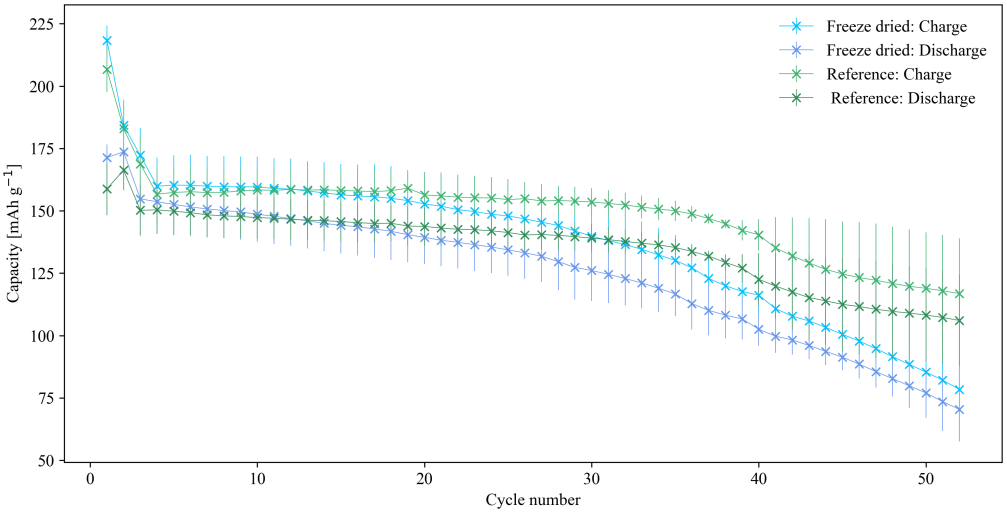

Figure 4.2: Charge and discharge capacities for freeze-dried and reference electrodes cycled at a C-rate of C/2 with corresponding standard deviations.

The variation in the three parallels of reference electrodes was a lot higher in the last ten cycles than they had been previously, having a mean standard deviation of 20.0 mAh g^{-1}during these cycles compared to the mean standard deviation of 7 mAh g^{-1}per cycle during the first 42

cycles. This was a lot higher than for the freeze-dried electrodes which had a mean standard deviation of 7.4 mAh g^{-1}per cycle in the last ten cycles, but had a higher deviation in the first 42 cycles at 10.5 mAh g^{-1}per cycle.

Figure 4.3 and 4.4 shows the Coulombic efficiency for each cycle for the freeze-dried and reference electrode that were cycled at C-rates of 1C and C/2, respectively. Here the trend for irreversible losses can be observed.

Figure 4.3 shows the Coulombic efficiency for the cells cycled at 1C after the formation cycles of C/10. The freeze-dried electrode displayed a lower initial efficiency at 71.9 % compared to the reference electrode with an initial efficiency of 78.0 %. After the first three cycles, the efficiencies of both electrodes stabilized at 95-96 %. From cycle 4 to the end of cycling the freeze-dried electrodes had a decreased efficiency from 96.5 % to 91.8 % while the reference electrodes had a decrease from 95.3 % to 90.8 %. The freeze-dried electrode had a slightly higher efficiency than the reference electrode from cycle 4 until cycle 49 when the freeze-dried electrode experienced a dip from 92.9 % to 90.9 % in efficiency while the reference electrode remained just above 92 %. However, the efficiency of the freeze-dried electrode increased to 91.2 % on the following cycle and kept increasing the remaining two cycles, while the reference electrode continued the steady decline throughout the cycling program.

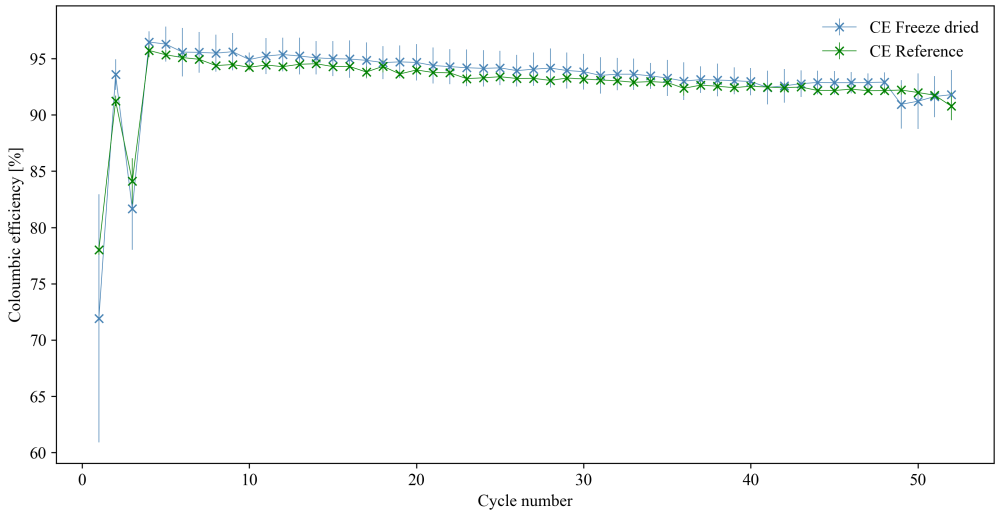

Figure 4.3: Coloumbic efficiency of freeze-dried and reference electrodes cycled at a C-rate of 1C along with standard deviations.

Figure 4.4 shows the Coloumbic efficiency of the cells cycled at C/2 after the formation cycle of C/10. These cells had a lot less stable efficiency than the cells cycled at 1C. The freeze-dried electrodes displayed a better initial efficiency than the previous ones after one cycle, with an efficiency of 78.4%. The reference ones displayed little difference from the ones cycled at 1C, with an initial efficiency of 76.8%. In general, both electrodes displayed worse efficiency than the cells cycled at 1C. The efficiency decreased by ca. 4% from cycle 4 to cycle 20 for both of the electrodes. The freeze-dried electrodes displayed slightly higher values than the reference electrode until cycle 20 where the curves shifted places. During these first cycles, there was not a large deviation in the efficiency values. There was an irregularity in the efficiency as the cycling continues after the 20th cycle. Both electrodes had a decrease in efficiency, albeit the freeze-dried electrodes decreased slightly more than the reference electrodes. At cycle 37 the curves switched again, and the freeze-dried electrodes had a greater efficiency than the reference electrodes. However, a short while later at cycle 42 both experience a sharp decrease in efficiency, before increasing again. The freeze-dried electrode increased in efficiency for the next two cycles before starting to decrease steadily again. The reference electrode increased until it crosses the freeze-dried electrode again in cycle 46 and the efficiency was kept stable at around 91% for the remaining cycles, while the freeze-dried electrodes ended the cycling at 89.8%.

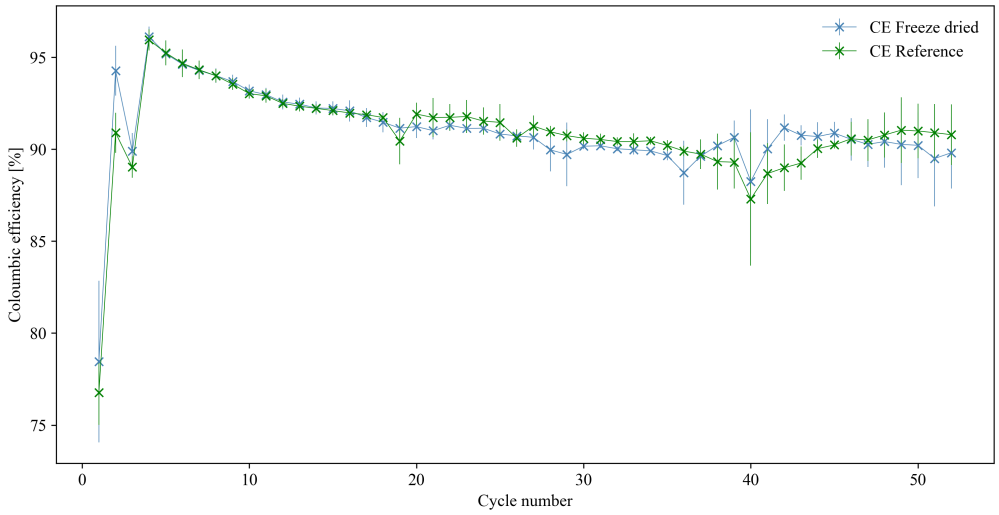

Figure 4.4: Coloumbic efficiency of freeze-dried and reference electrodes cycled at a C-rate of C/2.

4.1.2 Potential curves

This section provides the potential profiles of the electrodes obtained through galvanostatic cycling of the freeze-dried and reference electrodes. One of each parallel of electrodes is provided here and the other parallels are provided in Appendix C. Figures 4.5 and 4.6 give the potential curves of one freeze-dried and one reference electrode cycled at 1C, called Freeze-dried 1 and Reference 1 from Table 3.1 in Section 3.3.1. Both have an initial potential of over 3.5 V which decreases slightly before increasing toward the upper cut-off of 4.3 V. The freeze-dried and reference electrodes have very similar curves, using 48.1 and 47.0 hours to complete the formation cycles and complete their cycling in 136.9 and 132.2 hours, respectively.

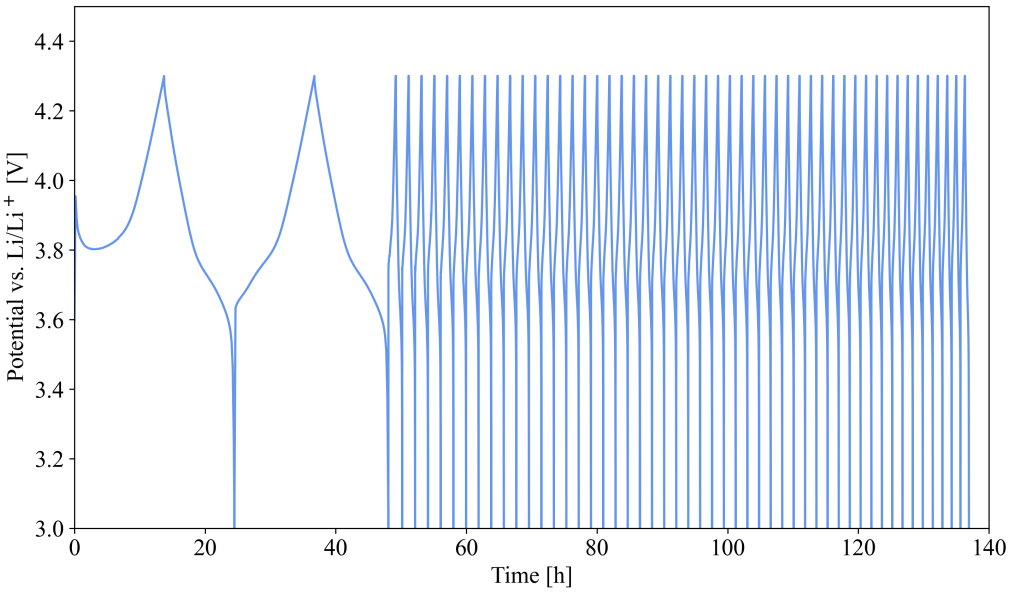

Figure 4.5: Potential curve for one of the freeze-dried electrodes cycled at a C-rate of 1C, Freeze-dried 1.

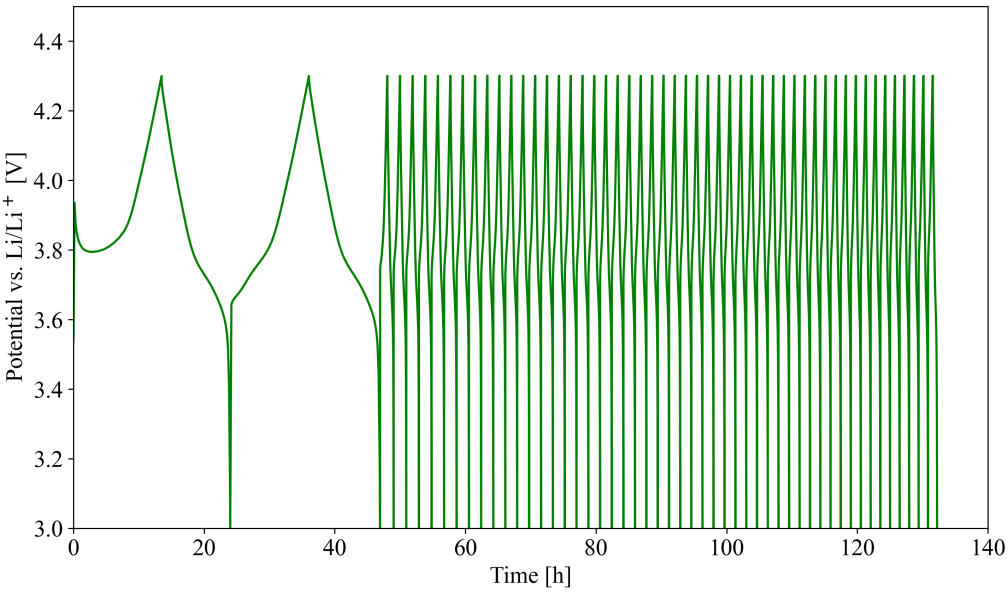

Figure 4.6: Potential curve for one of the reference electrodes cycled at a C-rate of 1C, Reference 1.

Figure 4.7 and 4.8 are the potential curves of one freeze-dried and one reference electrode cycled at a C-rate of C/2, which were Freeze-dried 6 and Reference 4 from Table 3.1 in Section 3.3.1. The freeze-dried electrode had a slightly higher initial potential at ca. 3.8 V than the reference electrode at ca. 3.7 V. The freeze-dried electrode used 47.6 hours on the formation cycles and 219.1 hours to complete the cycling program. The reference electrode used 46.7 and hours to complete the formation cycles and completed the cycling program in 220.9 hours. The potential curves of these two electrodes were similar, both being continuous and without interruptions or deviations from the program.

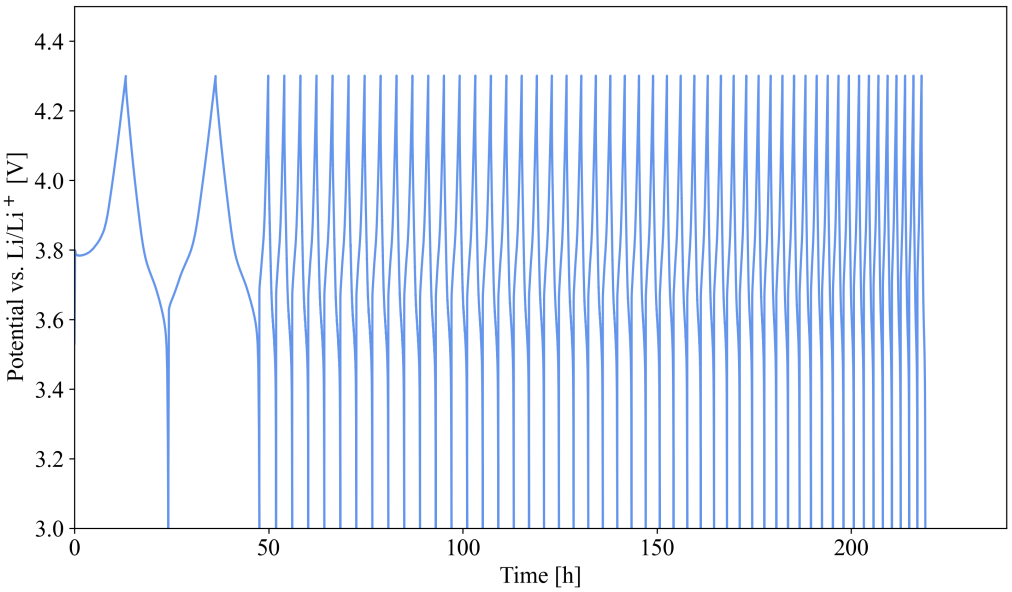

Figure 4.7: Potential curve for one of the freeze-dried electrodes cycled at a C-rate of C/2, Freeze-dried 6.

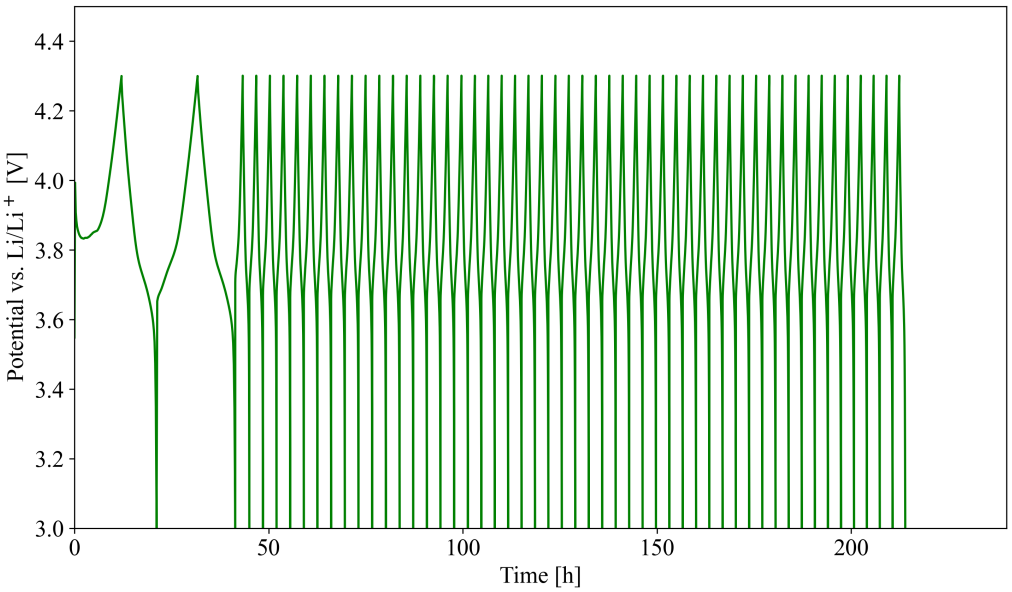

Figure 4.8: Potential curve for one of the reference electrodes cycled at a C-rate of C/2, Reference 6.

4.1.3 Voltage profiles

Figure 4.9 and 4.10 give the voltage profile of the first cycle for all parallels cycled at 1C and C/2, respectively. In both figures, the freeze-dried electrodes show both better and worse

charge and discharge capacities in the first cycle. For the cells cycled at 1C, this is a significant difference for one of the parallels, while at a rate of C/2 the discharge curve is closer to the reference curve. The freeze-dried electrode also showed a higher charge capacity during the first cycle in both cases. The parallels for the reference electrodes are very similar and their curves overlap in both figures.

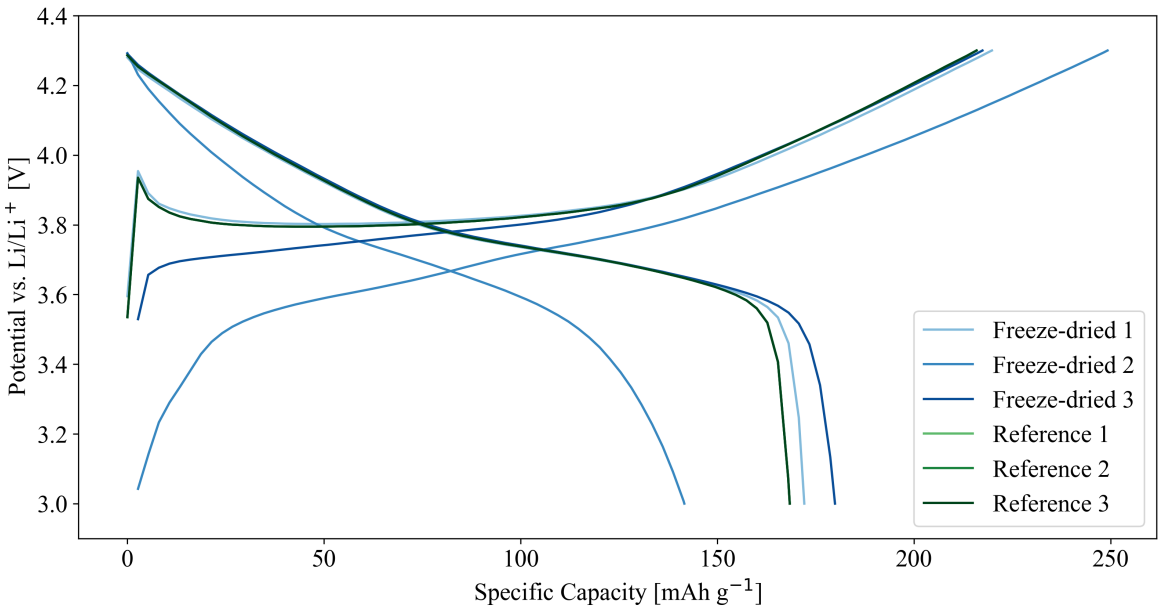

Figure 4.9: Potential vs. capacity of the electrodes cycled at 1C during the first cycle.

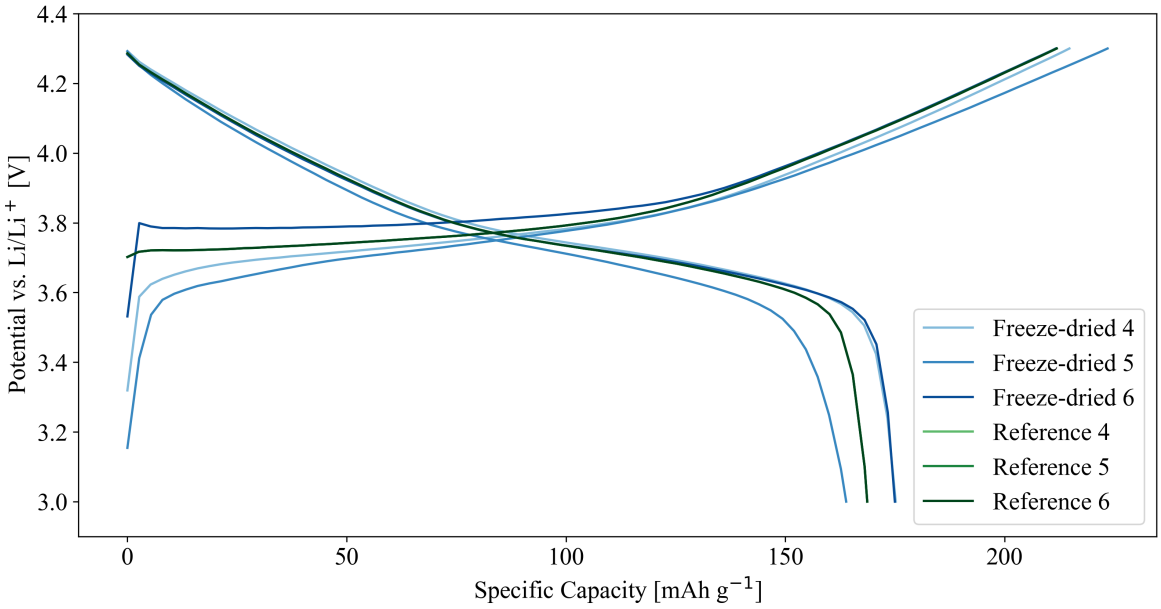

Figure 4.10: Potential vs. capacity of the electrodes cycled at C/2 during the first cycle.

The voltage profiles of the half-cells cycled are presented here and in Appendix C. The voltage profile of one freeze-dried and one reference electrode cycled at 1C are seen in Figure 4.11 and 4.12, called Freeze-dried 1 and Reference 1. These profiles are very similar when looking at the initial and final capacities. Reference 1 deteriorates at a more constant pace, while Freeze-dried 1 deteriorates more between cycles 1 and 10, and cycles 40 and 50, than between cycles 10 and 40.

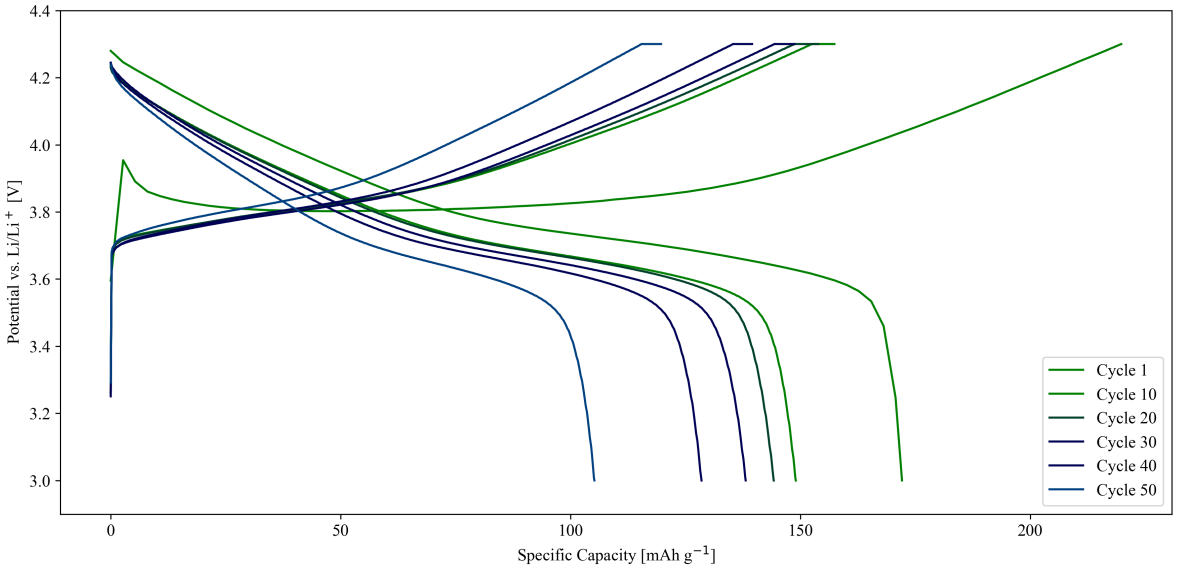

Figure 4.11: Potential vs. capacity during cycle 1, 10, 20, 30, 40, and 50 for one of the freeze-dried electrodes in a half cell cycled at a C-rate of 1C, Freeze-dried 1

.

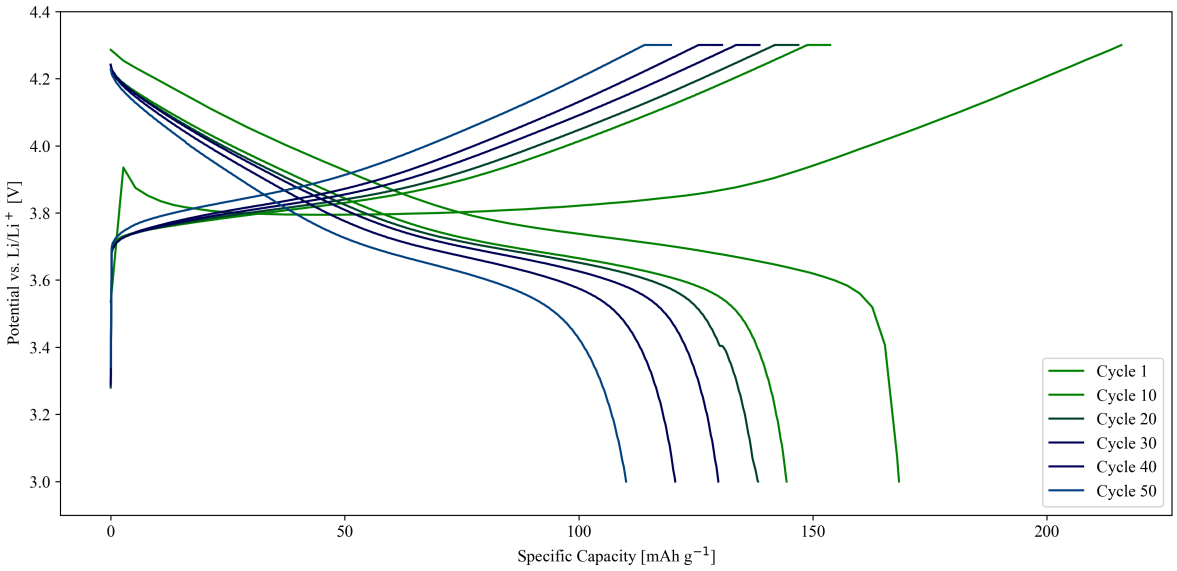

Figure 4.12: Potential vs. capacity during cycle 1, 10, 20, 30, 40, and 50 for one of the reference electrodes in a half cell cycled at a C-rate of 1C, Reference 1.

Figure 4.13 and 4.14 show the potential profiles of one freeze-dried and one reference electrode cycled at C/2, called Freeze-dried 6 and Reference 6 respectively.

Minimal capacity fade can be observed in Reference 6. In 52 cycles the electrode had its irreversible discharge capacity reduced by only 21.2 mAh g^{-1}. The largest capacity fade occurs in the charge capacity between cycles 1 and 10, where 8.5 mAh $g^{-1}$is lost. Freeze-dried 6 has a large capacity loss during the cycling. In 52 cycles the discharge capacity decreased by 97.5 mAh g^{-1}, where the last 20 cycles experience more than half of this decrease.

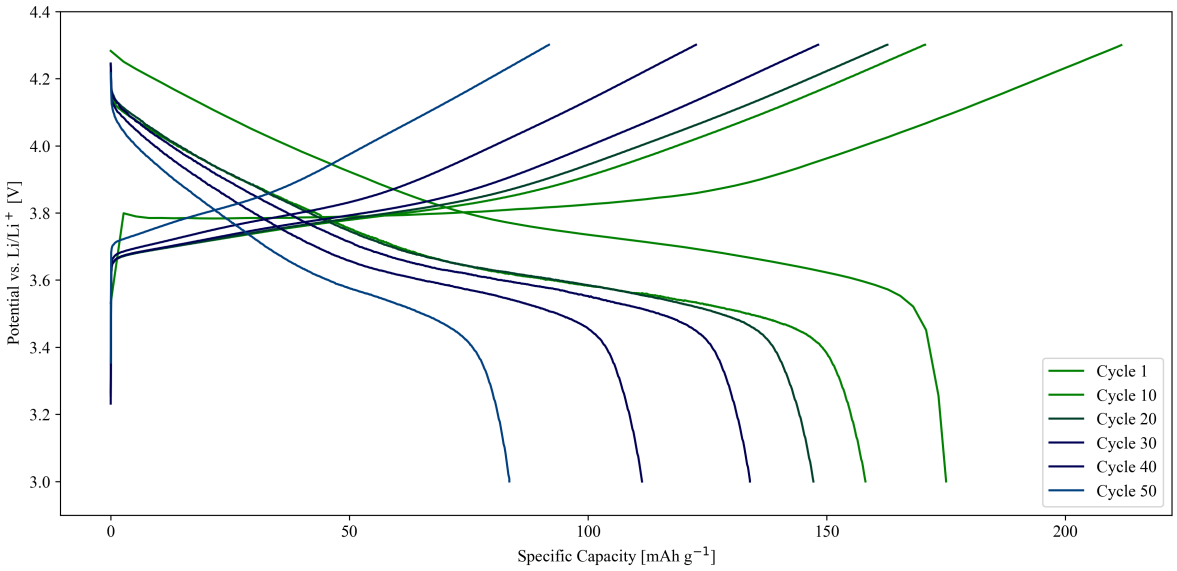

Figure 4.13: Potential vs. capacity during cycle 1, 10, 20, 30, 40, and 50 for one of the freeze-dried electrodes in a half cell cycled at a C-rate of C/2, Freeze-dried 6.

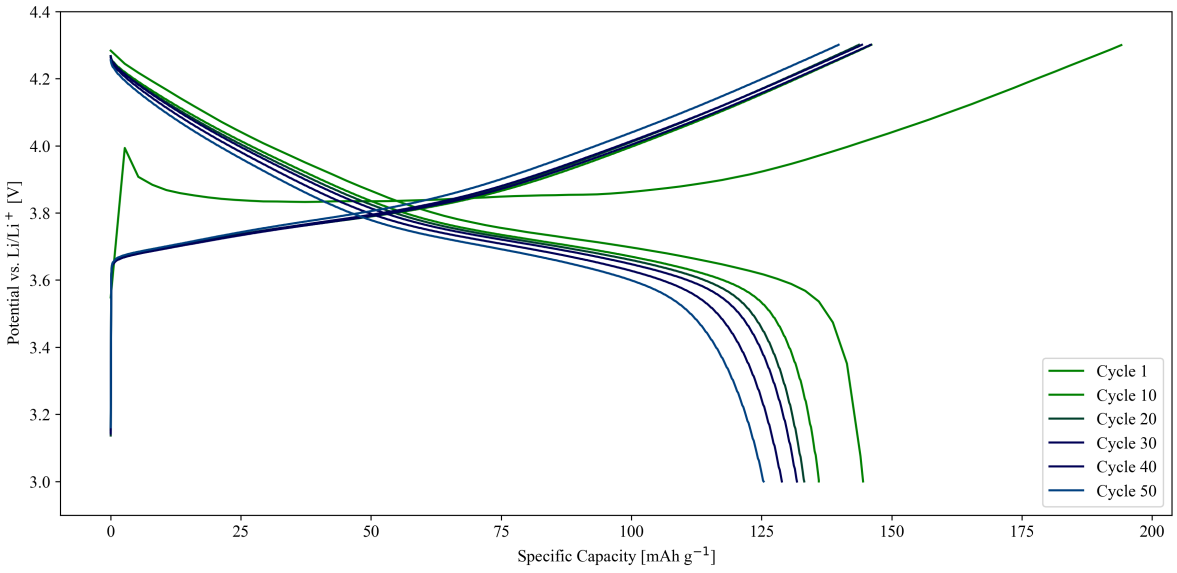

Figure 4.14: Potential vs. capacity during cycle 1, 10, 20, 30, 40, and 50 for one of the reference electrodes in a half cell cycled at a C-rate of C/2, Reference 6.

The remaining potential profiles are given in Appendix C.

4.2 EIS measurements

The results from the EIS measurements and tortuosity determinations are presented in the following section. PEIS measurements were conducted on the symmetrical cells manufactured according to Section 3.3.2, with the properties presented in Table 3.2. The measurements were fitted to the equivalent circuit presented in Figure 2.9 using ZView and are displayed as Nyquist plots in Figure 4.15. The values for the different parameters collected from the fitting are presented in Appendix C in Table C.1.

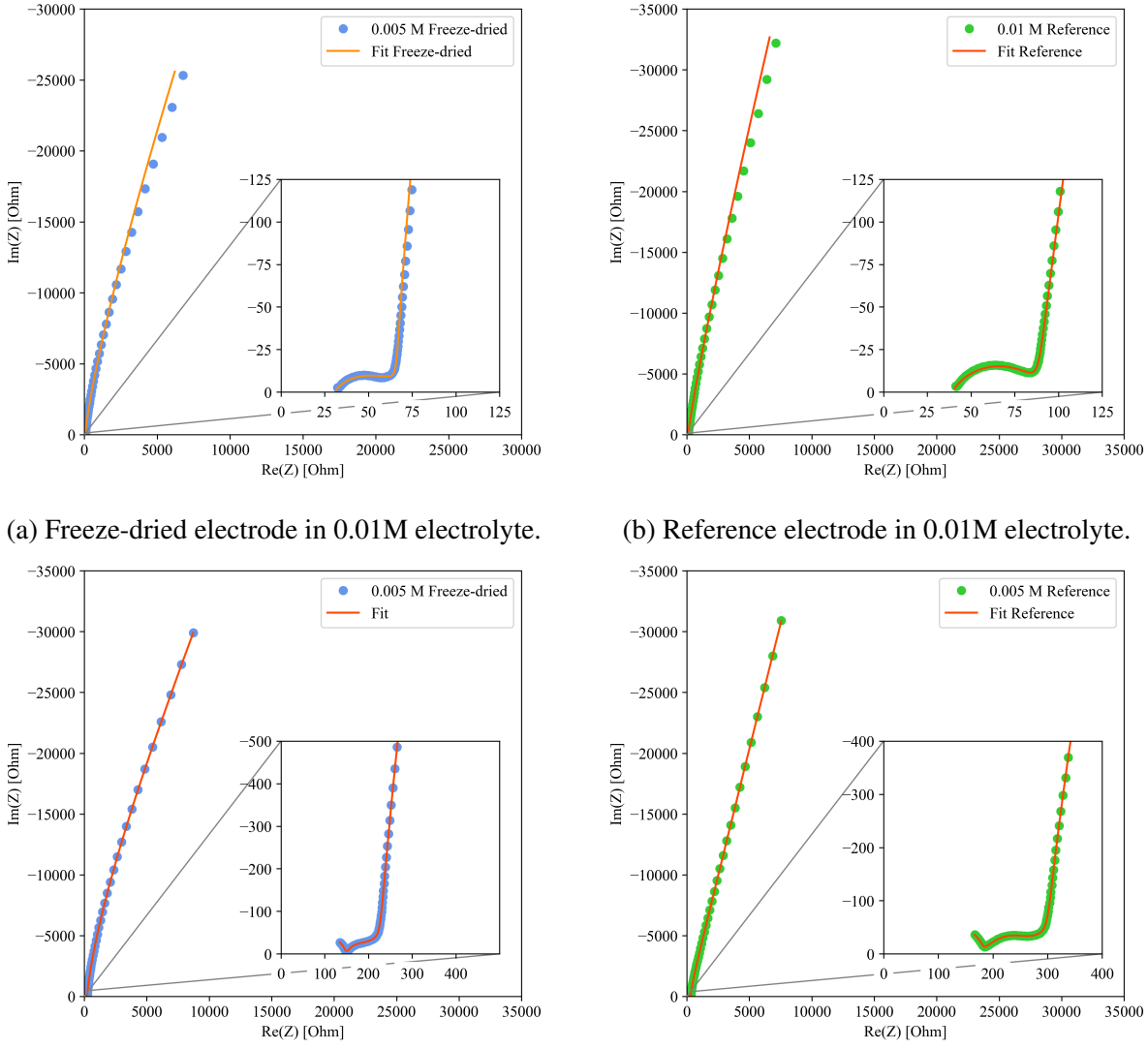

(a) Freeze-dried electrode in 0.01M electrolyte.

(b) Reference electrode in 0.01M electrolyte.

(c) Freeze-dried electrode in 0.005M electrolyte.

(d) Reference electrode in 0.005M electrolyte.

Figure 4.15

4.3 FTIR analysis

This section provides the FTIR results for freeze-dried and vacuum-dried 5% PVDF solution on Al-foil as well as the pure PVDF powder. The pure PVDF powder had a vacuum atmosphere as a background measurement while the other two had pristine Al-foil as a background measurement. These backgrounds were retracted from the sample spectra and are given in Appendix D. The spectra are given as transmittance spectra.

Figure 4.16-4.18 show the FTIR spectra of the three samples between 4000 and 550 cm^{-1}, with emphasis on different intervals of the spectra. Figure 4.16 shows the full FTIR spectrum of the three samples between 4000 and 550 cm^{-1}. Here all the signals can be seen as vertical lines within the diagram.

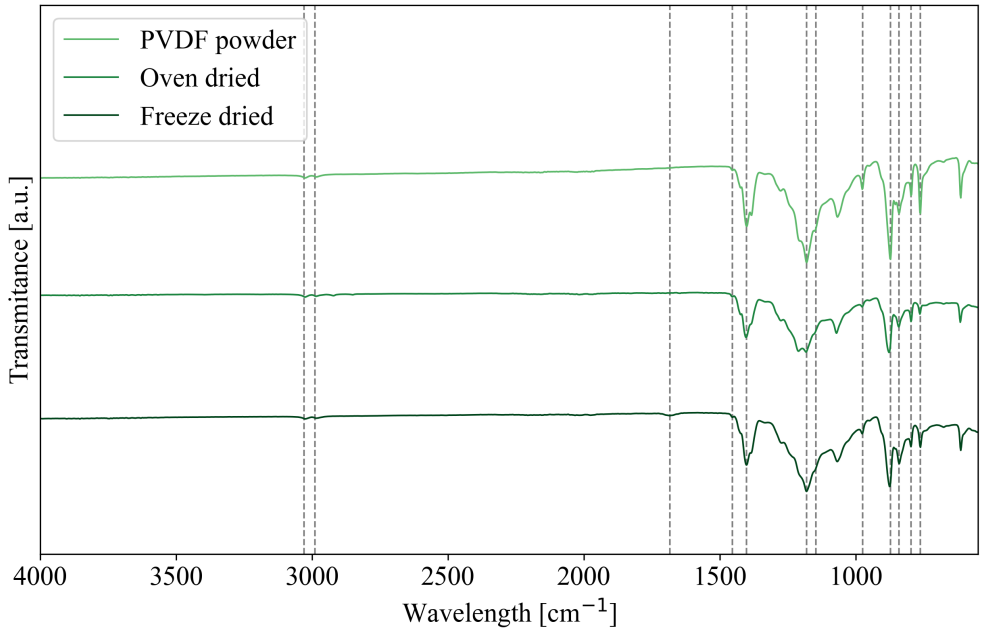

Figure 4.16: FTIR spectrum of 5% PVDF solution on Al-foil freeze-dried and vacuum-dried, and PVDF powder between 4000-550 cm^{-1}.

Figure 4.17 shows the spectra of the three samples between 1500 and 550 cm^{-1}. The most prominent peaks in this range were at 1453, 1402, 1210, 1180, 1066, 975, 872, 841, 796, 762, and 613 cm^{-1}, which are observed in all the samples.

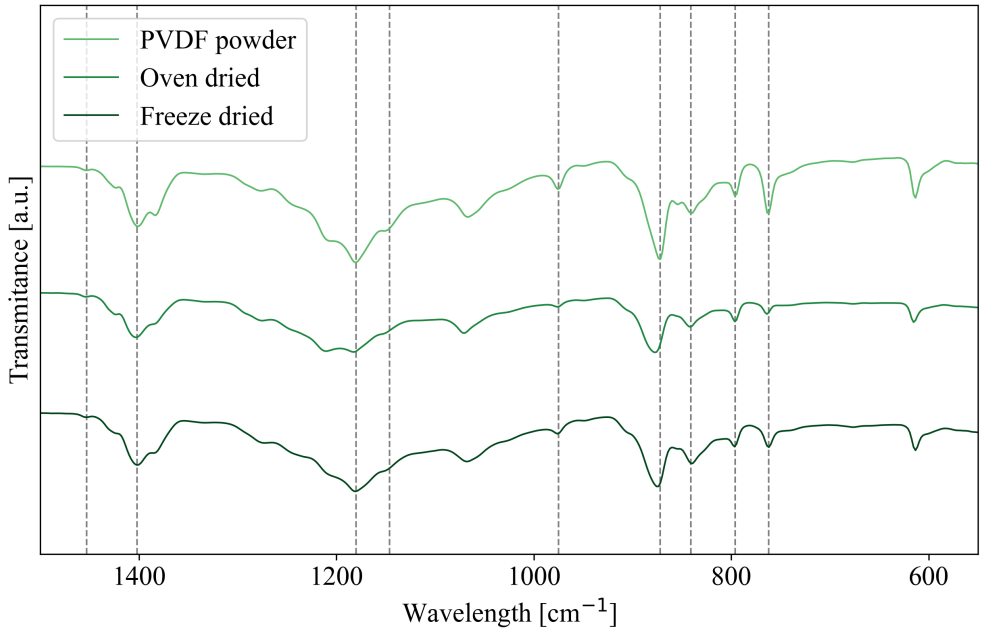

Figure 4.17: FTIR spectrum of 5% PVDF solution on Al-foil freeze-dried and vacuum-dried, and PVDF powder between 1500-550 cm^{-1}.

Figure 4.18 shows the measurements of the three samples between 4000 and 1500 cm^{-1} (4.18a) and enlarged at 1800-1500 cm^{-1} (4.18b). For the PVDF powder and oven-dried sample, there are two peaks at 3030 and 2990 cm^{-1}, which can be observed in Figure 4.18a. The freeze-dried sample has the peaks at 3030 and 2990 cm^{-1}, and an additional one at 1670 cm^{-1}, which is enlarged in Figure 4.18b.

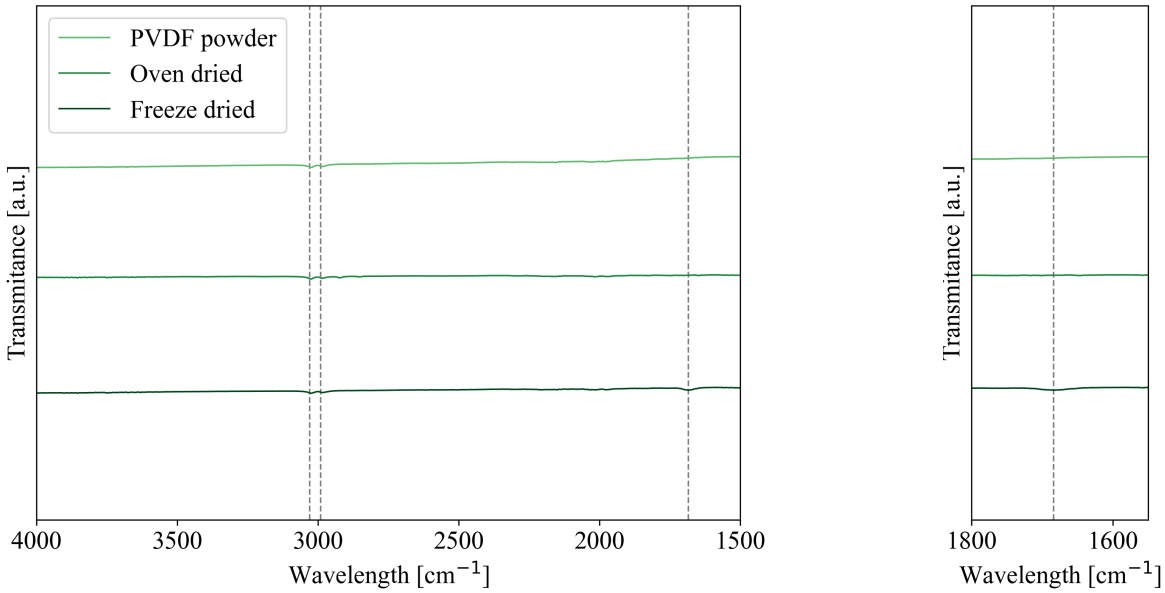

(a) (b)

Figure 4.18: FTIR spectrum of 5% PVDF solution on Al-foil freeze-dried and vacuum-dried, and PVDF powder between a) 4000-15000 cm^{-1} and b) 1800-1600 cm^{-1}.

Comparing the peaks from the FTIR spectra in this section to the peaks presented in Table 2.2 in Section 2.8.3, an estimate of potential bonds present in the samples was made.

All the samples showed peaks at 2900 and 3030 cm^{-1}, this could be due to the CH_3 bond present in PVDF, which has a range of 3000-2800 cm^{-1}. The next peak which is observed in all samples is at 1453 cm^{-1}, which corresponds to a CH_2 bond. This bond will also have a peak at ca. 870 cm^{-1}, and the closest peak in the spectra is at 872 cm^{-1}. However, this could also be due to the CH bonds in PVDF which will give peaks at 1400 cm^{-1} and 1000-700 cm^{-1}. The spectra display peaks at 1402, 762, 796, 841, 872, and 975 cm^{-1} which are within this range of the CH bond. While the peak at 841 cm^{-1} is within the range of the CH bond, it could also be due to the CF_2 bond in PVDF with a peak at ca. 830 cm^{-1}. The peak at ca. 1140 cm^{-1} in the spectrum could also be due to CF_2, which has a peak at ca. 1146 cm^{-1}.

The freeze-dried sample has a small additional peak at 1684 cm^{-1}, this could be due to the CN bond in NMP, which is the closest in range of the potential bonds present with a range of 1660-1615 cm^{-1}.

4.4 Morphology of electrodes identified through SEM

In this section, SEM imaging of the electrodes is presented. The images of different parts of the electrodes, both on the surface and cross-section are displayed. The electrodes depicted were analyzed after the drying process was completed. Different parts within the middle section of the electrodes were investigated, and images that represented the identified morphology were chosen.

4.4.1 Surface morphology

Figures 4.19 displays images that were taken of the surface of the electrodes of both the freeze-dried electrodes and the reference electrodes, and shows the general morphology of the electrode surfaces at 100 μm (4.19a and 4.19b) and 50 μm (4.19c and 4.19d). The NMC particles can be distinguished at this magnification, but the carbon black and binder can only be seen as clusters surrounding the NMC particles. The distribution of particles appears similar in the two electrodes.

In Figure 4.20 individual NMC particles are pictured at a greater magnification. There appear to be dark areas along the grain boundaries of the NMC particles in the freeze-dried sample, which do not appear in the reference sample. Additionally, there appears to be more carbon black on the surface of the NMC particle on the freeze-dried electrode compared to the reference electrode.

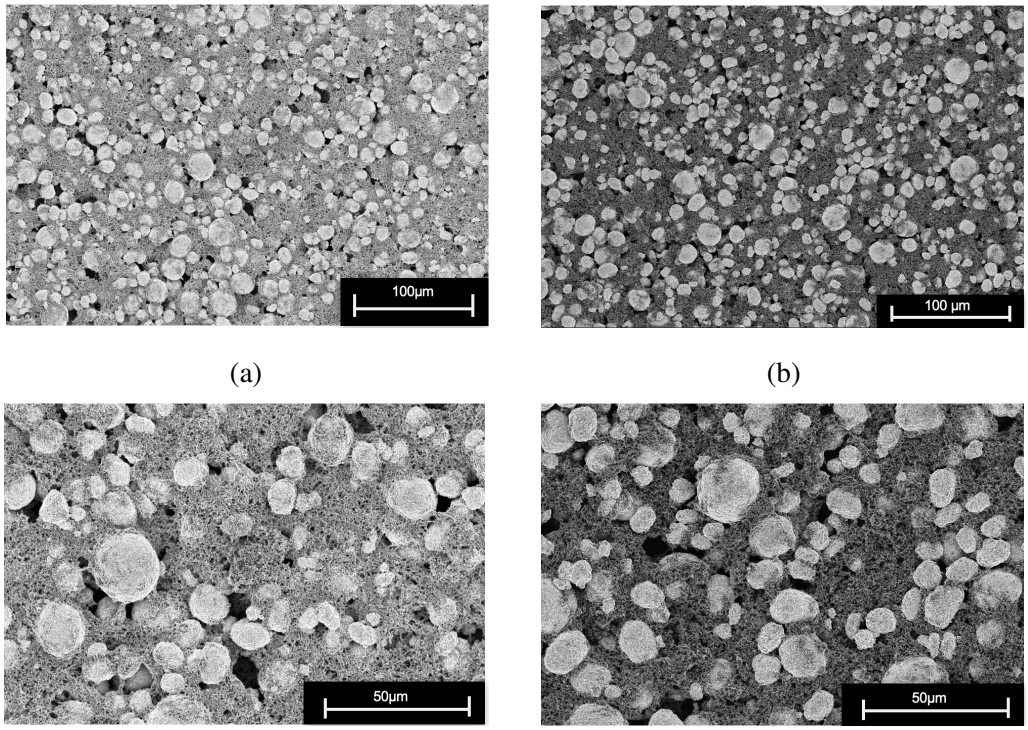

(a) (b)

(c) (d)

Figure 4.19: The surface of the freeze-dried electrode (a and c) and reference electrode (b and d)

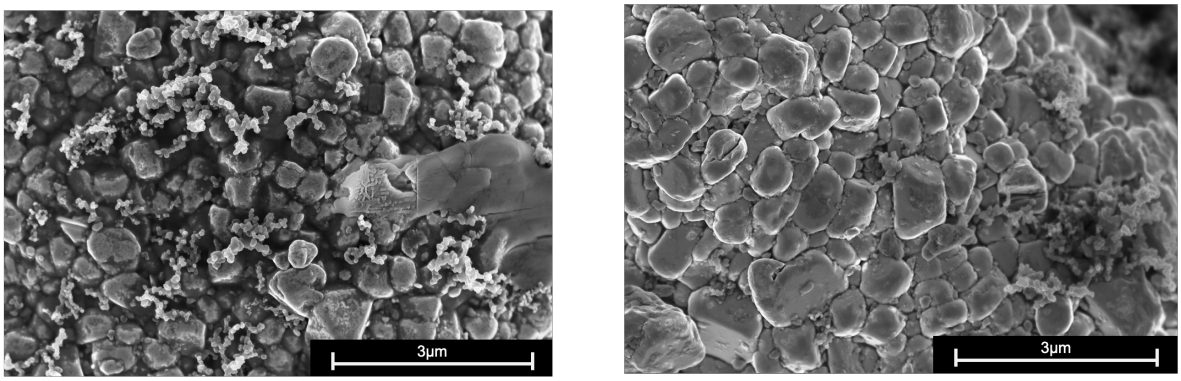

(a) (b)

Figure 4.20: The surface of NMC particles on the surface of a) freeze-dried electrodes and b) reference electrodes

Figure 4.21 shows the carbon black clusters observed on the surface of the freeze-dried electrodes (4.21a and 4.21c) and reference electrodes (4.21b and 4.21d). The carbon black covers the PVDF binder entirely within these clusters and the pure binder cannot be observed in these

images. There is little observable difference in the distribution of carbon black. There is a contrast within the clusters where the edges closer toward the ion beam probe are lighter in color than the carbon black deeper within the material. The images of the reference electrode show a lighter color than the freeze-dried electrode.

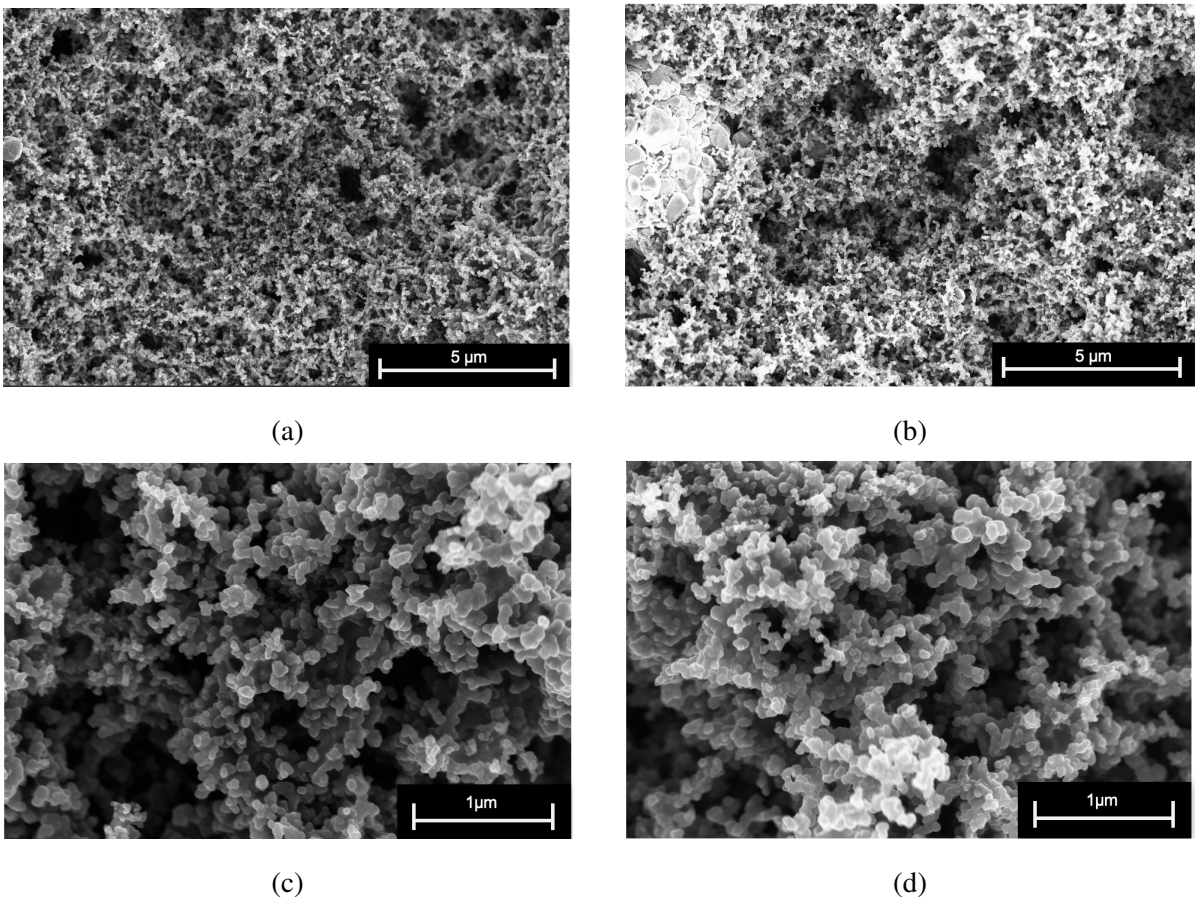

(a) (b)

(c) (d)

Figure 4.21: The surface of carbon black on the surface of a) freeze-dried electrodes and b) reference electrodes

Figure 4.22 shows a close-up of the PVDF binder identified in the two electrodes. Figure 4.22a-4.22c shows the binder in the freeze-dried electrode while Figure 4.22d shows a binder string coated in carbon black. In Figure 4.22a the binder can clearly be observed on the NMC cathodes in a way that was not observed in the reference electrode. Looking closer at the binder in Figures 4.22b and 4.22c the binder seems to be somewhat covered in carbon black near the thicker base, however, the strands connecting the NMC particles together are uncoated in the middle. The strands also appear to be stretched thinly across the gap. In Figure 4.22c there are also signs of breakage present on the right side of the binder string. In Figure 4.22d the binder strand is completely coated in carbon black particles. The binder holds its shape even though it is only

connected to a carbon black cluster at one end. It has no signs of breakage which were observed in the freeze-dried electrode. There string shape of the binder were found several places in the freeze-dried electrode, but was not observed in the reference electrode at all.

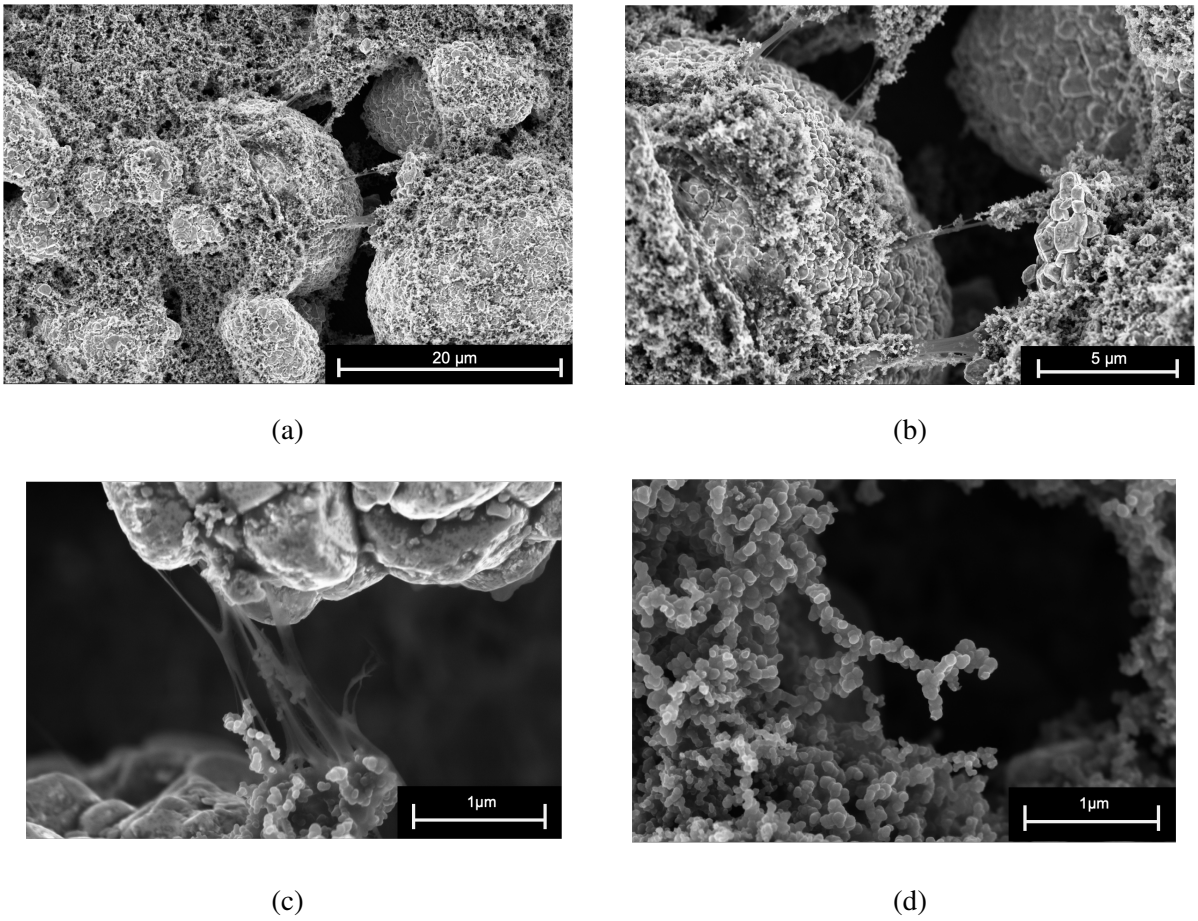

(a) (b)

(c) (d)

Figure 4.22: Images of the binder found in a)-c)the freeze-dried electrode and d) the reference electrode.

4.4.2 Cross-section morphology

As the binder distribution of the surface of the electrodes was investigated, so was the distribution of the cross-section analyzed under SEM. The SEM images of the cross-sections made with the PFIB are presented here. The electrodes were not very thick at less than 30 μm on average. As seen in Figure 4.23 the larger NMC particles spanned the entire cross-sections of the electrodes. The distribution of particles is not observably different between the electrodes in 4.23a and 4.23b. There are still clusters of carbon black and binder in between the NMC particles, however, no pattern can be observed.

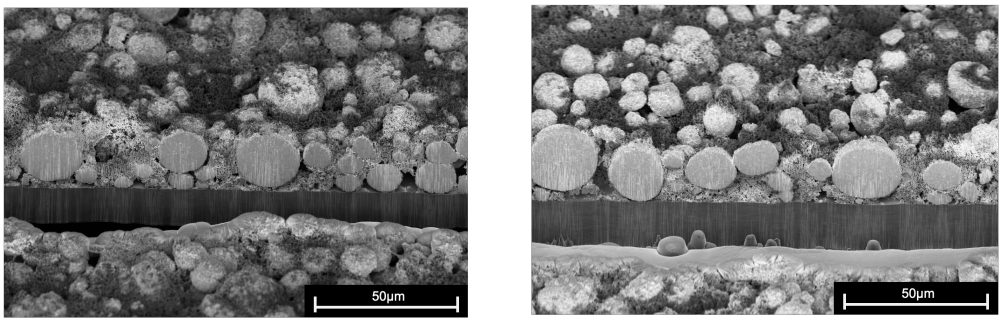

(a) (b)

Figure 4.23: Cross-section of a) the freeze-dried electrode and b) the reference electrode

A closer look at the cross-sections in Figure 4.24, reveals that the carbon black clusters in the freeze-dried electrode has higher contrast in signal than the reference electrode. While the reference electrode shows some high contrast fields within the carbon black clusters, this is a smaller area than what is observed in the freeze-dried electrode.

The particles near the aluminum current collector also have a dark residue on the bottom. This was the aluminum foil that was sputtered by the PFIB during the cutting and was deposited onto the underside of the particle. This residue layer is thicker where the gap between the particles and the foil was larger.

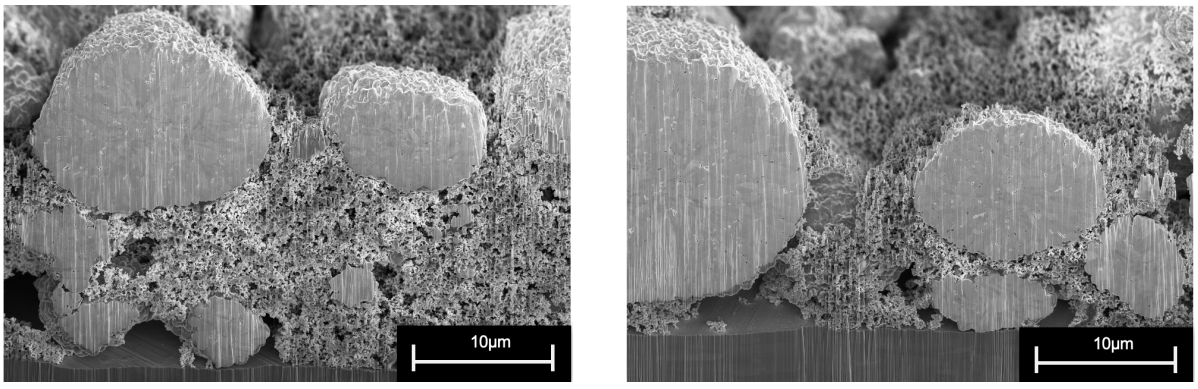

(a) (b)

Figure 4.24: Cross-section of a) the freeze-dried electrode and b) the reference electrode

When taking SEM images of the electrode cross-sections, some imperfections within the NMC particles were observed as seen in Figures 4.25 and 4.26. Figure 4.25 shows many small pores within the NMC particles that are not along grain the boundaries but within the grains them-

selves. Figure 4.26 shows separated phases within the particle that should not be there.

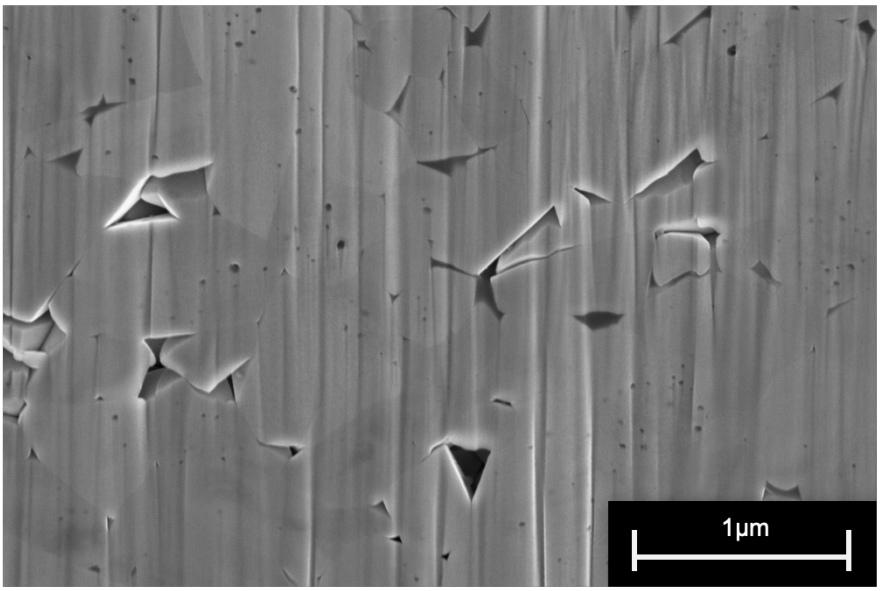

Figure 4.25: Pores within the NMC particle

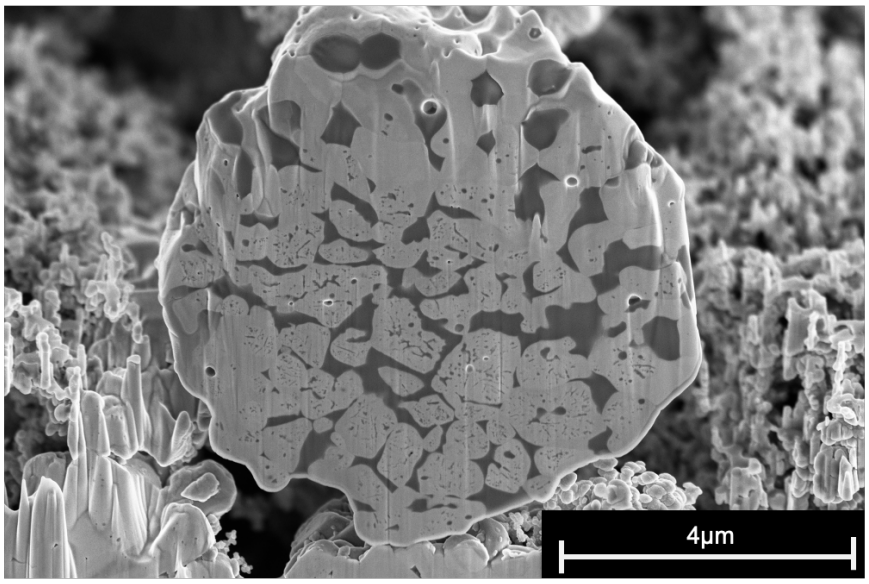

Figure 4.26: Seperated phases in an NMC particle

5 Discussion

5.1 Galvanostatic cycling

The galvanostatic cycling with potential limits was used to determine whether the drying method had any impact on the electrochemical performance of the electrodes. Freeze-drying, or freeze-casting, has previously shown favorable results in terms of capacity retention, porosity, pore distribution, and rate performance[16;58;17].

5.2 Cycling with a C-rate of 1C

5.2.1 Capacities

Figure 4.1 shows that both the electrodes had a high charge capacity compared to the discharge capacity during the first cycle, which is due to side reactions taking place. However, the difference from charge to discharge is much larger for the freeze-dried electrode, making it more energy intensive to charge than the reference electrode. The freeze-dried electrodes show a generally poorer performance with higher irregularity in measurements than the reference electrodes. This is punctuated in Figure 4.9 where the parallels of the reference electrodes follow the same curves in the first cycle, overlapping so much that the three curves are barely differentiable. For the freeze-dried electrodes, the curves do not overlap, and the difference in performance is considerable. One of the freeze-dried cells performed significatly worse than the other two with an initial charge capacity of 246.5 and a discharge capacity of 146.6. This half-cell was also the main cause of the large standard deviations in the measurements of the freeze-dried electrodes.

Looking at the potential profiles in Figures 4.11 and 4.12 which show the continued cycling of Freeze-dried 1 and reference 1 in Figure 4.9, the reference electrode displays a more predictable pattern in capacity loss than the freeze-dried electrode. The freeze-dried electrode suffered substantial capacity loss towards the 50th cycle. However, the graphs of the well-performing half-cells are not too different in how they act during cycling except for capacity retention. The reason for this could be lower contact within the freeze-dried electrode.

5.2.2 Efficiencies

In Figure 4.3 the efficiency of the freeze-dried electrode is higher than the reference electrode for most of the cycling. The most notable difference is in the first cycle where the efficiency of the freeze-dried electrode is at 72% while the reference is at 78%. It appears that once the electrode has stabilized during the first few cycles, the capacity loss diminishes, and the effect of the battery increases. This is expected from freeze-drying as the pores of freeze-dried materials are generally better aligned[16]. The efficiencies are still disappointing for both electrodes.

5.2.3 Potential Curves

The potential curves in Figure 4.5-4.6 show that the cells had continuous cycling and there is little difference between the freeze-dried and the reference electrodes in terms of behavior. Both the cells represented had initial potentials of over 3.8 V and had no problem reaching the potential limits set. The two electrodes used approximately the same amount of time in the formation cycles, but the freeze-dried electrode took longer to complete the remaining cycles, finishing 4.7 hours after the reference electrode. As the cycling progresses the time each cycle takes decreases in both electrodes due to the reduction in capacity, while the current remains the same. Following this, the potential limit is reached faster. One of the reasons for the freeze-dried electrode taking longer could be decreased contact between the particles.

5.3 Cycling with a C-rate of C/2

Half-cells were cycled at C/2 to see if the freeze-dried electrodes would be able to perform better at a lower C-rate which usually gives better results in terms of capacity retention and efficiency. Ideally, a battery performs well at a high C-rated to allow for faster charging[]. However, for easier comparison a lower C-rate was chosen.

5.3.1 Capacities

The cycling performed at C/2 also had side reactions during the first cycles which pressed up the charge capacities as was observed in Figure 4.2. However, the freeze-dried electrodes are performing better at C/2 than at 1C, and are able to compete with the reference electrodes in both charge and discharge capacity during the first 20 cycles, which seemed promising. Figure 4.10 shows this as well, where two of the freeze-dried electrodes had a discharge capacity above

the reference electrodes, and one was below the reference. Again, all the reference electrodes perform so consistently during the first cycle that they are indistinguishable in the graph, which accounts for the small uncertainty in the measurements. The freeze-dried electrodes deteriorated severely during the rest of the cycling program and the final discharge capacity of 70.37 $\pm$ 12.85 mAh g^{-1}compared to the reference electrodes' final discharge capacity of 106.03 $\pm$ 18.32 mAh $g^{-1}$was disappointing.

This deterioration is also observable in the potential profile of the freeze-dried electrode in Figure 4.13 which is the potential profile of Freeze-dried 6 in 4.10. The deterioration in the potential profile of Reference 6 in Figure 4.14 is a lot lower than for the freeze-dried electrode, and also lower than Reference 1 cycled at 1C, which is as expected. There is barely any difference in charge capacity after cycle 1 and the final discharge capacity is very high.

5.3.2 Efficiencies

The efficiencies of the C/2 cycling in Figure 4.4, appears more irregular than that of 1C cycling. This is true for both the freeze-dried and reference electrodes, and when considering the average efficiency per cycle, this is at 90.91-90.96%. This is a lot lower than the expected, especially for the reference electrode.

5.3.3 Potential Curves

Similar to the potential curves of the 1C cycling, the two electrodes cycled at C/2 in Figure C.11 and 4.14 both show continuous curves. Both electrodes finish cycling at similar time intervals, 219.1 hours for the freeze-dried electrode and 220.9 hours for the reference electrode, indicating that at a lower C-rate the freeze-dried electrode's behavior is closer to the reference.

5.4 Contact within the electrodes

The large difference in charge and discharge capacities, and the lack of capacity retention experienced in the freeze-dried cathodes are most likely due to insufficient contact within the electrode. As observed in Figure 4.22a-4.22c the freeze-dried electrode had strings of binder which are uncoated by carbon black. PVDF is an insulating material that does not transport electrons, which is why a conductive material such as carbon black is added to the slurry mixture. The binder also appears to be stretched thinly and prone to breaking, which occurred in

Figure 4.22c after being exposed to the electron gun probe in the SEM. A theory is that the lowered temperature in the freeze-dryer chamber did not allow the binder time to orient itself as it will do in vacuum drying as PVDF has limited elasticity properties[81]. Previous research on the freeze-drying of electrodes has all been conducted on CMC binders.

In the clusters of carbon black which can be observed in Figure 4.21, this bare binder of the Freeze-dried electrodes is not observed in the same way as it is next to NMC particles. However, in both electrodes charging occurs. Charging can be an indication of a bad connection between the particles.

In Figure 4.24 there are also signs of charging in the carbon black clusters of the cross-sections.

5.4.1 Impurities in the NMC particles

While investigating the cross-sections of the electrodes, observations of impurities within the NMC particles were made. In Figure 4.25 pores are observable within the NMC grains. While the gaps along the grain boundaries are expected, the pores within the grains are not and indicate an insufficient synthesis route.

In addition to the pores within the grains, Figure 4.26 also displays different phases within the NMC particle. While SEM is not used to differentiate what elements are in a sample, it can differentiate between heavier and lighter atoms[73]. Looking back at Figure 4.24, while the NMC grains observed within the particle don't appear to be completely homogeneous, they do not separate the same way as the NMC particle in Figure 4.26. As the NMC particle has darker spots, a theory is that during the synthesis of this particle, the elements separated creating different areas with different phases. While this type of impurity was only observable in one of the six cross-sections investigated, the fact that it was found at all is worth mentioning.

Both these impurities occurred during the synthesis of the NMC particles, which were provided by Targay, and could have had an influence on the lowered performance of the half-cells.

5.5 Mobility within electrodes

Figure 4.15 shows the fitted values to the EIS experimental data in using the Randles circuit in Figure 2.9. As can be observed, the fitted values are well aligned with the data points measured.

The 0.01M electrolyte was too concentrated, and the results from the fitting gave highly inac-

curate results, as seen in the error in Table C.1. Therefore these results will not be discussed.

In the same table the Z_W freeze-dried electrode with 0.005M electrolyte is a lot higher than that of the reference electrode with 0.005M electrolyte. From Table 3.2 it is observed that the densities, thickness and porosity of the freeze-dried and reference electrodes are very similar, and as the electrolytes used in the measurements are the same, the tortuosity calculated from Equation 2.8 is the resistance measure multiplied by a constant. This means that the tortuosity of the electrodes is largely dependent on the resistance within the electrode and the difference in resistance between the electrodes can be used to estimate how the tortuosity differs. However, as the calculations for the resistance are quite complex, this is not easily done. Therefore this Z_W value is used to determine which electrode has the higher tortuosity.

This is very different from other freeze-dried electrodes, which all reported lowered tortuosity and higher porosity[58;17;16]. It is not probable that the lack of contact within the elctrode is the reason for this, but rather the lack of effect from the freeze-drying as will be discussed further in Section 5.6

5.6 Effect of freeze-drying

5.6.1 Residual solvent in the electrodes

The FTIR spectra of the electrodes and PVDF-powder are similar as observed in Figure 4.16. Most of the peaks appear to overlap each other, and at first glance there appears to be no other component than PVDF in either of the samples. Looking at the main part of the spectra between 1500 and 550 cm^{-1} in Figure 4.17, the largest difference is in the reference spectra at 1146 cm^{-1}, where the peak is more subdued than in the other two and at 872 cm^{-1}, where the peak is slightly displaced. This is likely not due to any other bond present.

In Figure 4.18a) there is a slight peak at 1684 cm^{-1} which can be observed closer in b). This peak is most likely from a CN bond that is present in NMP. In the NMP spectrum, this bond is one of the bonds with the clearest signal i.e. highest peak, which is probably the only reason this can be observed. It is likely that the traces of NMP in the sample are overshadowed by the amount of PVDF, so it is difficult to make any other observations of the solvent.

This amount of solvent, although small compared to the mass of other components present in the electrode, is probably a factor in the poor cell performance of the freeze-dried electrodes. While

FTIR is not a quantitative characterization method, the presence indicated by these spectra is concerning and brings up the question of how much effect the freeze-drying had on the electrodes at all.

As NMP has a very low freezing point, -24 °C, the freeze-dryer used, which only reaches -60 °C at the freezing plate, did probably not reach low enough temperatures to sufficiently freeze the NMP to reach the complete sublimation stage in four hours. It is due to this low freezing point that Liu et. al. used a 10% 1,4-dioxane in water solvent for their production of $LiFePO_4$ cathodes[17]. It is well known that NMC cathodes produced with water solvent creates alkaline solutions, which affect the battery[82]. There is also little knowledge about the sublimation pressure and temperature of NMP, which determines what temperature NMP needs to have to sublimate. Should this temperature be below -60 °C, then it is impossible that the electrodes were sufficient dried in the freeze-dryer used. Although, even if the sublimation temperature was above -60 °C, it is unlikely that the electrodes reached this temperature as its is only the freezing plate that reaches -60 °C, and the actual temperature in the chamber was not measured. It is likely that this temperature was higher. Dang et. al. used a temperature of -150 °C on a freezing plate for 10 minuttes before freeze-drying at -50 °C overnight with great results[58].

As observed in Figure 4.23 the electrodes are thin. Some of the NMC particles span the entire cross-section while the areas with binder and carbon black fill the spaces. With such an uneven surface height, it is difficult to say whether the porosity measured is due to the drying method as the particle distribution is uneven. From Figure 4.24 the height difference from the top of the NMC particle to the top of the binder and carbon black next to it appears to be ca. 10 μm for both the freeze-dried and reference electrode, making it hard to see how the different drying methods affect the particle distribution. From other experiments on freeze-drying of electrodes, the electrodes were minimum 10-20 μm however the particle shape is different from the NMC particles[14].

6 Conclusion

Freeze-drying of NMC_{622} cathode has been evaluated. The aim was to assess whether freeze-drying could replace the current drying processes in cathode production. The evaluations consisted of electrochemical testing, morphology characterization, and FTIR spectroscopy of freeze-dried electrodes and reference electrodes dried in a vacuum oven.

The galvanostatic measurements performed on the cathodes showed lower specific capacity for the freeze-dried electrodes than the reference electrodes dried in a vacuum oven. There was also a larger variation in the performance of the freeze-dried electrodes compared to the reference electrodes. After evaluating the electrodes in SEM, the cause of the poor performance in the freeze-dried electrodes was attributed to the reduced contact between the particles due to the PVDF binder being insufficiently coated in the conductive material carbon black. The binder was also more stretched out and prone to break under the electron gun probe of the SEM. FTIR evaluations indicated that another possible reason for the decreased performance was that the freeze-drying did not remove the solvent as well as vacuum oven drying, leaving residue NMP in the freeze-dried electrode.

Both electrodes had virtually the same thickness and porosity. Electrochemical impedance spectroscopy of the electrodes revealed that the freeze-dried electrode had a higher resistance and lower tortuosity than the reference electrode.

Lastly, some impurities within the NMC particles were found in SEM imaging. As the same NMC powder was used in both the freeze-dried and reference electrode, which would explain the overall reduced performance of both electrodes.

7 Further Work

Freeze-drying in general is a good technique for creating high-porosity materials with water as the solvent. As there are not many uses for NMP solvent in its solid form, knowledge of how the physical properties of solid NMP differ from ice is limited. Should NMP has a large decrease in density from its liquid form to its solid form, there is a possibility that the porosity of the material will decrease or worse, that the porous structure collapses before it solidifies. Other solvents should also be evaluated for freeze-drying and whether they can replace NMP in NMC cathode production.

The temperature of the freeze-dryer should also be evaluated to find which temperature would produce the best-performing electrodes. Here, freeze-casting should also be considered as solvents such as NMP evaporates quickly from the surface of materials and there is a question of the effect of freeze-drying through vacuum only to produce the right structure. Freeze-casting could possibly increase the freezing rate through contact with the cooling plate, limiting the premature evaporation of NMP.

To examine the particle distribution across the cross-section, thicker electrodes should be produced and examined to determine whether binder migration is as prominent in freeze-drying as it is in conventional electrode drying. The binder should also be tested under different freezing conditions to evaluate whether the freeze-drying process damages the binder and at which temperature the binder obtains the best quality. Different binders should be tested under these conditions to evaluate which produces the best results.

Should freeze-drying prove an adequate replacement for the current standard, there is also a need for assessing the energy use and operation cost of freeze-drying at an industrial scale. Freeze-drying is an energy-intensive and slow process as it requires low temperatures over a longer period of time. It is also performed in a closed vacuum which requires vacuum pumps to operate properly. As current drying processes happen on a continuously moving conveyor belt, making it low maintenance, freeze-drying should ideally be as low maintenance which would require it to work in a more open system. The freeze-drying system should be evaluated, to see if there is any way to streamline the process. NMP collection during freeze-drying ought to be assessed, as NMP vapor is explosive even at low concentrations.

References

[1] Ghassan Zubi, Rodolfo Dufo-López, Monica Carvalho, and Guzay Pasaoglu. The lithium-ion battery: State of the art and future perspectives. *Renewable and Sustainable Energy Reviews*, 89:292–308, 6 2018. ISSN 18790690. doi: 10.1016/j.rser.2018.03.002.

[2] M Bielewski, A. Pfrang, S. Bobba, A. Kronberga, A. Georgakaki, S. Letout, A. Kuokkanen, A. Mountraki, E. Ince, D. Shtjefni, G. Joanny, O. Eulaerts, and M. Grabowska. Clean Energy Technology Observatory:Batteries for energy storage in the European Union - 2022 Status Report on Technology Development, Trends, Value Chains and Markets. Technical report, Publication Office of the European Union, Luxembourg, 2022. URL `https://joint-research-centre.ec.europa.eu`.

[3] European Commission Secretariat-General. The European Green Deal. Technical report, European Commission, Brussels, 12 2019. URL `https://eur-lex.europa.eu/legal-content/EN/TXT/?uri=COM:2019:640:FIN`.

[4] Fred Lambert. Tesla (TSLA) becomes best-selling brand in Norway as the country hits new electric vehicle records, 1 2022. URL `https://electrek.co/2022/01/03/tesla-tsla-becomes-best-selling-brand-in-norway-new-electric-vehicle-records/`.

[5] Govind Bhutada. Breaking Down the Cost of an EV Battery Cell, 2 2022. URL `https://www.visualcapitalist.com/breaking-down-the-cost-of-an-ev-battery-cell/`.

[6] Silje Nornes Bryntesen, Anders Hammer Strømman, Ignat Tolstorebrov, Paul R. Shearing, Jacob J. Lamb, and Odne Stokke Burheim. Opportunities for the state-of-the-art production of lib electrodes—a review. *Energies*, 14(5), 3 2021. ISSN 19961073. doi: 10.3390/en14051406.

[7] Chris Yuan, Yelin Deng, Tonghui Li, and Fan Yang. Manufacturing energy analysis of lithium ion battery pack for electric vehicles. *CIRP Annals - Manufacturing Technology*, 66(1):53–56, 2017. ISSN 17260604. doi: 10.1016/j.cirp.2017.04.109.

[8] David L. Wood, Jeffrey D. Quass, Jianlin Li, Shabbir Ahmed, David Ventola, and Claus Daniel. Technical and economic analysis of solvent-based lithium-ion electrode drying

with water and NMP. *Drying Technology*, 36(2):234–244, 1 2018. ISSN 15322300. doi: 10.1080/07373937.2017.1319855.

[9] Yangtao Liu, Ruihan Zhang, Jun Wang, and Yan Wang. Current and future lithium-ion battery manufacturing. *iScience*, 24(102332):1–17, 4 2021. doi: 10.1016/j.isci.

[10] Stefan Jaiser, Jana Kumberg, Jop Klaver, Janos L. Urai, Wilhelm Schabel, Joyce Schmatz, and Philip Scharfer. Microstructure formation of lithium-ion battery electrodes during drying – An ex-situ study using cryogenic broad ion beam slope-cutting and scanning electron microscopy (Cryo-BIB-SEM). *Journal of Power Sources*, 345:97–107, 2017. ISSN 03787753. doi: 10.1016/j.jpowsour.2017.01.117.

[11] Georg-Wilhelm Oetjen. *Freeze-Drying*. Wiley-VCH, 1999.

[12] M K Krokida, V T Karathanos, and Z B Maroulis. Effect of Freeze-drying Conditions on Shrinkage and Porosity of Dehydrated Agricultural Products. *Journal of Food Engineering*, 35:369–380, 1998.

[13] Benjamin Delattre, Ruhul Amin, Jonathan Sander, Joël De Coninck, Antoni P. Tomsia, and Yet-Ming Chiang. Impact of Pore Tortuosity on Electrode Kinetics in Lithium Battery Electrodes: Study in Directionally Freeze-Cast LiNi 0.8 Co 0.15 Al 0.05 O 2 (NCA) . *Journal of The Electrochemical Society*, 165(2):A388–A395, 2018. ISSN 0013-4651. doi: 10.1149/2.1321802jes.

[14] Yoon Hwa, Eongyu Yi, Hao Shen, Younghoon Sung, Jiawei Kou, Kai Chen, Dilworth Y. Parkinson, Marca M. Doeff, and Elton J. Cairns. Three-Dimensionally Aligned Sulfur Electrodes by Directional Freeze Tape Casting. *Nano Letters*, 19(7):4731–4737, 7 2019. ISSN 15306992. doi: 10.1021/acs.nanolett.9b01805.

[15] Shuping Li, Ruoyu Xiong, Zhilong Han, Renjie He, Siwu Li, Huamin Zhou, Chuang Yu, Shijie Cheng, and Jia Xie. Unveiling low-tortuous effect on electrochemical performance toward ultrathick LiFePO4 electrode with 100 mg/cm2 area loading. *Journal of Power Sources*, 515, 12 2021. ISSN 03787753. doi: 10.1016/j.jpowsour.2021.230588.

[16] Milad Azami Ghadkolai, Stephen Creager, Jagjit Nanda, and Rajendra K. Bordia. Freeze Tape Cast Thick Mo Doped Li 4 Ti 5 O 12 Electrodes for Lithium-Ion Batteries . *Journal of The Electrochemical Society*, 164(12):A2603–A2610, 2017. ISSN 0013-4651. doi: 10.1149/2.1311712jes.

[17] Changyong Liu, Xingxing Cheng, Bohan Li, Zhangwei Chen, Shengli Mi, and Changshi Lao. Fabrication and characterization of 3D-printed highly-porous 3D LiFePO4 electrodes by low temperature direct writing process. *Materials*, 10(8), 8 2017. ISSN 19961944. doi: 10.3390/ma10080934.

[18] Christian Julien, Alain Mauger, Ashok Vijh, and Karim Zaghib. *Lithium Batteries Science and Technology*. Springer International Publishing, 2016.

[19] Yuping Wu, Xiangyun Yuan, Shiyong Zhao, and Teunis Van Ree. *Lithium-Ion Batteries*. CRC Press, 4 2015. ISBN 9780429096884. doi: 10.1201/b18427.

[20] John B. Goodenough and Kyu Sung Park. The Li-ion rechargeable battery: A perspective. *Journal of the American Chemical Society*, 135(4):1167–1176, 1 2013. ISSN 00027863. doi: 10.1021/ja3091438.

[21] Ronald Dell and D A J Rand. *Understanding Batteries*. RSC Paperbacks. Royal Society of Chemistry, Cambridge, 2001. ISBN 9780854046058. URL `https://search.ebscohost.com/login.aspx?direct=true&db=nlebk&AN=496119&site=ehost-live&scope=site`.

[22] Wu Xu, Jiulin Wang, Fei Ding, Xilin Chen, Eduard Nasybulin, Yaohui Zhang, and Ji Guang Zhang. Lithium metal anodes for rechargeable batteries. *Energy and Environmental Science*, 7(2):513–537, 2014. ISSN 17545706. doi: 10.1039/c3ee40795k.

[23] Michal Osiak, Hugh Geaney, Eileen Armstrong, and Colm O'Dwyer. Structuring materials for lithium-ion batteries: Advancements in nanomaterial structure, composition, and defined assembly on cell performance. *Journal of Materials Chemistry A*, 2(25):9433–9460, 7 2014. ISSN 20507496. doi: 10.1039/c4ta00534a.

[24] John B. Goodenough. How we made the Li-ion rechargeable battery: Progress in portable and ubiquitous electronics would not be possible without rechargeable batteries. John B. Goodenough recounts the history of the lithium-ion rechargeable battery. *Nature Electronics*, 1(3):204, 3 2018. ISSN 25201131. doi: 10.1038/s41928-018-0048-6.

[25] P. U. Nzereogu, A. D. Omah, F. I. Ezema, E. I. Iwuoha, and A. C. Nwanya. Anode materials for lithium-ion batteries: A review. *Applied Surface Science Advances*, 9, 6 2022. ISSN 26665239. doi: 10.1016/j.apsadv.2022.100233.

[26] Uday Kasavajjula, Chunsheng Wang, and A. John Appleby. Nano- and bulk-silicon-based insertion anodes for lithium-ion secondary cells. *Journal of Power Sources*, 163(2):1003–1039, 1 2007. ISSN 03787753. doi: 10.1016/j.jpowsour.2006.09.084.

[27] Jeannine R. Szczech and Song Jin. Nanostructured silicon for high capacity lithium battery anodes. *Energy and Environmental Science*, 4(1):56–72, 1 2011. ISSN 17545692. doi: 10.1039/c0ee00281j.

[28] M. Stanley Whittingham. Lithium batteries and cathode materials. *Chemical Reviews*, 104(10):4271–4301, 10 2004. ISSN 00092665. doi: 10.1021/cr020731c.

[29] Patrick Rozier and Jean Marie Tarascon. Review—Li-Rich Layered Oxide Cathodes for Next-Generation Li-Ion Batteries: Chances and Challenges. *Journal of The Electrochemical Society*, 162(14):A2490–A2499, 2015. ISSN 0013-4651. doi: 10.1149/2.0111514jes.

[30] Luca Schneider, Julian Klemens, Eike Christian Herbst, Marcus Müller, Philip Scharfer, Wilhelm Schabel, Werner Bauer, and Helmut Ehrenberg. Transport Properties in Electrodes for Lithium-Ion Batteries: Comparison of Compact versus Porous NCM Particles. *Journal of The Electrochemical Society*, 169(10):100553, 10 2022. ISSN 0013-4651. doi: 10.1149/1945-7111/ac9c37. URL `https://iopscience.iop.org/article/10.1149/1945-7111/ac9c37`.

[31] Hong Sun and Kejie Zhao. Electronic Structure and Comparative Properties of LiNi x Mn y Co z O 2 Cathode Materials . *The Journal of Physical Chemistry C*, 121(11):6002–6010, 3 2017. ISSN 1932-7447. doi: 10.1021/acs.jpcc.7b00810.

[32] Zhaolin Liu, Aishui Yu, and Jim Y Lee. Synthesis and characterization of LiNi1xyCoxMnyO2 as the cathode materials of secondary lithium batteries. *Journal of Power Sources*, 81:1999–416, 1999. URL `www.elsevier.comrlocaterjpowsour`.

[33] K.-S. Lee, S.-T. Myung, K. Amine, H. Yashiro, and Y.-K. Sun. Structural and Electrochemical Properties of Layered Li[Ni[1-2x]Co[x]Mn[x]]O[2] (x=0.1–0.3) Positive Electrode Materials for Li-Ion Batteries. *Journal of The Electrochemical Society*, 154(10):A971, 2007. ISSN 00134651. doi: 10.1149/1.2769831.

[34] Myung Hyoon Kim, Ho Suk Shin, Dongwook Shin, and Yang Kook Sun. Synthesis and electrochemical properties of Li[Ni0.8Co0.1Mn0.1]O2 and Li[Ni0.8Co0.2]O2 via co-

precipitation. *Journal of Power Sources*, 159(2):1328–1333, 9 2006. ISSN 03787753. doi: 10.1016/j.jpowsour.2005.11.083.

[35] Wen Liu, Pilgun Oh, Xien Liu, Min Joon Lee, Woongrae Cho, Sujong Chae, Youngsik Kim, and Jaephil Cho. Nickel-Rich Layered Lithium Transition-Metal Oxide for High-Energy Lithium-Ion Batteries. *Angewandte Chemie - International Edition*, 54(15):4440–4457, 4 2015. ISSN 15213773. doi: 10.1002/anie.201409262.

[36] Roland Jung, Philipp Strobl, Filippo Maglia, Christoph Stinner, and Hubert A. Gasteiger. Temperature Dependence of Oxygen Release from LiNi0.6Mn0.2Co0.2O2 (NMC622) Cathode Materials for Li-Ion Batteries. *Journal of The Electrochemical Society*, 165(11): A2869–A2879, 2018. ISSN 0013-4651. doi: 10.1149/2.1261811jes.

[37] Seong Min Bak, Enyuan Hu, Yongning Zhou, Xiqian Yu, Sanjaya D. Senanayake, Sung Jin Cho, Kwang Bum Kim, Kyung Yoon Chung, Xiao Qing Yang, and Kyung Wan Nam. Structural changes and thermal stability of charged LiNixMnyCozO2 cathode materials studied by combined in situ time-resolved XRD and mass spectroscopy. *ACS Applied Materials and Interfaces*, 6(24):22594–22601, 12 2014. ISSN 19448252. doi: 10.1021/am506712c.

[38] Carl D. Reynolds, Peter R. Slater, Sam D. Hare, Mark J.H. Simmons, and Emma Kendrick. A review of metrology in lithium-ion electrode coating processes. *Materials and Design*, 209, 11 2021. ISSN 18734197. doi: 10.1016/j.matdes.2021.109971.

[39] Mojdeh Nikpour, Baichuan Liu, Paul Minson, Zachary Hillman, Brian A. Mazzeo, and Dean R. Wheeler. Li-ion Electrode Microstructure Evolution during Drying and Calendering. *Batteries*, 8(9), 9 2022. ISSN 23130105. doi: 10.3390/batteries8090107.

[40] Max Wolfram von Horstig, Alexander Schoo, Thomas Loellhoeffel, Julian K. Mayer, and Arno Kwade. A Perspective on Innovative Drying Methods for Energy-Efficient Solvent-Based Production of Lithium-Ion Battery Electrodes. *Energy Technology*, 12 2022. ISSN 21944296. doi: 10.1002/ente.202200689.

[41] Andreas Altvater, Thilo Heckmann, Jochen Christoph Eser, Sandro Spiegel, Philip Scharfer, and Wilhelm Schabel. (Near-) Infrared Drying of Lithium-Ion Battery Electrodes: Influence of Energy Input on Process Speed and Electrode Adhesion. *Energy Technology*, 2022. ISSN 21944296. doi: 10.1002/ente.202200785.

[42] Sung Yeon Kim and Sehun Rhee. A Study on Improving Drying Performance of Spinel Type LiMn2O4 as a Cathode Material for Lithium Ion Battery. *Int. J. Electrochem. Sci*, 6: 5462–5469, 2011. URL `www.electrochemsci.org`.

[43] Xianfeng Wu, Xujia Li, and Xinzhi Bei. Experiments on hot-air and infrared drying characteristics of LiCoO2 cathode coating for lithium-ion battery. *Materials Science Forum*, 1003 MSF:260–267, 2020. ISSN 16629752. doi: 10.4028/www.scientific.net/MSF.1003.260.

[44] Sanghyuk Lim, Kyung Hyun Ahn, and Masato Yamamura. Latex migration in battery slurries during drying. *Langmuir*, 29(26):8233–8244, 7 2013. ISSN 07437463. doi: 10.1021/la4013685.

[45] Hideki Hagiwara, Wieslaw J. Suszynski, and Lorraine F. Francis. A Raman spectroscopic method to find binder distribution in electrodes during drying. *Journal of Coatings Technology and Research*, 11(1):11–17, 2014. ISSN 15470091. doi: 10.1007/s11998-013-9509-z.

[46] Stefan Jaiser, Marcus Müller, Michael Baunach, Werner Bauer, Philip Scharfer, and Wilhelm Schabel. Investigation of film solidification and binder migration during drying of Li-Ion battery anodes. *Journal of Power Sources*, 318:210–219, 6 2016. ISSN 03787753. doi: 10.1016/j.jpowsour.2016.04.018.

[47] Fabienne Huttner, Wolfgang Haselrieder, and Arno Kwade. The Influence of Different Post-Drying Procedures on Remaining Water Content and Physical and Electrochemical Properties of Lithium-Ion Batteries. *Energy Technology*, 8(2), 2 2020. ISSN 21944296. doi: 10.1002/ente.201900245.

[48] Yanhai Du, Nader Hedayat, Dhruba Panthi, Hoda Ilkhani, Benjamin J. Emley, and Theo Woodson. Freeze-casting for the fabrication of solid oxide fuel cells: A review. *Materialia*, 1:198–210, 9 2018. ISSN 25891529. doi: 10.1016/j.mtla.2018.07.005.

[49] Wei Wang, Chen Mo, and Chen Guohua. Issues in Freeze Drying of Aqueous Solutions *. *Chinese Journal of Chemical Engineering*, 20(3):551559, 2012.

[50] Sha Mi, Zhiqiang Liu, Chun Luo, Lingling Cai, Zezong Zhang, and Longquan Li. A review on preparing new energy ultrafine powder materials by freeze-drying. *Drying*

Technology, 38(12):1544–1564, 8 2020. ISSN 15322300. doi: 10.1080/07373937.2019.1651733.

[51] Farial Jafar and Mohammed Farid. Analysis of heat and mass transfer in freeze drying. *Drying Technology*, 21(2):249–263, 2003. ISSN 07373937. doi: 10.1081/DRT-120017746.

[52] Lue Lue Huang, Min Zhang, Arun S. Mujumdar, Dong Feng Sun, Guan Wei Tan, and Shameel Tang. Studies on decreasing energy consumption for a freeze-drying process of apple slices. *Drying Technology*, 27(9):938–946, 9 2009. ISSN 07373937. doi: 10.1080/07373930902901844.

[53] M. K. Krokida and Z. B. Maroulis. Effect of drying method on shrinkage and porosity. *Drying Technology*, 15(10):2441–2458, 1997. ISSN 07373937. doi: 10.1080/07373939708917369.

[54] J. Orlenius, O. Lyckfeldt, K. A. Kasvayee, and P. Johander. Water based processing of LiFePO 4/C cathode material for Li-ion batteries utilizing freeze granulation. *Journal of Power Sources*, 213:119–127, 9 2012. ISSN 03787753. doi: 10.1016/j.jpowsour.2012.04.037.

[55] Hao Li, Yongqi Dai, Xuetian Li, and Zhongcai Shao. Preparation of LiNi0.5Co0.2Mn0.3O2 by freeze-drying method. *Colloids and Surfaces A: Physicochemical and Engineering Aspects*, 629, 11 2021. ISSN 18734359. doi: 10.1016/j.colsurfa.2021.127486.

[56] Zheng Song, Xinfu Cao, Can Cui, Yang Zhang, Jie Liu, and Fengsheng Li. Improved preparation efficiency and electrochemical performance of LiNi0.8Co0.15Al0.05O2 cathode material by oxalic acid and freeze-drying. *Ionics*, 27(11):4663–4672, 11 2021. ISSN 18620760. doi: 10.1007/s11581-021-04228-1.

[57] Wassim Abdelwahed, Ghania Degobert, Serge Stainmesse, and Hatem Fessi. Freeze-drying of nanoparticles: Formulation, process and storage considerations, 12 2006. ISSN 0169409X.

[58] Dingying Dang, Yikai Wang, Shuang Gao, and Yang Tse Cheng. Freeze-dried low-tortuous graphite electrodes with enhanced capacity utilization and rate capability. *Carbon*, 159:133–139, 4 2020. ISSN 00086223. doi: 10.1016/j.carbon.2019.12.036.

[59] National Center for Biotechnology Information. PubChem Compound Summary for CID 962, Water, 2023. URL `https://pubchem.ncbi.nlm.nih.gov/compound/Water`.

[60] National Center for Biotechnology Information. PubChem Compound Summary for CID 13387, 1-Methyl-2-pyrrolidinone, 2023. URL `https://pubchem.ncbi.nlm.nih.gov/compound/1-Methyl-2-pyrrolidinone`.

[61] National Center for Biotechnology Information. PubChem Compound Summary for CID 31275, Dioxane, 2023. URL `https://pubchem.ncbi.nlm.nih.gov/compound/Dioxane`.

[62] Kang Xu. Nonaqueous liquid electrolytes for lithium-based rechargeable batteries. *Chemical Reviews*, 104(10):4303–4417, 10 2004. ISSN 00092665. doi: 10.1021/cr030203g.

[63] Matthew Li, Chunsheng Wang, Zhongwei Chen, Kang Xu, and Jun Lu. New Concepts in Electrolytes. *Chemical Reviews*, 120(14):6783–6819, 7 2020. ISSN 15206890. doi: 10.1021/acs.chemrev.9b00531.

[64] Rosamar a Fong, Ulrich Yon Sacken, and J R Dahn. Studies of Lithium Intercalation into Carbons Using Nonaqueous Electrochemical Cells. *The Electrochemical Society*, 137(7): 2009–2013, 7 1990.

[65] S Tobishima, M Arakawa, T Hirai, and J Yamaki. Ethylene Carbonate-based Electrolytes for Rechargeable Lithium Batteries. *Journal of Power Sources*, 26:449–454, 1989.

[66] J M Tarascon and D Guyomard. New electrolyte compositions stable over the 0 to 5 V voltage range and compatible with the Lil +xMn204/carbon Li-ion cells. *Solid State Ionics*, 69:293–305, 1994.

[67] M Schmidt, U Heider, A Kuehner, R Oesten, M Jungnitz, N Ignat'ev, and P Sartori. Lithium fluoroalkylphosphates: a new class of conducting salts for electrolytes for high energy lithium-ion batteries. *Journal of Power Sources*, 97-98:557–560, 2000.

[68] Grant West. Modern ceramic engineering: properties, processing and use in design: David W. Richerson Marcel Dekker, Inc., USA, 1992 ISBN 0-8427-8634-3, xv + 872 pp, 1994.

[69] Johannes Landesfeind, Johannes Hattendorff, Andreas Ehrl, Wolfgang A. Wall, and Hubert A. Gasteiger. Tortuosity Determination of Battery Electrodes and Separators by

Impedance Spectroscopy. *Journal of The Electrochemical Society*, 163(7):A1373–A1387, 2016. ISSN 0013-4651. doi: 10.1149/2.1141607jes.

[70] BioLogic. Protocols for studying intercalation electrodes materials : Part I: Galvanostatic cycling with potential limitation (GCPL), 2005. URL `www.biologic.net`.

[71] Gamry Instruments. Basics of Electrochemical Impedance Spectroscopy. Technical report, Gamry Instruments, 2010.

[72] Scribner Associates. ZView ® 4.0 Operating Manual Impedance / Gain-Phase Graphing & Analysis Software. Technical report. URL `www.scribner.com`.

[73] Jarle Hjelen. *Scanning elektron-mikroskopi*. SINTEF, Trondheim, 1989. URL `https://urn.nb.no/URN:NBN:no-nb_digibok_2013070305116`.

[74] Yao Nan. Introduction to the focused ion beam system. In *Focused Ion Beam Systems: Basics and Applications*, volume 9780521831994, pages 1–30. Cambridge University Press, 1 2007. ISBN 9780511600302. doi: 10.1017/CBO9780511600302.002.

[75] Emily Moore. *Fourier Transform Infrared Spectroscopy (FTIR) : Methods, Analysis, and Research Insights*. Chemical Engineering Methods and Technology. Nova Science Publishers, Inc, Hauppauge, New York, 2016. ISBN 9781536103830. URL `https://search.ebscohost.com/login.aspx?direct=true&db=nlebk&AN=1419216&site=ehost-live&scope=site`.

[76] Brian C Smith. *Fundamentals of Fourier transform infrared spectroscopy*. CRC Press, Boca Raton, Fla, 2nd ed. edition, 2011. ISBN 9781420069297.

[77] Judith Mihály, Silvana Sterkel, Hugo M Ortner, László Kocsis, László Hajba, Éva Furdyga, and János Mink. FTIR and FT-Raman Spectroscopic Study on Polymer Based High Pressure Digestion Vessels. *CROATICA CHEMICA ACTA*, 79(3):497–501, 2006.

[78] Nick Daems, Sam Milis, Rhea Verbeke, Anthony Szymczyk, Paolo Pescarmona, and Ivo Vankelecom. High-performance membranes with full pH-stability. *RSC Advances*, 8: 8813–8827, 2 2018. doi: 10.1039/C7RA13663C.

[79] Somayeh Mohamadi. Preparation and Characterization of PVDF/PMMA/Graphene Polymer Blend Nanocomposites by Using ATR-FTIR Technique. In *Infrared Spectroscopy - Materials Science, Engineering and Technology*. InTech, 4 2012. doi: 10.5772/36497.

[80] Yakimchuk Evgenyi, Vladimir Volodin, and Irina Antonova. New graphene derivative with N-methylpirrolidone: suspension, structural, optical and electrical properties. *Physical Chemistry Chemical Physics*, 21, 5 2019. doi: 10.1039/C9CP01612K.

[81] M. Bini, D. Capsoni, S. Ferrari, E. Quartarone, and P. Mustarelli. Rechargeable lithium batteries: Key scientific and technological challenges. In *Rechargeable Lithium Batteries: From Fundamentals to Applications*, pages 1–17. Elsevier Inc., 4 2015. ISBN 9781782420989. doi: 10.1016/B978-1-78242-090-3.00001-8.

[82] Michaela Memm, Alice Hoffmann, and Margret Wohlfahrt-Mehrens. Water-based LiNi1/3Mn1/3Co1/3O2-cathodes with good electrochemical performance by use of additives. *Electrochimica Acta*, 260:664–673, 1 2018. ISSN 00134686. doi: 10.1016/j.electacta.2017.12.014.

A Constants and Variables

Table A.1: Constants and variables used in the calculations

Symbol	Description	Unit	Value
$A_{electrode}$	Area of electrode	cm^2	2.01
$C_{electrode}$	Theoretical capacity for an electrode	mAh	-
$C_{theoretical}$	Theoretical specific capacity for a given material	mAh g^{-1}	-
C_{AM}	Concentration of active material	wt%	-
$C_{PVDFsol}$	Concentration of PVDF dissolved in NMP	wt%	-
d_{Al}	Thickness of the Al-foil current collector	mm	-
d_{cast}	Thickness cast on current collector	mm	-
$d_{electrode}$	Thickness of entire electrode	mm	-
m_{AM}	Mass of active material	g	-
m_{Al}	Mass of current collector	g	-
$m_{electrode}$	Mass of electrode and current collector	g	-
m_{NMP}	Mass of NMP	g	-
m_{PVDF}	Mass of PVDF binder	g	-
$m_{PVDFsol}$	Mass of 5% PVDF in NMP solution	g	-
m_{tot}	Total mass of electrode components	g	-
m_{tot}	Total mass of electrode components	g	-
$wt_c\%$	Weight percentage of component c	%	-
wt_{CB} %	Weight percentage of carbon black	%	-
$wt_{NMC}\%$	Weight percentage of NMC	%	-
$wt_{PVDF}\%$	Weight percentage of PVDF	%	-
TD_c	True density of component c	g cm^{-2}	-
TD_{CB}	True density of Carbon Black	g cm^{-2}	2.1
TD_{NMC}	True density of NMC	g cm^{-2}	2.63
TD_{PVDF}	True density of PVDF	g cm^{-2}	1.78
σ	conductivity	mS/m	-
τ	Tortosity		

B Calculations used in experimental procedure

Binder solution

The PVDF solution was made by mixing PVDF powder and N-methyl-2-pyrrolidine (NMP). Batches of ca. 10 g solutions were made with a target concentration of 5 wt%. The amount of NMP needed was calculated after weight out the PVDF powder to reach a 5% solution. The amount of each component needed is given by Equations B.1-B.2

$$m_{PVDF} = 10g \cdot 0.05 = 0.5g \tag{B.1}$$

$$m_{NMP} = m_{PVDF} \cdot 19 = 9.5g \tag{B.2}$$

The actual amount of each component and the resulting concentration for each batch is given in Table B.1.

Table B.1: Actual amounts of each component used in the PVDF solution and the resulting concentration of each batch.

Batch	mass PVDF [g]	mass NMP [g]	Concentration [%]
1	0.5273	10.0471	4.99
2	0.5014	10.0094	05.01

Slurry mixture

The slurry mixture used was aimed to be a 90:5:5 ratio of NMC:CB:PVDF. Batches were made with 2g of NMC and the amount needed for the other components was calculated from the amount of NMC. Equations B.3-B.5 gives the aimed amount of each component for the slurry mixture.

$$m_{tot} = \frac{m_{NMC}}{90\%} = \frac{2.0000g}{90\%} = 2.2222g \tag{B.3}$$

$$m_{CB} = m_{tot} \cdot 5\% = 2.2222g \cdot 5\% = 0.1111g \tag{B.4}$$

$$m_{PVDF} = m_{tot} \cdot 5\% = 2.2222g \cdot 5\% = 0.1111g \tag{B.5}$$

The PVDF was dissolved prior to use as a 5 wt% solution of PVDF in NMP. This was taken into account and Equation B.5 was expanded into Equation B.6

$$m_{PVDFsol} = \frac{m_{PVDF}}{C_{PVDFsol}} = \frac{0.1111g}{5wt\%} = 2.2222g \tag{B.6}$$

Table B.2 gives the actual amounts used compared to the calculated amounts needed to create the slurry mixture used in the electrode construction.

Table B.2: Calculated and actual amount of each component in each batch of the slurry mixture, with deviations from the calculated amount.

Component	Batch	calculated amount [g]	actual amount [g]	% deviation from calculated
Batch 1				
NMC	1	2.0000 g	2.0025	0.0013
Carbon Black	1	0.1111	0.1111	0.0000
PVDF:NMP (5%)	1	0.1109	0.1109	0.0000
PVDF	1	2.2180	2.2180	0.0000
Batch 2				
NMC	2	2.0000	2.0011	0.0005
Carbon Black	2	0.1111	0.1112	0.0009
PVDF:NMP (5%)	2	0.1113	0.1114	0.0009
PVDF	2	2.2260	2.2340	0.0035

Loading and C-rates

The loading of an electrode is the amount of active material per area, given by Equation B.7

$$\text{Loading}[\frac{\text{mg}}{\text{cm}^2}] = \frac{m_{AM}}{A_{electrode}} \tag{B.7}$$

Where m_{AM} is the mass of active material and $A_{electrode}$ is the area of the electrode. The mass of active material can be found by Equation B.8

$$m_{AM} = (m_{electrode} - m_{Al}) \cdot \frac{C_{AM}\%}{100\%} = (m_{electrode} - m_{Al}) \cdot \frac{90\%}{100\%} \tag{B.8}$$

Here, $m_{electrode}$ is the mass of the electrode, m_{Al} is the mass of the Al-foil, and C_{AM} is the percentage of active material in the sample. The mass of the active material and theoretical specific capacity, $C_{theoretical}$ can also be used to calculate the theoretical C-rate for the electrode, $C_{electrode}$, as displayed in Equation B.9

$$C_{electrode} = m_{AM} \cdot C_{theoretical} \tag{B.9}$$

Porosity

The equation for calculating porosity given in Equation 2.6. Here the equation will be expanded and the geometrical density (GD) and theoretical density (TD) are defined.

As the thickness measured, d, includes the thickness of the Al-foil, d_{Al}, this has to be subtracted to find the electrode thickness $d_{electrode}$. The area of the electrode, $A_{electrode}$, is circular. The Equation for the GD is given in B.10

$$GD = (d_{electrode} - d_{Al}) \cdot A_{electrode} = d_{cast} \cdot \pi r^2 \tag{B.10}$$

The true density uses is the sum of the true density of each component in the slurry multiplied by the weight percentages of each component within the slurry, as seen in Equation B.11.

$$TD = \sum_{c=1}^{n} TD_c \cdot wt\%_c \tag{B.11}$$

For the slurry used in this project work, the true density is calculated by

$$TD = (TD_{NMC} \cdot wt\%_{NMC}) + (TD_{CB} \cdot wt\%_{CB}) + (TD_{PVDF} \cdot wt\%_{PVDF}) \tag{B.12}$$

Table B.3 gives the true density of each component used in the slurry mixture and the weight percentages of each component, and the calculated true density for each of the batches made.

Table B.3: True densities of the components used in the slurry mixture along with the true density of the electrodes from each of the batches made.

Component	True density [g cm^{-2}]
NMC	2.63
CB	2.1
PVDF	1.78
Batch 1	2.5611 ± 0.00002
Batch 2	2.5609 ± 0.00001

C Additional plots

Galvanostatic cycling

Potential curves for the remaining half-cells

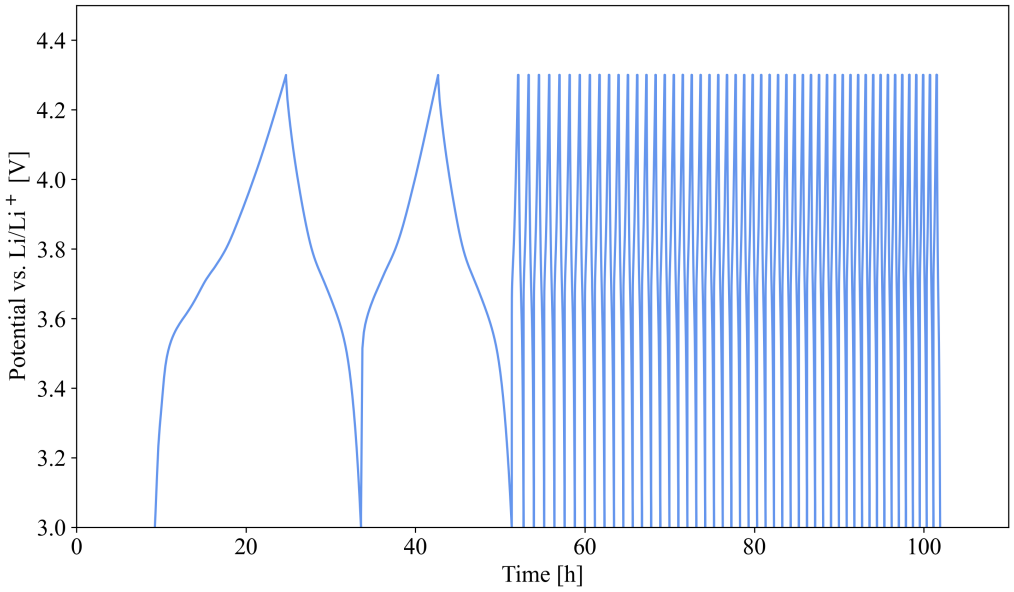

Figure C.1: Potential curve for one of the freeze-dried electrodes in a half cell cycled at a C-rate of 1C

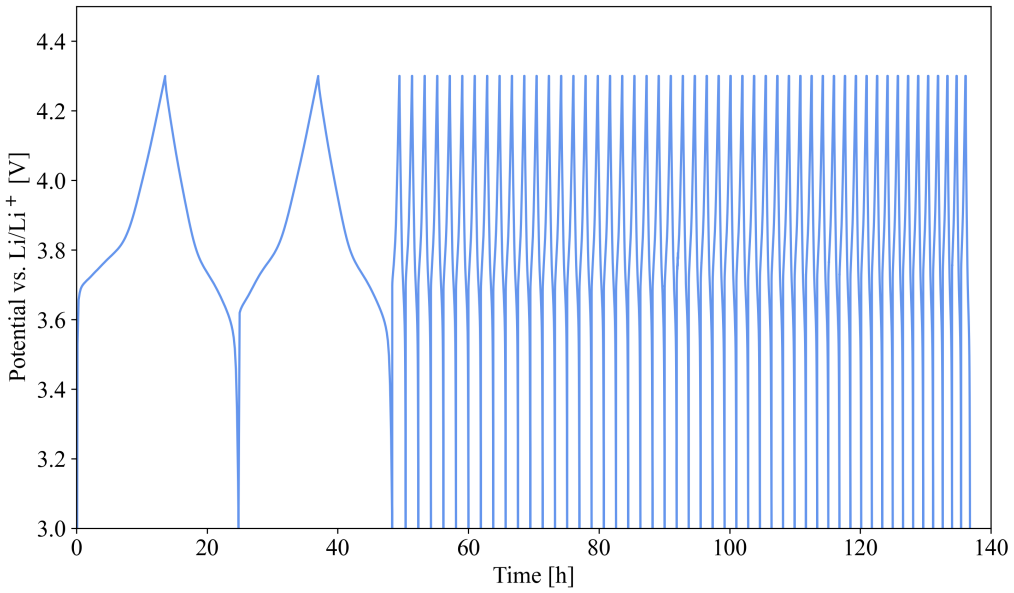

Figure C.2: Potential curve for one of the freeze-dried electrodes in a half cell cycled at a C-rate of 1C

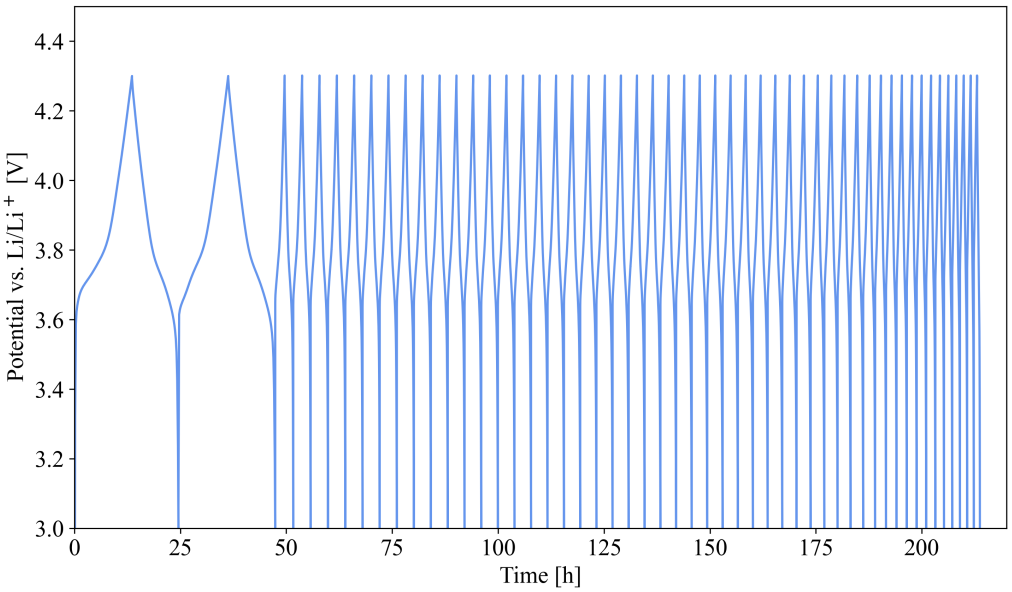

Figure C.3: Potential curve for one of the freeze-dried electrodes in a half cell cycled at a C-rate of C/2

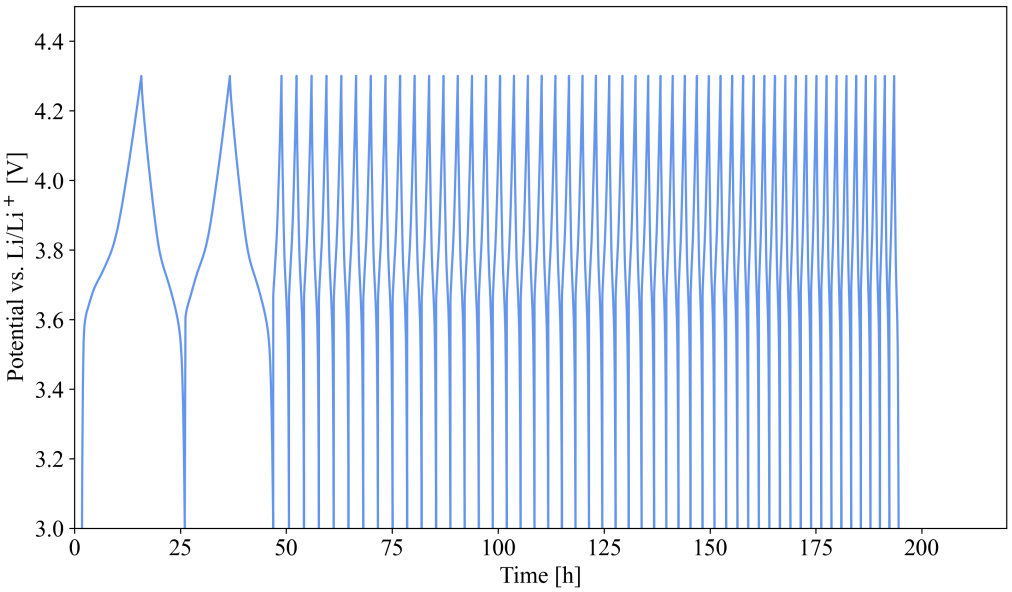

Figure C.4: Potential curve for one of the freeze-dried electrodes in a half cell cycled at a C-rate of C/2

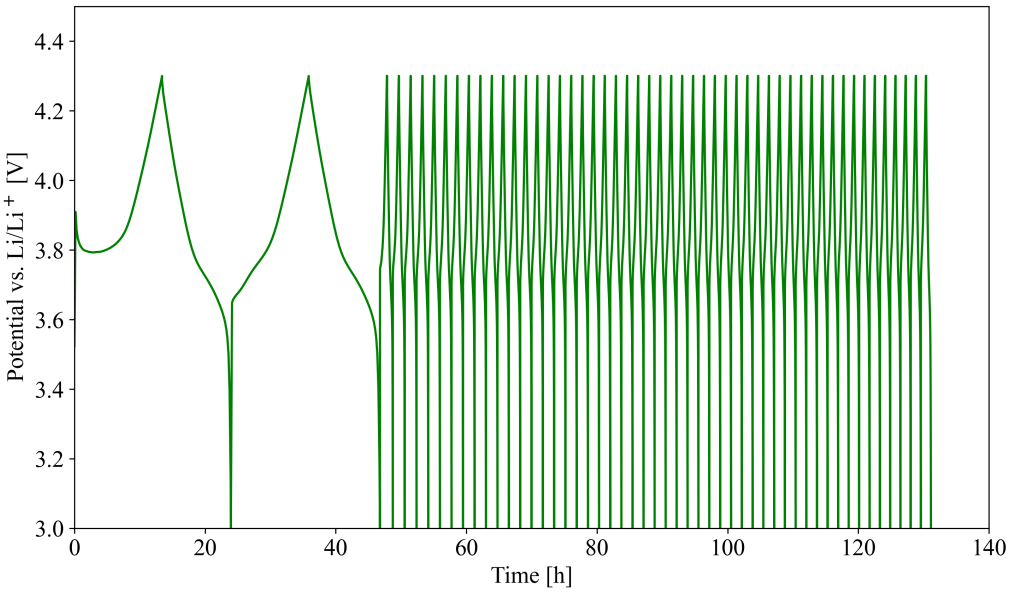

Figure C.5: Potential curve for one of the reference electrodes in a half cell cycled at a C-rate of 1C

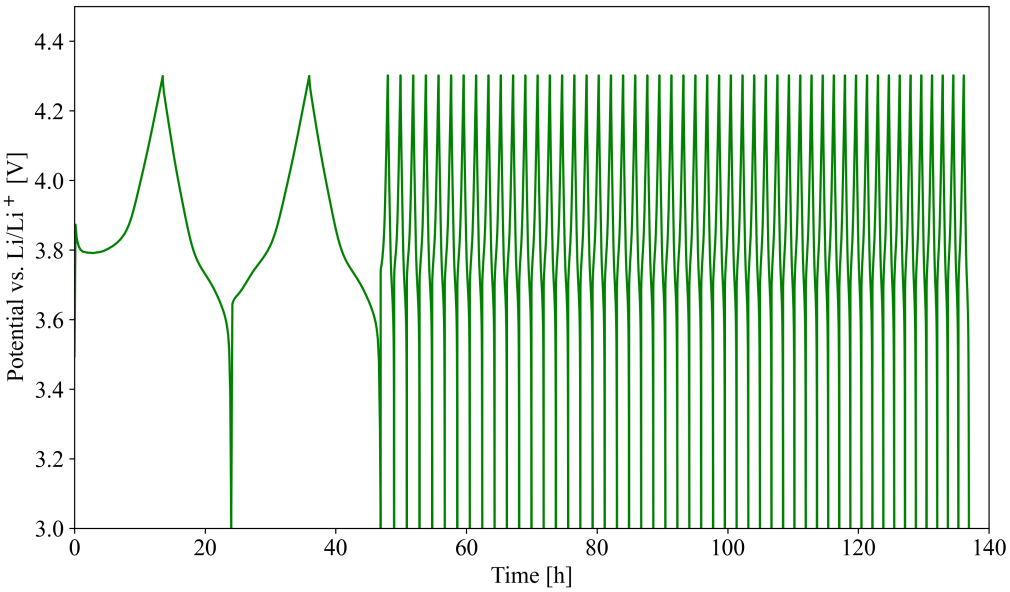

Figure C.6: Potential curve for one of the reference electrodes in a half cell cycled at a C-rate of 1C

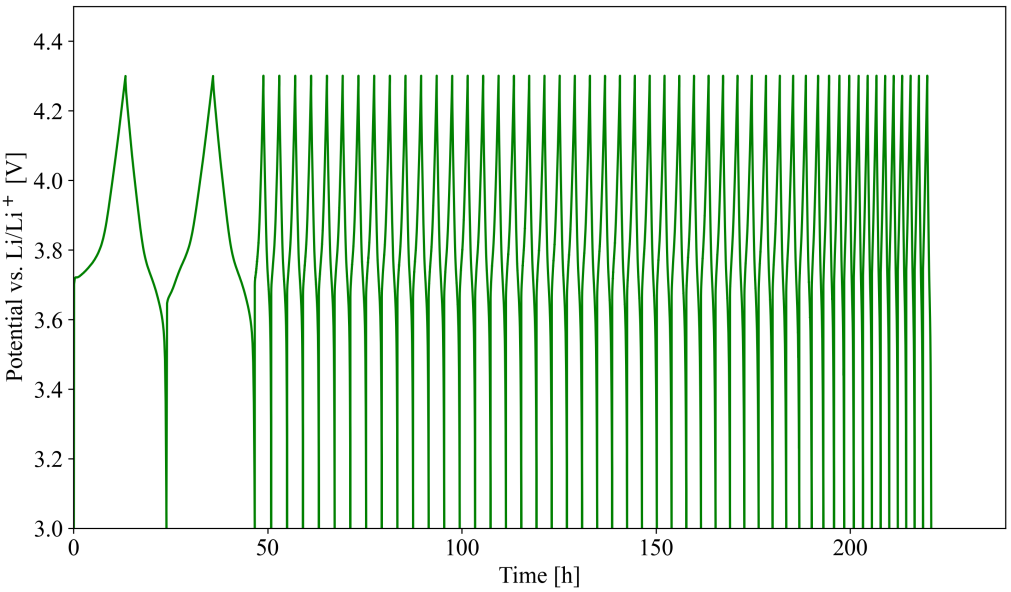

Figure C.7: Potential curve for one of the reference electrodes in a half cell cycled at a C-rate of C/2

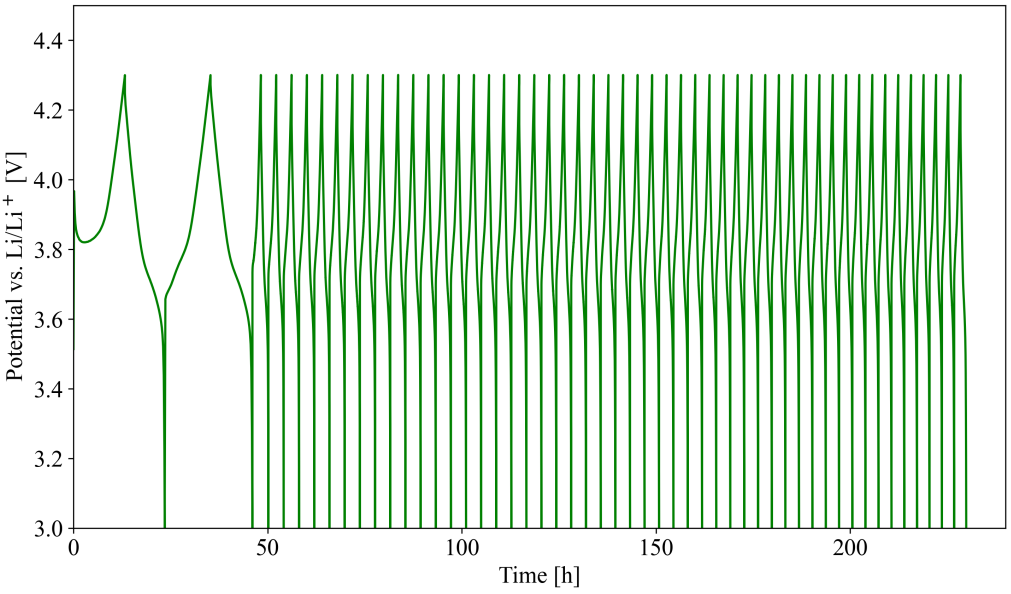

Figure C.8: Potential curve for one of the reference electrodes in a half cell cycled at a C-rate of C/2

Potential profiles for the remaining half-cells

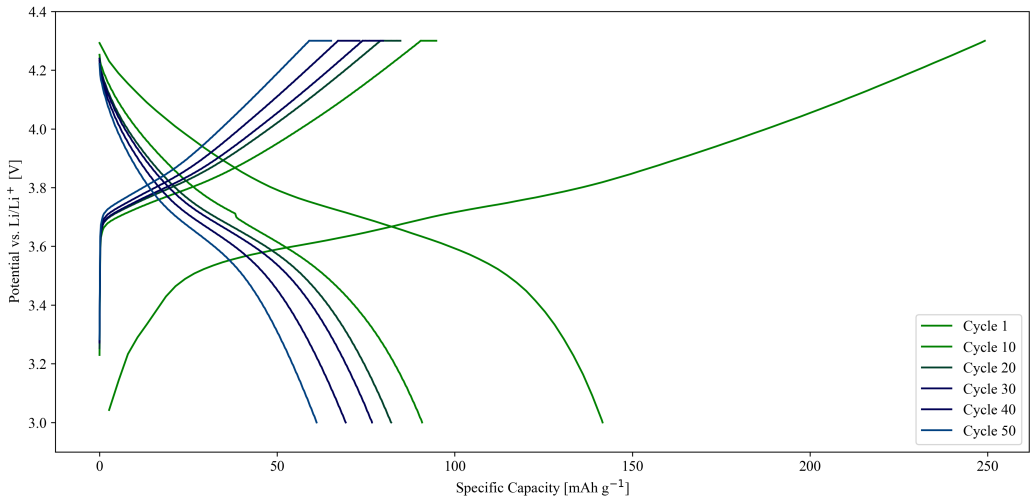

Figure C.9: Potential vs. capacity during cycle 1, 10, 20, 30, 40 and 50 for one of the freeze-dried electrodes in a half cell cycled at a C-rate of 1C

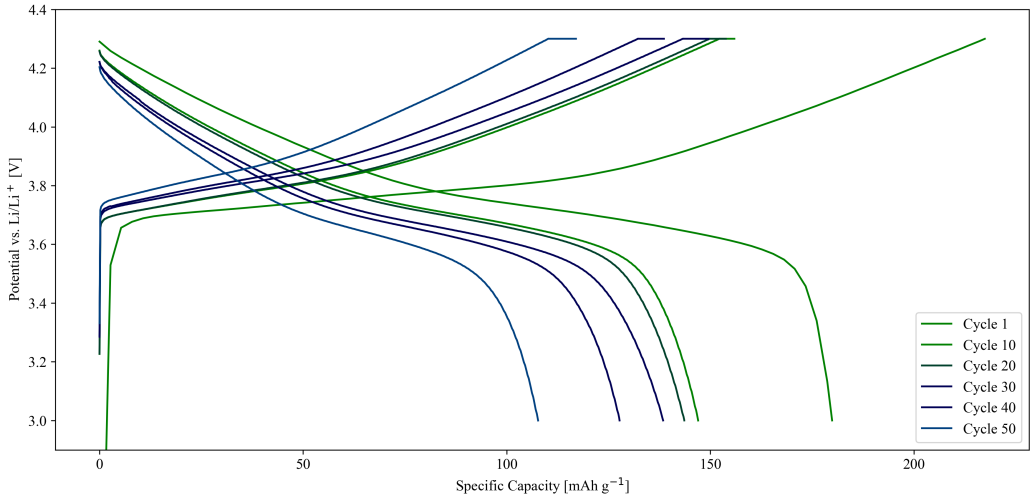

Figure C.10: Potential vs. capacity during cycle 1, 10, 20, 30, 40 and 50 for one of the freeze-dried electrodes in a half cell cycled at a C-rate of 1C

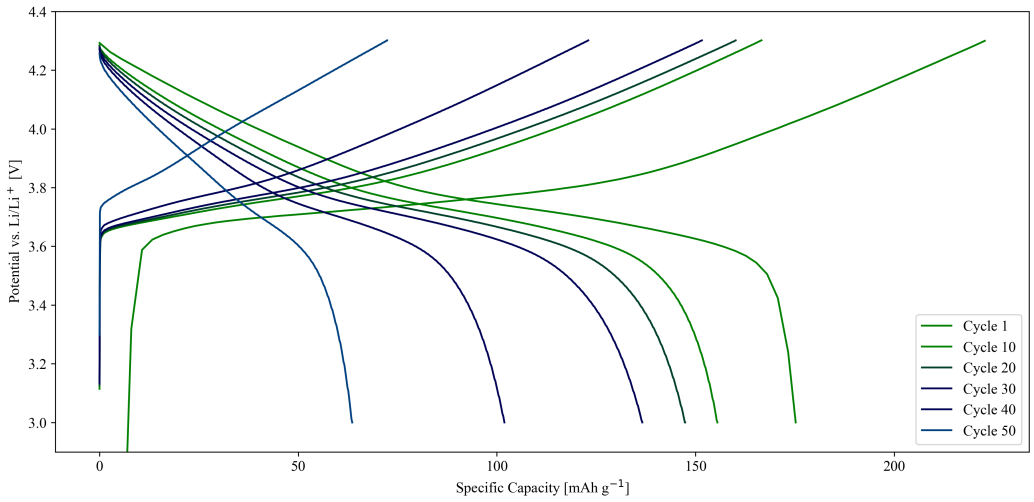

Figure C.11: Potential vs. capacity during cycle 1, 10, 20, 30, 40 and 50 for one of the freeze-dried electrodes in a half cell cycled at a C-rate of C/2

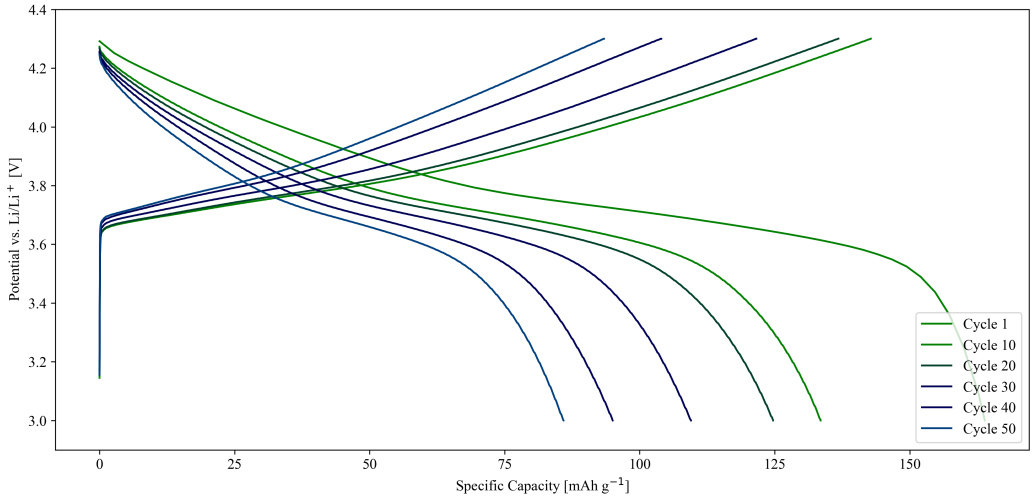

Figure C.12: Potential vs. capacity during cycle 1, 10, 20, 30, 40 and 50 for one of the freeze-dried electrodes in a half cell cycled at a C-rate of C/2

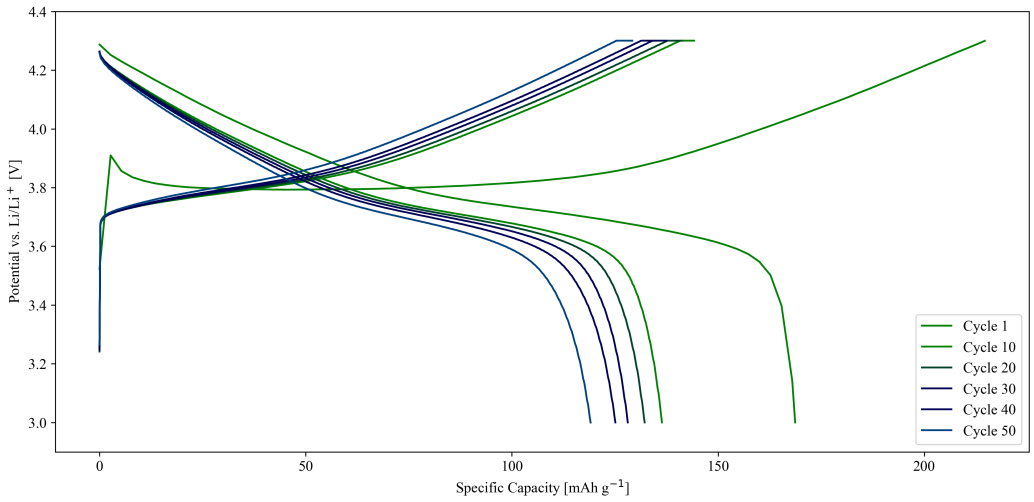

Figure C.13: Potential vs. capacity during cycle 1, 10, 20, 30, 40 and 50 for one of the reference electrodes in a half cell cycled at a C-rate of 1C

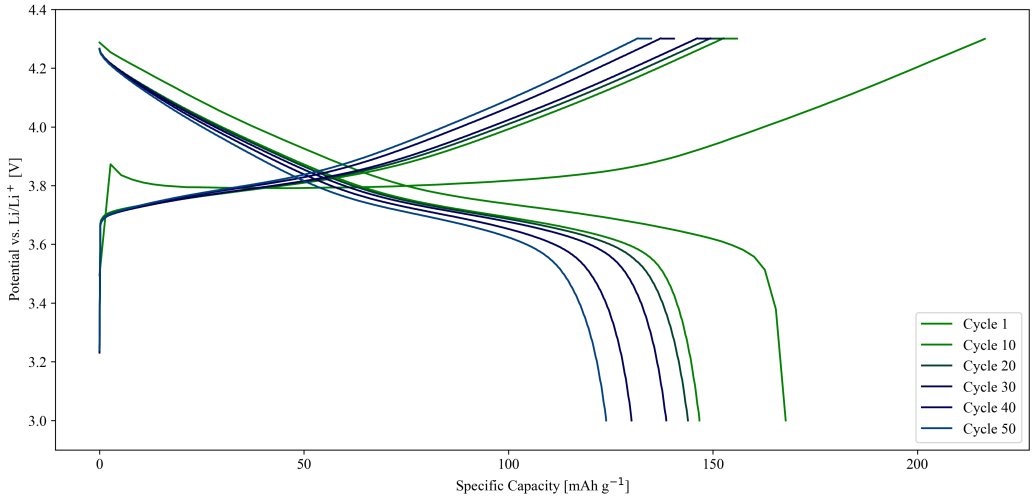

Figure C.14: Potential vs. capacity during cycle 1, 10, 20, 30, 40 and 50 for one of the reference electrodes in a half cell cycled at a C-rate of 1C

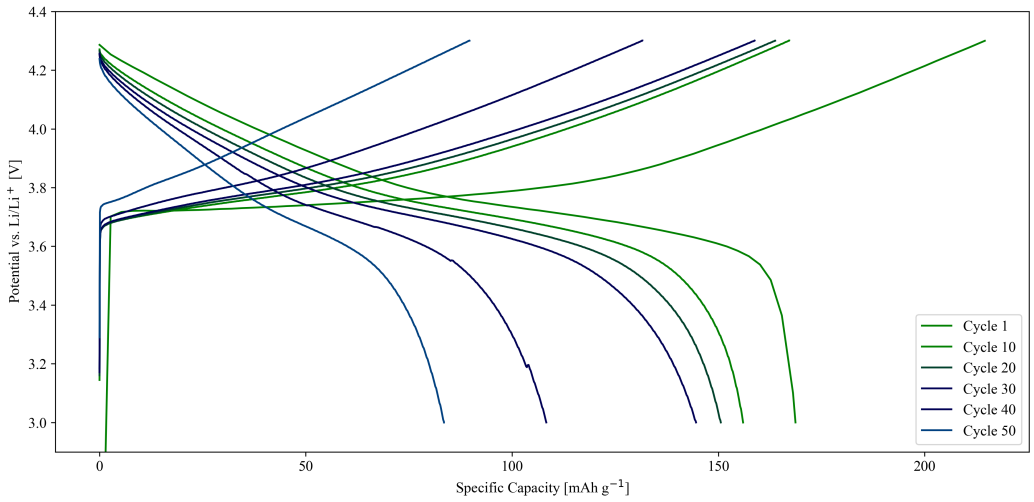

Figure C.15: Potential vs. capacity during cycle 1, 10, 20, 30, 40 and 50 for one of the reference electrodes in a half cell cycled at a C-rate of C/2

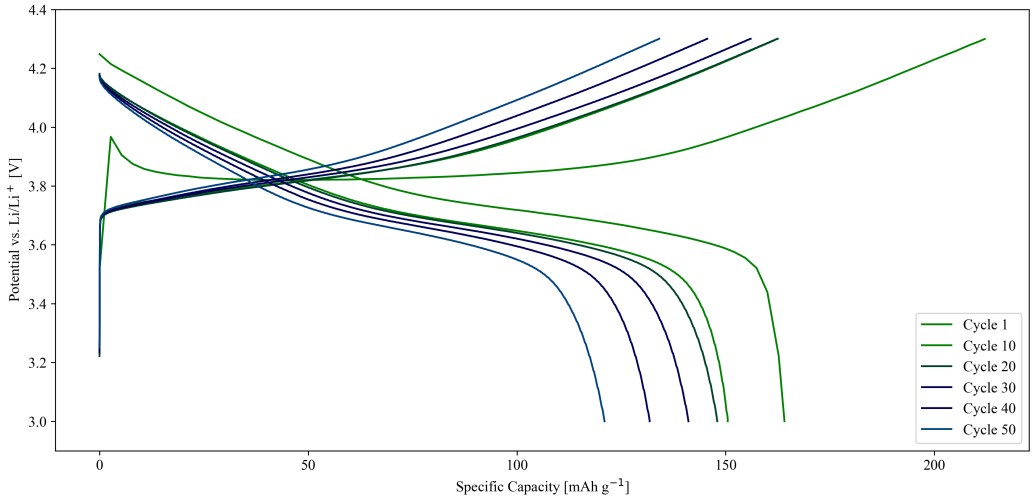

Figure C.16: Potential vs. capacity during cycle 1, 10, 20, 30, 40 and 50 for one of the reference electrodes in a half cell cycled at a C-rate of C/2

Potentiostatic electrochemical impedance spectroscopy

The data from the EIS measurements of the symmetrical cells were fitted to the circuit shown in Figure 2.9 using ZView. The values obtained from the fitting corresponding to Figure 2.9 are presented in Table C.1.

Table C.1: Parameters for the circuit shown in Figure 2.9 with corresponding fitted data and error values. ZView was used to fit the experimental data for the symmetrical cells using freeze-dried and reference electrodes.

Electrode	Parameters	Impedance 0.01M	Impedance 0.005M
Freeze-dried	R1	30.60 ± 0.01	145.50 ± 0.33
	R2	32.07 ± 0.29	60.74 ± 0.99
	Q_0	0.000082 ± 0.000001	0.000103 ± 0.000001
	α_Q	0.631 ± 0.002	0.668 ± 0.002
	Z_W	18.75 ± 1.01	121.60 ± 3.25
	τ_W	0.0060 ± 0.0003	0.0312 ± 0.0009
	α_W	0.4864 ± 0.0006	0.4978 ± 0.0006
Reference	R1	39.17 ± 0.12	176.40 ± 0.62
	R2	52.24 ± 5.69	111.60 ± 1.80
	Q_0	0.000041 ± 0.000001	0.000055 ± 0.000001
	α_Q	0.662 ± 0.002	0.626 ± 0.002
	Z_W	0.759 ± 17.013	53.86 ± 6.09
	τ_W	0.0001 ± 0.0031	0.0109 ± 0.0013
	α_W	0.4658 ± 0.0004	0.4621 ± 0.0007

D Additional characteristic diagrams

Backgrounds of FITR spectra

Figures D.1 and D.2 display the background spectra which were subtracted from the samples analyzed by FTIR. Figure D.1 was subtracted from the PVDF powder, while Figure D.2 was subtracted from the vacuum-dried and freeze-dried sampled of the PVDF solution.

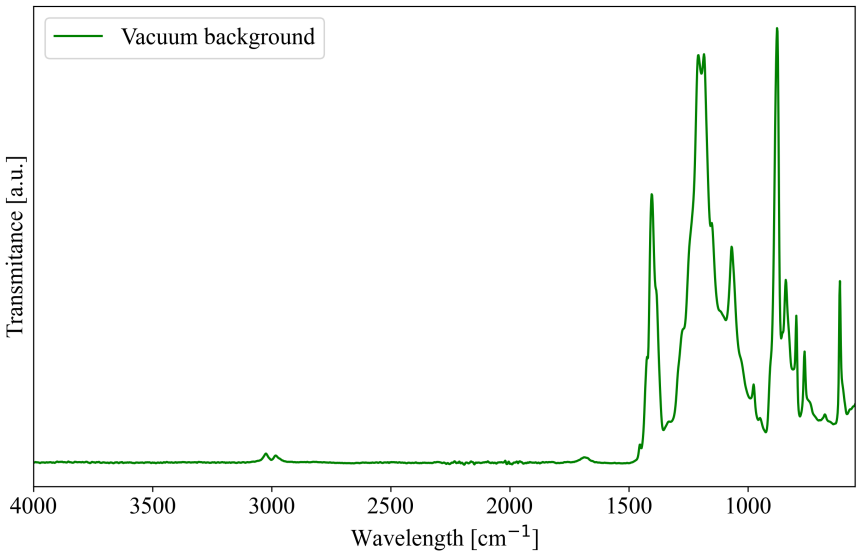

Figure D.1: The background spectrum of the plain Al-foil.

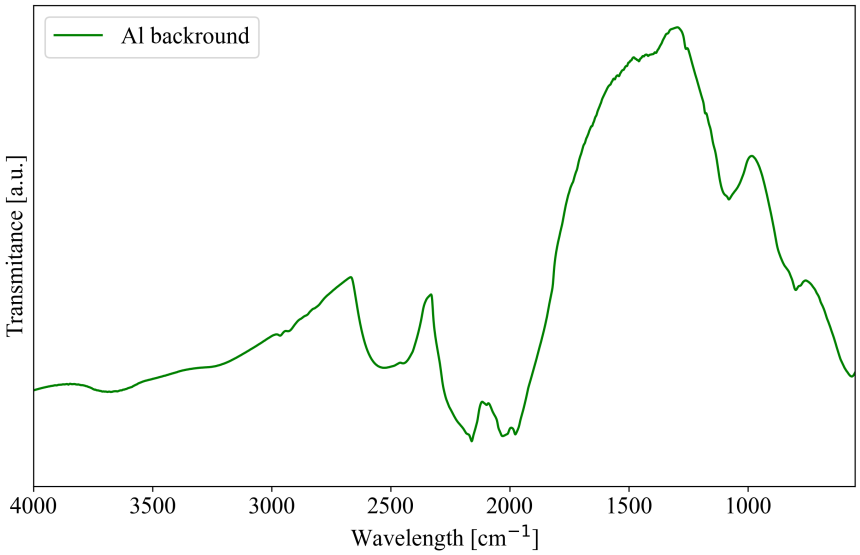

Figure D.2: The background spectrum of vacuum.

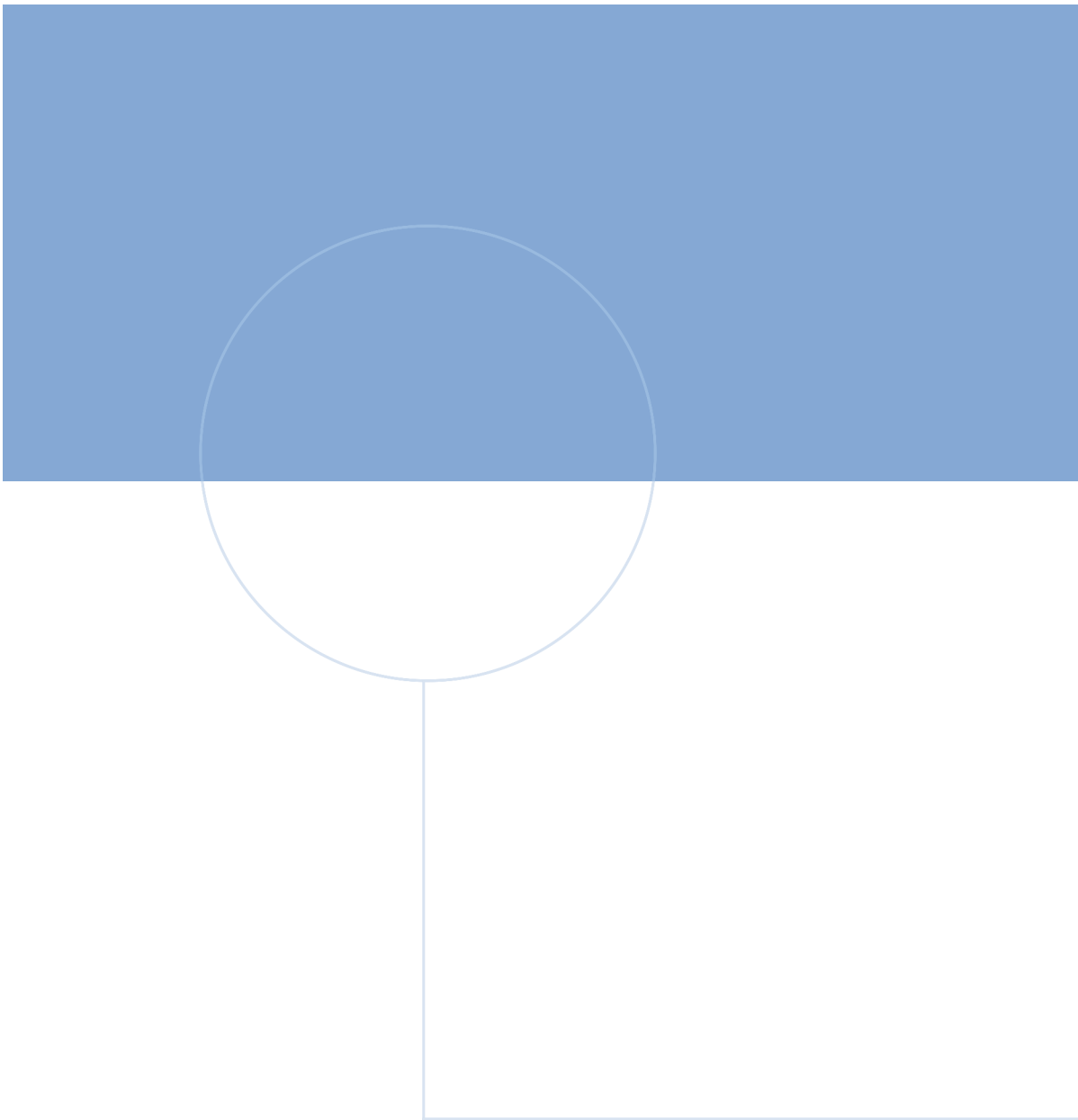

NTNU

Norwegian University of
Science and Technology